

DISSERTATION

NETWORKED RADAR SYSTEMS: WAVEFORMS, SIGNAL PROCESSING  
AND RETRIEVALS FOR VOLUME TARGETS

Submitted by

Nitin Bharadwaj

Department of Electrical and Computer Engineering

In partial fulfillment of the requirements

for the Degree of Doctor of Philosophy

Colorado State University

Fort Collins, Colorado

Fall, 2009

UMI Number: 3401022

All rights reserved

**INFORMATION TO ALL USERS**

The quality of this reproduction is dependent upon the quality of the copy submitted.

In the unlikely event that the author did not send a complete manuscript and there are missing pages, these will be noted. Also, if material had to be removed, a note will indicate the deletion.



UMI 3401022

Copyright 2010 by ProQuest LLC.

All rights reserved. This edition of the work is protected against unauthorized copying under Title 17, United States Code.



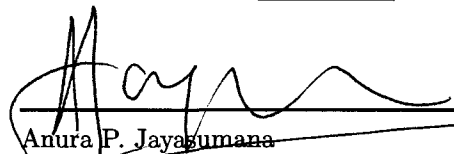
ProQuest LLC  
789 East Eisenhower Parkway  
P.O. Box 1346  
Ann Arbor, MI 48106-1346

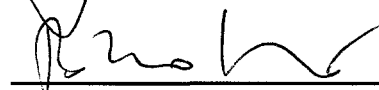
COLORADO STATE UNIVERSITY

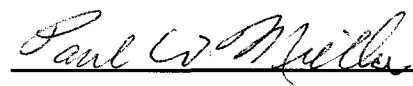
October 30, 2009

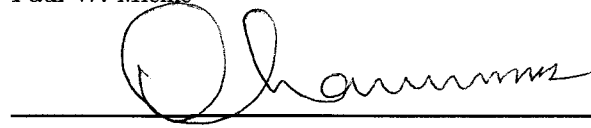
WE HEREBY RECOMMEND THAT THE DISSERTATION PREPARED UNDER OUR SUPERVISION BY NITIN BHARADWAJ ENTITLED NETWORKED RADAR SYSTEMS: WAVEFORMS, SIGNAL PROCESSING AND RETRIEVALS FOR VOLUME TARGETS BE ACCEPTED AS FULFILLING IN PART REQUIREMENTS FOR THE DEGREE OF DOCTOR OF PHILOSOPHY.

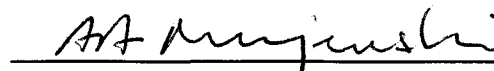
Committee

  
Anura P. Jayagumana

  
Branislav M. Notaros

  
Paul W. Mielke

  
Advisor: Chandrasekar Venkatachalam

  
Department Head: Anthony A. Maciejewski

## ABSTRACT OF DISSERTATION

### NETWORKED RADAR SYSTEMS: WAVEFORMS, SIGNAL PROCESSING AND RETRIEVALS FOR VOLUME TARGETS

Networked radar systems consisting of a dense set of agile short-range high frequency radars operating as Distributed Collaborative Adaptive System (DCAS) is an emerging innovative concept for atmospheric remote sensing that offer great potential to address several challenging problems in atmospheric remote sensing. This research addresses some of the unique challenges that must be overcome to successfully deploy a networked radar system. This research also provides a novel waveform and methodology for a networked radar environment and wideband waveforms for next generation precipitation radars.

The waveform design for a low-cost magnetron based dual polarization weather radar operating at X-band is presented. The waveform aims to concurrently address range-velocity ambiguity, ground clutter, hardware and operational requirements. Adaptive spectral processing of dual-polarization weather radar signals is presented for ground clutter suppression and range velocity ambiguity mitigation along with an evaluation of the spectral methodology based on simulations as well as data. The waveform and adaptive spectral processing is fully operational in the Integrated Project-1 (IP1) X-band radar network deployed by the Engineering Research Center (ERC) for Collaborative Adaptive Sensing of the Atmosphere (CASA). The IP1 radar network provides real-time data to the various end-users.

A transition from traditional high powered transmitters to solid-state transmitter is essential to realize a dense network of low cost electronically steered radars. However, solid-state radars have low peak powers and this necessitates the use of pulse compression waveforms. In this research a novel frequency diversity wideband waveform is proposed to mitigate low sensitivity of solid-state radars. In addition, the waveform mitigates the range eclipsing problem associated with long pulse compression waveforms. An analysis of the performance of this novel waveform is presented for volume targets.

In this research, two novel techniques using the concept of different look angles, inherent in a networked radar environment, is presented. The first technique is a networked waveform system where the range-velocity ambiguity problem is formulated for a networked radar environment by using the principle that the underlying intrinsic properties of the medium such as reflectivity and velocity must remain self consistent. A distributed waveform is designed to resolve the ambiguities of observations within the coverage region of the networked radar system. The second technique is a methodology for the enhancement of spatial resolution of reflectivity resulting from volume targets such as precipitation. The enhancement in resolution is obtained by jointly processing observations from the individual radar nodes. The resolution enhancement system (RES) uses the inherent nature of networked radar systems of observing a precipitation event with different look angles. Results and analysis for the networked radar algorithms are presented from simulations as well as data collected by the IP1 radar network.

Nitin Bharadwaj  
Department of Electrical and Computer Engineering  
Colorado State University  
Fort Collins, Colorado 80523  
Fall, 2009

## ACKNOWLEDGEMENTS

My experience at Colorado State University during my graduate study has been very rich, extremely valuable, and rewarding. I am especially thankful and indebted to my advisor Dr. Chandrasekar V. Chandra for his support, guidance, encouragement, and opportunities he provided during my graduate study. I would like to also express my gratitude to Dr. Anura Jayasumana, Dr. Branislav Notaros and Dr. Paul Mielke for serving as my committee members.

I also wish to thank Francesc Junyent for his help in implementing the real-time software and collecting valuable data from CASA's IP1 radar network. I appreciate and thank all the members of the Radar and Communication Group, Dmitri Moisseev, Yanting Wang, Sanghun Lim, Cuong Nguyen and Jim George for all the discussions and your help during my graduate study.

Also, I am deeply grateful to my mother, Vimala Bharadwaj and my brother, Naveen Bharadwaj for their love, support and encouragement while I was far away from home.

This work was supported by the National Science Foundation (NSF) Engineering Research Center (ERC) program (0313747), NSF Colorado State University CHILL program, and National Aeronautics and Space Administration (NASA) Precipitation Measurement Mission (PMM).

## TABLE OF CONTENTS

<b>Abstract of Dissertation</b>	<b>ii</b>
<b>Acknowledgements</b>	<b>iv</b>
<b>Table of Contents</b>	<b>v</b>
<b>List of Figures</b>	<b>ix</b>
<b>List of Tables</b>	<b>xix</b>
<b>1 Introduction</b>	<b>1</b>
1.1 Introduction . . . . .	1
1.2 Problem statement . . . . .	4
1.3 Research question . . . . .	4
1.4 Focus of dissertation . . . . .	4
1.5 Overview of dissertation . . . . .	6
<b>2 Background</b>	<b>8</b>
2.1 Doppler weathers radars . . . . .	8
2.2 Precipitation covariance matrix and radar observables . . . . .	10
2.2.1 Doppler spectral moments . . . . .	11
2.2.2 Polarimetric variables . . . . .	13
2.3 Single versus distributed radar environments . . . . .	14
2.4 CASA first generation DCAS system . . . . .	17

<b>3</b>	<b>Spectral Processing for Dual Polarization Weather Radars</b>	<b>21</b>
3.1	Introduction . . . . .	21
3.2	Effect of window function . . . . .	22
3.3	Spectral clutter filtering . . . . .	26
3.4	Retrieval of polarimetric variables . . . . .	31
3.5	Results . . . . .	32
3.6	Summary . . . . .	34
<b>4</b>	<b>Waveform Design and Processing for the CASA X-band Radar Systems</b>	<b>37</b>
4.1	Introduction . . . . .	37
4.2	Waveform design perspective . . . . .	39
4.2.1	Range-velocity ambiguity . . . . .	39
4.2.2	Ground Clutter . . . . .	41
4.3	Design Considerations . . . . .	41
4.3.1	Operation Requirements . . . . .	42
4.3.2	Hardware requirements . . . . .	43
4.4	Ground clutter filtering . . . . .	43
4.5	Dual-PRF waveform . . . . .	50
4.6	Waveform for first generation CASA radars . . . . .	59
4.6.1	Real-time environment and data . . . . .	60
4.6.2	Clutter suppression in IP1 . . . . .	61
4.6.3	Overlay echo suppression in IP1 . . . . .	66
4.6.4	Velocity dealiasing in IP1 . . . . .	70
4.7	Summary . . . . .	74
<b>5</b>	<b>Wideband Waveforms for Polarimetric Radars with Solid-state Transmitters</b>	<b>78</b>
5.1	Introduction . . . . .	78

5.2	Sensitivity Mapped Generalized Waveforms . . . . .	80
5.3	Pulse compression waveforms . . . . .	83
5.3.1	Nonlinear frequency modulation (NLFM) . . . . .	84
5.3.2	Compression filters . . . . .	85
5.4	Side lobe characterization for NLFM pulse compression . . . . .	87
5.4.1	Doppler tolerance . . . . .	88
5.4.2	Phase noise tolerance . . . . .	89
5.5	Pulse compression for volume targets . . . . .	91
5.5.1	Range resolution . . . . .	91
5.5.2	Receiver bandwidth . . . . .	92
5.5.3	Impact on Doppler spectral moments . . . . .	93
5.5.4	Impact on polarimetric variables . . . . .	98
5.6	Frequency diversity waveform . . . . .	104
5.7	Summary . . . . .	109
<b>6</b>	<b>Networked Waveform System for Weather Radar Network</b>	<b>115</b>
6.1	Introduction . . . . .	115
6.2	Multiple Doppler observations . . . . .	118
6.3	Networked Waveform System . . . . .	119
6.3.1	Formulation and solution . . . . .	119
6.3.2	Analysis . . . . .	121
6.4	Simulation Study . . . . .	124
6.5	Results . . . . .	127
6.6	Summary . . . . .	132
<b>7</b>	<b>Resolution Enhancement System For Networked Radar Systems</b>	<b>134</b>
7.1	Introduction . . . . .	134
7.2	Received signal from volume targets . . . . .	136
7.3	Resolution of measured reflectivity . . . . .	137

7.4	The CASA example . . . . .	140
7.4.1	Multiscale analysis . . . . .	142
7.4.2	Simulations : Multiscale analysis . . . . .	144
7.5	Implementation with CASA radar network data . . . . .	151
7.5.1	Case I: Small precipitation cell . . . . .	151
7.5.2	Case II: Thunder storm cell . . . . .	153
7.5.3	Case III: Hook echo . . . . .	156
7.5.4	Results: multiscale analysis . . . . .	159
7.6	Summary . . . . .	162
<b>8</b>	<b>Summary and Conclusions</b>	<b>164</b>
8.1	Summary and Conclusions . . . . .	164
8.2	Future Work . . . . .	169
	<b>Bibliography</b>	<b>170</b>

## LIST OF FIGURES

2.1	Illustrating the (continuous) range-time axis ( $\tau$ ) and the (discrete) sample-time axis ( $t_s$ ). The pulse-repetition time (PRT) is $T_s$ (Bringi and Chandrasekar, 2001). . . . .	9
2.2	Illustration of the earth's curvature problem encountered in radar operations (NRC, 1995). . . . .	16
2.3	The four polarimetric radars forming the IP1 radar network. . . . .	18
2.4	Map showing the location of each radar node in the IP1 radar network.	19
3.1	Comparison of standard deviation of spectral moments and polarimetric variables as a function of number of samples. (a). Reflectivity (b) Mean Doppler velocity (c). Differential reflectivity and (d). Differential propagation phase shift. . . . .	23
3.2	Comparison of standard deviation of spectral moments and polarimetric variables as a function of Doppler spectral width. (a). Reflectivity (b) Mean Doppler velocity (c). Differential reflectivity and (d). Differential propagation phase shift. . . . .	24
3.3	Illustration of spectral clutter filtering using a Gaussian model. . . . .	29
3.4	Error in the estimated spectral moments (a) Reflectivity (b) Mean Doppler velocity (c) Spectral width. The signal has been simulated for $N = 64$ samples at $\lambda = 11$ cm with $T_s = 1$ ms and $CSR = 40$ dB. . .	30

3.5	Error in the estimated polarimetric variables (a) Differential reflectivity(ZDR) (b) Differential propagation phase $\phi_{dp}$ (c) Lag 0 co-polar correlation coefficient ( $\rho_{hv}$ ). The signal has been simulated for $N = 64$ samples at $\lambda = 11\text{ cm}$ with $T_s = 1\text{ ms}$ and $CSR = 40\text{ dB}$ . . . . .	33
3.6	Comparison of estimated spectral moments with pulse-pair and spectral processing (a) Reflectivity from pulse-pair (b) Reflectivity from spectral processing (c) Doppler velocity from pulse-pair(d) Doppler velocity from spectral processing (e) Spectral width from pulse-pair and (f) Spectral width from spectral processing.The data obtained is from a snow storm with blizzard conditions on Dec 20, 2006 at 23:58:19 UTC.	35
3.7	Comparison of of estimated polarimetric variables with pulse-pair and spectral processing (a) Differential reflectivity from pulse-pair (b) Differential reflectivity from spectral processing (c) Differential phase from pulse-pair(d) Differential phase from spectral processing (e) Co-polar correlation coefficient from pulse-pair and (f) Co-polar correlation coefficient from spectral processing.The data obtained is from a snow storm with blizzard conditions on Dec 20, 2006 at 23:58:19 UTC. . .	36
4.1	Comparisons of range-velocity limitations for S-band and X-band radars	40
4.2	Clutter filtering with Gaussian spectral density fits . . . . .	47
4.3	Standard deviation of power and mean Doppler velocity as a function of clutter-to-signal ratio for a weather signal with $N = 64$ samples, $\sigma_v = 2\text{ m/s}$ , and $SNR = 10 - 20\text{ dB}$ . The weather echo is located at half the Nyquist velocity at PRF=2 kHz. . . . .	48
4.4	Standard deviation of $Z_{dr}$ and $\phi_{dp}$ as a function of clutter-to-signal ratio for a weather signal with $N = 64$ samples, $\sigma_v = 2\text{ m/s}$ , and $SNR = 10 - 20\text{ dB}$ . The weather echo is located at half the Nyquist velocity at PRF=2 kHz. . . . .	50

4.5	Standard deviation of reflectivity and mean Doppler velocity after ground clutter filtering as a function of number of pulses for $\sigma_v = 2$ m/s and $\sigma_v = 4$ m/s. The standard deviation is plotted for $PRF = 1.6$ kHz and $PRF = 2.4$ kHz for an $SNR = 10$ dB, $CSR = 25$ dB and $0.25^\circ$ phase noise. . . . .	51
4.6	Standard deviation of $Z_{dr}$ and $\phi_{dp}$ after ground clutter filtering as a function of number of pulses for $\sigma_v = 2$ m/s and $\sigma_v = 4$ m/s. The standard deviation is plotted for $PRF = 1.6$ kHz and $PRF = 2.4$ kHz for an $SNR = 10$ dB, $CSR = 25$ dB and $0.25^\circ$ phase noise. . . . .	52
4.7	Scatter plot of unfolded Doppler velocity versus the true Doppler velocity for $\sigma_v = 4$ m/s for two different dual-PRF waveform at X-band.	55
4.8	Unfolding error rate as a function of mean Doppler velocity for $CSR = 25$ dB and phase noise $\delta\theta = 0.25^\circ$ . Waveform-I: $PRF_1 = 2.4$ kHz, $N_1 = 54$ , $PRF_2 = 1.6$ kHz, $N_2 = 40$ and $v_a = 38.3$ m/s. Waveform-II= $PRF_1 = 3.0$ kHz, $N_1 = 64$ , $PRF_2 = 2.0$ kHz, $N_2 = 56$ and $v_a = 47.8$ m/s. . . . .	56
4.9	Unfolding error rate as a function of variance of mean Doppler velocity for raw unfolded velocity, phasor median filter, and median filter data. Waveform-I: $PRF_1 = 2.4$ kHz, $N_1 = 54$ , $PRF_2 = 1.6$ kHz, $N_2 = 40$ and $v_a = 38.3$ m/s. Waveform-II= $PRF_1 = 3.0$ kHz, $N_1 = 64$ , $PRF_2 = 2.0$ kHz, $N_2 = 56$ and $v_a = 47.8$ m/s. . . . .	58
4.10	Illustration of dual-PRF waveform implemented in CASA IP1 radars.	59
4.11	RHI plots of dual-PRF data collected with Chickasha radar on May 04, 2009 at 19:34:18 UTC:(a) The unfiltered and filtered reflectivity;(b) The unfiltered and filtered mean Doppler velocity. . . . .	62
4.12	RHI plots of dual-PRF data collected with Chickasha radar on May 04, 2009 at 19:34:18 UTC:(a) The unfiltered and filtered $Z_{dr}$ ;(b) The unfiltered and filtered $ \rho_{hv}(0) $ . . . . .	63

4.13	Scatter plot of $Z_h$ versus $Z_{dr}$ from RHI data collected with KSAO radar at different azimuths during a wide spread showers on May 04, 2009 from 19:24 to 19:34 UTC. The scatter plot is done for data with unfiltered and filtered data. . . . .	64
4.14	PPI plots of dual-PRF data collected with Cyril radar on May 09, 2007 at 00:37:42 UTC:(a) The unfiltered and filtered reflectivity;(b) The unfiltered and filtered velocity. . . . .	65
4.15	Cumulative distribution function of clutter suppressed (a) with weather signal (b) without weather echo. The cumulative distribution functions plotted is for ten data sets collected with the IP1 radar network. . . .	67
4.16	Reflectivity of a precipitation cell contaminated with ground clutter and overlaid echoes. (a) Unfiltered reflectivity (b) Filtered reflectivity. Data collected from Cyril on Feb 10, 2009 at 21:15:08 UTC with a dual-PRF waveform. . . . .	70
4.17	Cumulative distribution function of overlaid echo suppressed. The cumulative distribution functions plotted is for ten data sets collected with the IP1 radar network. . . . .	71
4.18	Reflectivity of a precipitation cell forming a hook echo. Data collected from Cyril on Feb 10, 2009 at 21:15:39 UTC with a dual-PRF waveform. . . . .	72
4.19	Doppler velocity of a precipitation cell forming a hook echo (a) Folded velocity (b) Unfolded velocity. Data collected from Cyril on Feb 10, 2009 at 21:15:39 UTC with a dual-PRF waveform. . . . .	73
4.20	PPI plots of dual-PRF data collected with Cyril radar on Mar 24, 2009 at 00:50:15 UTC:(a) The filtered reflectivity;(b) Raw unfolded velocity and (c) PMF filtered velocity. . . . .	75
5.1	Minimum detectable reflectivity of a sensitivity mapped frequency diversity waveform with three components. The peak transmit power $P_t = 100 W$ operating at X-band. . . . .	83

5.2	Nonlinear FM characteristics . . . . .	85
5.3	Nonlinear FM Pulse compression waveform (a) FM characteristics (b) Amplitude of transmit pulse. The Pulse compression waveform has a nonlinear chirp of $B = 3.6 MHz$ , $T = 40 \mu s$ pulse length, and base-band sampling frequency $f_s = 5 MHz$ . . . . .	88
5.4	Side lobe level as a function of Doppler velocity (a) Peak size-lobe level(b) Integrated side-lobe level. The Pulse compression waveform has a nonlinear chirp of $B = 3.6 MHz$ , $T = 40 \mu s$ pulse length, and base-band sampling frequency $f_s = 5 MHz$ . . . . .	89
5.5	Peak side-lobe level as a function of Doppler velocity and system phase noise. The Pulse compression waveform has a nonlinear chirp of $B = 3.6 MHz$ , $T = 40 \mu s$ pulse length, and base-band sampling frequency $f_s = 5 MHz$ . . . . .	90
5.6	Integrated side-lobe level as a function of Doppler velocity and system phase noise. The Pulse compression waveform has a nonlinear chirp of $B = 3.6 MHz$ , $T = 40 \mu s$ pulse length, and base-band sampling frequency $f_s = 5 MHz$ . . . . .	90
5.7	Comparison of range resolution using Chebyshev-80 dB mismatch filter and minimum ISL filter for Pulse compression waveform using $B = 3.6 MHz$ , $T = 40 \mu s$ and $T = 20 \mu s$ pulse length, and base-band sampling frequency $f_s = 5 MHz$ . . . . .	92
5.8	(a) Spectrum of transmit pulse and compression filter characteristics (b) Comparison of ambiguity function with 80 dB Chebyshev window filter and minimum ISL filter. The Pulse compression waveform has a nonlinear chirp of $B = 3.6 MHz$ , $T = 40 \mu s$ pulse length, and base-band sampling frequency $f_s = 5 MHz$ . . . . .	94

5.9	Observation of a trapezoidal reflectivity profile with $20\text{db}/\text{km}$ gradient. (a) Observed mean reflectivity (b) Bias in measured reflectivity (c) Standard deviation of reflectivity. The Pulse compression waveform has a nonlinear chirp of $B = 3.6\text{ MHz}$ , $T = 40\ \mu\text{s}$ pulse length, and base-band sampling frequency $f_s = 5\text{ MHz}$ . The phase noise of the system is 0 degrees . . . . .	95
5.10	Observation of a trapezoidal reflectivity profile with $20\text{db}/\text{km}$ gradient. (a) Observed mean reflectivity (b) Bias in measured reflectivity (c) Standard deviation of reflectivity. The Pulse compression waveform has a nonlinear chirp of $B = 3.6\text{ MHz}$ , $T = 40\ \mu\text{s}$ pulse length, and base-band sampling frequency $f_s = 5\text{ MHz}$ . The phase noise of the system is 0.5 degrees . . . . .	96
5.11	Observation of a trapezoidal reflectivity profile with $20\text{db}/\text{km}$ gradient. (a) Observed mean reflectivity (b) Bias in measured reflectivity (c) Standard deviation of reflectivity. The Pulse compression waveform has a nonlinear chirp of $B = 3.6\text{ MHz}$ , $T = 40\ \mu\text{s}$ pulse length, and base-band sampling frequency $f_s = 5\text{ MHz}$ . The phase noise of the system is 0.5 degrees . . . . .	97
5.12	The impact of side lobe level on $Z_h$ using a step function profile with varying step sizes of reflectivity with phase noise $\delta\theta = 0.25^\circ$ . . . . .	99
5.13	The impact of side lobe level on $v$ using a step function profile with varying step sizes of reflectivity with phase noise $\delta\theta = 0.25^\circ$ . . . . .	100
5.14	The impact of side lobe level on $Z_{dr}$ using a step function profile with varying step sizes of reflectivity with phase noise $\delta\theta = 0.25^\circ$ . . . . .	101
5.15	The impact of side lobe level on $\phi_{dp}$ using a step function profile with varying step sizes of reflectivity with phase noise $\delta\theta = 0.25^\circ$ . . . . .	102
5.16	The impact of side lobe level on $\rho_{hv}$ using a step function profile with varying step sizes of reflectivity with phase noise $\delta\theta = 0.25^\circ$ . . . . .	103

5.17	The standard deviation of $Z_{dr}$ and $\phi_{dp}$ with the reflectivity step size as a parameters (a) for a waveform with $T = 40\mu s$ and (b) for a waveform with $T = 20\mu s$ . . . . .	105
5.18	Time-frequency plot of the frequency diversity pulse compression waveform (a) Transmit pulse envelope (b) Time frequency plot. . . . .	106
5.19	Simulation of frequency diversity pulse compression waveform for an X-band radar. (a) Observed reflectivity field from CSU-CHILL radar on Jun 07, 2003 at 02:15:01 UTC (b) The retrieved reflectivity from a frequency diversity pulse compression waveform. . . . .	107
5.20	PPI plots of frequency diversity pulse compression waveform compared with the input data. The simulation is based on observation made with CASA IP1 radar at Chickasha on Mar 10, 2009 at 01:14:19 UTC. (a) Reflectivity (b) $Z_{dr}$ . . . . .	110
5.21	PPI plots of frequency diversity pulse compression waveform compared with the input data. The simulation is based on observation made with CASA IP1 radar at Chickasha on Mar 10, 2009 at 01:14:19 UTC. (a) $\phi_{dp}$ (b) $\rho_{hv}$ . . . . .	111
5.22	Scatter plot of reflectivity from frequency diversity pulse compression versus the input reflectivity. The data used for simulations were collected by Chickasha radar on Mar 10, 2009 at 01:14:19 UTC and Cyril radar on Apr 16, 2009 at 23:14:17 UTC. . . . .	112
6.1	Illustration of a networked radar concept (NETRAD). . . . .	116
6.2	Geometry of IP1 radar network. The four radar nodes are located at Cyril(KCYR), Chickasha(KSAO), Rush Springs(KRSP) and Lawton(KLWE). . . . .	117
6.3	Velocity unfolding error plotted as a function of standard deviation in velocity: (a) For N=3 radars;(b) For N=4 radars . . . . .	123

6.4	Velocity unfolding error as a function of wind speed and wind direction for the resolution volume located 20 km from Cyril radar at an azimuth of 60 deg. . . . .	125
6.5	Velocity unfolding error within the IP1 coverage area. (a) Mean unfolding error with a networked waveform using three radar nodes. (b) Mean unfolding error with networked waveform using four radar nodes.	126
6.6	Networked waveform simulation with the IP1 radar network at 1 degree elevation angle. (a) True and mean Doppler velocity with networked retrieval (b) Standard deviation of NETRAD velocity at Cyril (c) Unfolding error in NETRAD velocity at Cyril. . . . .	128
6.7	Networked waveform simulation with the IP1 radar network at 1 degree elevation angle. (a) Measured velocity at Cyril at PRF=1.6 kHz (b) Measured velocity at Cyril at PRF=1.84 kHz (c) True Doppler velocity of the simulated circulation and (d) (b) Networked retrieval for Cyril.	129
6.8	Networked waveform the IP1 radar network at 1 degree elevation angle. (a) Doppler velocity with networked retrieval (b) Reflectivity. . . . .	130
6.9	Networked waveform data collected on Mar 31, 2008 at 17:50:32 UTC with the IP1 radar network at 1 degree elevation angle. (a) Measured velocity at Cyril at PRF=1.6 kHz (b) Measured velocity at Cyril at PRF=1.84 kHz (c) Measured reflectivity and (d) (b) Networked retrieval for Cyril. . . . .	131
7.1	Received voltage due to scattering from particles located within a shell extending from $(r, r + \Delta r)$ . . . . .	137
7.2	Illustration of resolution volume size as a function of pulse width, range and beam width. . . . .	138
7.3	Range-variant discrete Gaussian kernel . . . . .	139
7.4	A two dimensional flat topped reflectivity distribution with 25 dB/km gradient. . . . .	141

7.5	Resolution enhancement system applied to simulated data for a three radar node case. Observed reflectivity from (a) KCYR (b) KSAO (c) KRSP. (d) True reflectivity distribution (e) Range weighted mosaic (f) Resolution enhancement system. . . . .	143
7.6	Case I : Observation of simulated data for a networked radar system :(a) KCYR (b) KSAO (c) KRSP, and (d) KLWE. . . . .	146
7.7	Case I : Simulated data for a networked radar system :(a) Location of the storm within the IP1 radar network (b) True reflectivity distribution (c) Reflectivity mosaic, and (d) RES retrieval. . . . .	147
7.8	Case II : Observation of simulated data for a networked radar system :(a) KCYR (b) KSAO (c) KRSP, and (d) KLWE. . . . .	148
7.9	Case II : Simulated data for a networked radar system :(a) Location of the storm within the IP1 radar network (b) True reflectivity distribution (c) Reflectivity mosaic, and (d) RES retrieval. . . . .	149
7.10	Isotropic power spectrum of reflectivity distribution: (a) Case I; (b) Case II. . . . .	150
7.11	Composite networked resolution for CASA's IP1 radar network. . . . .	152
7.12	Location of the precipitation event in the radar network for data collected with IP1 radar network on Jun 06, 2008 at 20:36:08 UTC. . . . .	153
7.13	Data collected with IP1 radar network on Jun 06, 2008 at 20:36:08 UTC: (a) KCYR (b) KSAO (c) KRSP, and (d) KLWE. . . . .	154
7.14	Reflectivity retrieval from the IP1 radar network with data collected on 2008-Jun-06 at 20:36:08 UTC (a) Range weighted reflectivity mosaic and (b) RES reflectivity retrieval. . . . .	155
7.15	Location of the precipitation event in the radar network for data collected with IP1 radar network on Jun 16, 2008 at 11:30:30 UTC. . . . .	156
7.16	Data collected with IP1 radar network on Jun 16, 2008 at 11:30:30 UTC: (a) KCYR (b) KSAO (c) KRSP, and (d) KLWE. . . . .	157

7.17	Reflectivity retrieval from the IP1 radar network with data collected on 2008-Jun-16 at 11:30:30 UTC (a) Range weighted reflectivity mosaic and (b) RES reflectivity retrieval. . . . .	158
7.18	Location of the precipitation event in the radar network for data collected with IP1 radar network on Feb 10, 2008 at 21:13:11 UTC. . . . .	159
7.19	Data collected with IP1 radar network on Feb 10, 2008 at 21:13:11 UTC: (a) KCYR (b) KSAO (c) KRSP, and (d) KLWE. . . . .	160
7.20	Reflectivity retrieval from the IP1 radar network with data collected on Feb 10, 2008 at 21:13:11 UTC (a) Range weighted reflectivity mosaic and (b) RES reflectivity retrieval. . . . .	161
7.21	Comparison of radially average power spectral density of the RES retrieved reflectivity and range weighted mosaic. . . . .	162

## LIST OF TABLES

2.1	IP1 network radar nodes location. . . . .	18
4.1	IP1 radar node design characteristics . . . . .	44
4.2	Dual-PRF unfolding for a stagger ratio of $2/3$ . . . . .	54
4.3	Ground clutter suppression . . . . .	66
4.4	Overlaid echo suppression . . . . .	71
5.1	Finite bandwidth filter loss for frequency diversity pulse compression waveform, $B = 3.6 MHz$ . . . . .	93
5.2	Frequency diversity pulse compression waveform . . . . .	104
5.3	Solid-state radar characteristics used in simulations . . . . .	108

# CHAPTER 1

## INTRODUCTION

---

### 1.1 Introduction

Weather radars have been operational and deployed around world for more than three decades. Doppler weather radars provide essential measurements of the atmosphere for meteorological, hydrological and climatological applications. Doppler radar observations have been of great value in detection and warning of hazards associated with severe storms like hail, high winds, flash floods and tornadoes. In addition, they have been a valuable tool in aviation safety. The deployment of weather surveillance radars world wide (WSR-88D in the US) and the airport Terminal Doppler Weather radars (TDWR) are considered as one of the major milestones in weather radar applications. Both WSR-88D and TDWR provide reflectivity and Doppler velocity which is obtained based on the amplitude and phase of the scattered electromagnetic wave from the precipitating phenomenon.

In the last three decades extensive research done with polarization diversity weather radars such as the Colorado State University CHILL (CSU-CHILL) radar has demonstrated that significant information about the micro-physics of precipitation is contained in the polarization state of the back-scattered wave. Dual polarization observations have significantly improved quantitative precipitation estimation (QPE) and hydrometeor classification. The dual polarization Doppler weather radars are considered an indispensable tool in the measurement and forecasting of atmospheric phenomena.

Although the existing long-range radars operating at S-band and C-band (longer wavelength radars) provide measurements of reflectivity and Doppler velocity observations for a very large area, these long range radars have limitations. First, the curvature of the Earth inhibits the observation of low-level atmospheric phenomenon closer to the surface of the Earth. For example, S-band radars with  $1^\circ$  beam width have a cross-range resolution of 1 km at 60 km. Second, the spatial resolution of long range radar is poor at farther ranges. Third, the long range radars have limited coverage in some regions due to terrain blockage. More recently, the emphasis on weather radars has been to move to attenuating frequencies such as X-band and K-band to enable more economical and distributed collaborative short-range radar systems, instead of stand alone long-range radar systems. The recent introduction of the Distributed Collaborative Adaptive System (DCAS) by the Center for Collaborative Adaptive Sensing of the Atmosphere (CASA) can be considered as a major step in weather radar applications in moving towards deployment of short-range radar networks.

The major emphasis on weather radars is the quantitative estimation of the precipitation content and three dimensional motion fields for both weather surveillance, forecasting and hydrological applications. There are several challenges that needs to be overcome in order to provide Doppler spectral moments and polarimetric variables suitable for the various quantitative applications such as QPE. The Doppler radar observables are estimated from the received signal back-scattered from precipitation particles and there are many factors that affect the received signal. Some of the main factors that affect the observations are waveform design (and signal processing algorithms), sensitivity of the radar system and electromagnetic wave attenuation due to propagation through precipitation. Some precipitation systems can cover several hundreds of km and the electromagnetic waves have to propagate through the targets to get to a target at a farther range. The impact of propagation effects on the radar

observables are more severe at higher frequencies such as X-band, Ku-band and Ka-band. This research focuses on aspects of waveform diversity and design for the next generation of dual-polarization Doppler weather radars.

Waveform diversity and design for weather radars present some interesting challenges that are similar to hard target radars in some aspects and very different in other aspects. Fundamentally, weather is a volume target, which is composed of large number of precipitation particles, each with its own velocity and scattering property. Hence the spectral property of the signal is a spectrum of finite width in the frequency domain. In addition, the polarization-dependent backscatter properties of the precipitation particles is different from that of ground clutter and hard targets such as airplanes and all of these can co-exist in the same observation volume. There are many challenges that must be considered for designing waveforms and processing algorithms to observe volume targets such as precipitation. First, an important aspect that brings unique challenges to weather radars is the demand for large dynamic range within short ranges (not just due to the range power dependence of the radar equation). This large dynamic range in received power is because weather targets can have light rain and drizzle existing within short distance of volumes with large hailstones that produce reflectivities that are different by as much as six to eight orders of magnitude. Second, unlike hard targets precipitation medium can be everywhere and extend over large areas. The very wide extent of precipitation can results in range-velocity ambiguity in pulse Doppler weather radar and pulsing schemes must take this into account. Third, the weather echoes can co-exist with very strong ground clutter echo which has to be suppressed before estimates of the radar observables are obtained. Each of the above aspects of the weather radar has driven specific aspects of the waveform design and they are the focus of this research, with special emphasis on the modern distributed collaborative adaptive systems of CASA operating at X-band.

## **1.2 Problem statement**

This research aims to address some of the unique and specific challenges that arise in designing, developing and deploying a short wavelength networked radar system. Specifically, the research concentrates on transmit waveforms, signal processing of the received signal and retrieval algorithms to provide radar observables from the networked radar system to the end-users. The objective of this research is to develop waveform system which will enable operation of the radar nodes within the radar network, be able to provide networked retrieval algorithms to enhance the radar observations and be able to provide both qualitative and quantitative conclusions about the waveforms and retrieval algorithms. This research is the first step towards developing, and to some extent realizing novel waveforms and retrieval methodologies for a modern networked radar system.

## **1.3 Research question**

The primary objective of the short wavelength networked radar system is to provide better spatial and temporal observations of meteorological phenomenon that occur in the troposphere. The question under consideration in this research is whether a network of radars observing a common precipitation event can mitigate ambiguities and provide higher resolution observations. Specifically, there are two primary questions being investigated. First, investigate whether a networked radar system can be used for designing waveforms to mitigate range-velocity ambiguity. Second, investigate the feasibility of improving spatial resolution of radar observations in a networked radar environment by using observations from a different view angle.

## **1.4 Focus of dissertation**

The main tasks of this research are grouped into two categories. The first category is individual radar node level waveforms and processing. The second category is

networked radar waveform and retrievals. The following items summarize the objects of the research in this dissertation.

***Waveforms and signal processing***

- i. Study the performance of spectral processing in estimating the Doppler spectral moments and polarimetric variables.
- ii. Evaluate spectral filtering methodology for polarimetric variables.
- iii. Characterize the statistical properties of ground clutter echo.
- iv. Design the waveform for a single node to minimize the impact of range-velocity ambiguity and ground clutter.
- v. Evaluate the performance of the waveform with the CASA's first generation radar network.
- vi. Design and evaluate wideband pulse compression waveform for meteorological radar.
- vii. Design and evaluate the performance of frequency diversity pulse compression waveform.

***Networked radar retrievals***

- i. Develop a networked waveform system to mitigate range-velocity ambiguity.
- ii. Evaluate and characterize the performance of the networked waveform.
- iii. Test and demonstrate the networked waveform with CASA's first generation radar network.
- iv. Develop a methodology to improve the resolution by using observations using different look angles.
- v. Test resolution enhancement system with simulation and data from CASA's first generation radar network.

## 1.5 Overview of dissertation

*Chapter 2* presents a short description about the nature of the received signal in a dual-polarization weather radar and the parameters estimated from the received signals. The summary of the meaning of the estimated parameters in characterizing the precipitation medium is also presented. The distinction between a monolithic and distributed radar is introduced. Finally the chapter ends with a very short description of the networked radar system deployed in Oklahoma.

*Chapter 3* presents the evaluation of spectral processing for dual-polarization weather radars. Also, spectral clutter filtering methodology is described for estimated spectral moments and polarimetric variables. The application of spectral processing to CSU-CHILL data is also presented in Chapter 3.

*Chapter 4* presents the challenges involved in the designing waveforms for weather radars. The performance of the waveforms for X-band radar is presented from simulated signals and statistics from operational radar network is reported.

*Chapter 5* describes the first steps needed for the transition from traditional high powered transmitters to solid-state transmitter that is essential to realize a network of low cost electronically steered radars. In this chapter frequency diversity wideband waveforms are proposed to mitigate low sensitivity of solid-state transmitters. In addition, the waveforms mitigate the range eclipsing problem associated with pulse compression. An analysis of the performance of pulse compression using mismatched compression filters is reported in this chapter.

*Chapter 6* presents a novel waveform that is designed for networked operations. A networked retrieval algorithm for the distributed waveform is presented in this chapter along with the error that result due to geometry and waveform parameters. This chapter ends with a preliminary implementation of the networked waveform in CASA's first generation IP1 radar network.

*Chapter 7* presents a networked resolution enhancement system that makes use of different viewing angles to improve the resolution of the reflectivity observations.

A framework to improve the resolution is developed in this chapter. The analysis presented in this chapter is based on simulations and data collected with CASA's first generation IP1 radar network.

*Chapter 8* summarizes the findings of this research and ends the chapter with some suggestions for future work.

## CHAPTER 2

### BACKGROUND

---

---

#### 2.1 Doppler weathers radars

Precipitation is composed of a large number of hydrometeors extending over a large range. The antenna beam is filled with scatterers that contribute to the return signal. A pulse Doppler radar transmits a pulse train with a pulse repetition time (PRT)  $T_s$  and pulse width  $T_0$ . The received voltage corresponds to the back scattered signal from particles within a volume determined by pulse width  $T_0$ , antenna beam widths  $\theta_B$  and  $\phi_B$ . The back scattered signals from all the particles within a single resolution volume sum to a resultant voltage sample at the receiver at  $t = \tau$  (or  $r$ ). The sampling of received signal due to a pulse train is divided into range-time and sample-time. The range-time diagram for a periodic pulse train, spaced  $T_s$  apart is illustrated in Fig. 2.1. For a single transmitted pulse the range-time is defined as  $\tau = 2r/c$ , and the received voltage  $V_r(t)$  at  $t = \tau$  is due to back scatter from particles located within a resolution volume at range-time  $\tau$ . For a periodic pulse train with  $N$  pulses, the received voltage at the same range-time ( $\tau$ ) is given as  $V_r(t = \tau), V_r(t = \tau + T_s), \dots, V_r(t = \tau + (N - 1)T_s)$  which form a sequence of temporal samples from the same resolution volume (Fig.2.1). Each observation of the received signal is one realization of the underlying complex stochastic process. The fluctuations of the received voltage in sample-time is determined by the time-varying properties of the particles located in the resolution volume.

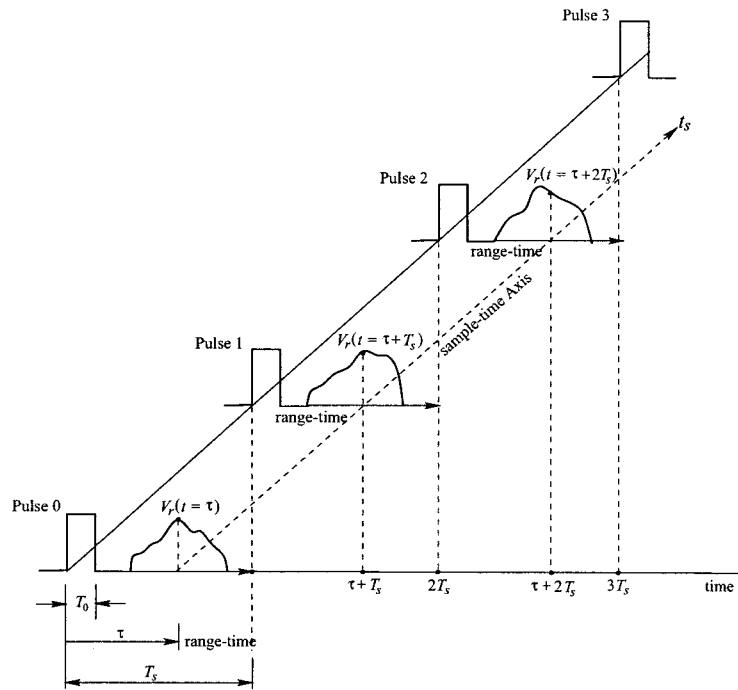


Figure 2.1: Illustrating the (continuous) range-time axis ( $\tau$ ) and the (discrete) sample-time axis ( $t_s$ ). The pulse-repetition time (PRT) is  $T_s$  (Bringi and Chandrasekar, 2001).

## 2.2 Precipitation covariance matrix and radar observables

The weather radar equation at single polarization is expressed as a well known scalar equation whereas the corresponding equation for dual polarization radar becomes a matrix equation expressed as (Bringi and Chandrasekar, 2001)

$$\begin{bmatrix} v_h \\ v_v \end{bmatrix} = \frac{\lambda\sqrt{P_t}G_0}{4\pi r^2} [\mathbf{T}][\mathbf{S}_{BSA}][\mathbf{T}] \begin{bmatrix} M_h \\ M_v \end{bmatrix} \text{ with } \mathbf{S} = \begin{bmatrix} S_{hh} & S_{hv} \\ S_{vh} & S_{vv} \end{bmatrix} \quad (2.1)$$

where  $\mathbf{T}$  is the transmission matrix of the uniform precipitation medium and is included for completeness to account for the propagation of electromagnetic waves through precipitation medium but it does not affect waveform coding.  $\mathbf{S}$  is the  $2 \times 2$  back-scattering matrix.  $M_h$  and  $M_v$  are the transmitter excitation states in horizontal and vertical ports of a dual-polarized antenna with an antenna gain  $G_0$ , transmit power  $P_t$  and operating at a wavelength  $\lambda$ . Thus it can be seen that the received signal ( $v_h$  and  $v_v$ ) is a vector depending on the transmit polarization state. In a switched or alternate polarization mode the transmit states are vectors

$$\begin{bmatrix} M_h \\ M_v \end{bmatrix} = \begin{bmatrix} 1 \\ 0 \end{bmatrix} \text{ and } \begin{bmatrix} M_h \\ M_v \end{bmatrix} = \begin{bmatrix} 0 \\ 1 \end{bmatrix} \quad (2.2)$$

resulting in a sequence of length four vector

$$\mathbf{z} = [v_{hh} \ v_{hv} \ v_{vh} \ v_{vv}]^T \quad (2.3)$$

corresponding to the two orthogonal transmit states. The subscripts vh (hv) refers to transmit horizontal(vertical) polarization and receive vertical(horizontal) polarization. The properties of this signal vector  $\mathbf{z}$  can be described in terms of the covariance matrix  $\mathbf{C}$

$$E\mathbf{z}\mathbf{z}^H = \mathbf{C} = E \begin{bmatrix} |v_{hh}|^2 & v_{hh}v_{vh}^* & v_{hh}v_{hv}^* & v_{hh}v_{vv}^* \\ v_{vh}v_{hh}^* & |v_{vh}|^2 & v_{hh}v_{hv}^* & v_{vh}v_{vv}^* \\ v_{hv}v_{hh}^* & v_{hv}v_{vh}^* & |v_{hv}|^2 & v_{hv}v_{vv}^* \\ v_{vv}v_{hh}^* & v_{vv}v_{vh}^* & v_{vv}v_{hv}^* & |v_{vv}|^2 \end{bmatrix} \quad (2.4)$$

where  $H$  is the Hermitian operator and  $*$  indicates complex conjugate. This  $4 \times 4$  matrix can be reduced to  $3 \times 3$  invoking reciprocity. This covariance matrix measurement corresponds to the covariance matrix of the scatterers in the precipitation

medium defined by (Bringi and Chandrasekar, 2001)

$$\boldsymbol{\Sigma} = \left\langle \left[ \begin{array}{ccc} |S_{hh}|^2 & \sqrt{2}S_{hh}S_{hv}^* & S_{hh}S_{vv}^* \\ \sqrt{2}S_{hv}S_{hh}^* & 2|S_{hv}|^2 & \sqrt{2}S_{hv}S_{vv}^* \\ S_{vv}S_{hh}^* & \sqrt{2}S_{vv}S_{hv}^* & |S_{vv}|^2 \end{array} \right] \right\rangle \quad (2.5)$$

where  $S_{hh}$ ,  $S_{hv}$ ,  $S_{vh}$  and  $S_{vv}$  are the elements of the scattering matrix,  $n$  is the number of particles per unit volume and the angle brackets denote ensemble averaging. The intrinsic back-scattering properties of the hydrometeors at the two polarization states enables the measurement of characteristics such as mean size, shape and spatial orientation of the precipitation particles in the radar resolution volume. These characteristics are described in terms of the back scattering matrix elements. The elements of the back scattering covariance matrix or some combination of them are used to compute the polarimetric variables. Several radar observables can now be estimated (Bringi and Chandrasekar, 2001).

### 2.2.1 Doppler spectral moments

The observed shape of the Doppler spectrum of co-polar signal can be approximated to be Gaussian (Doviak and Zrnić, 1993; Bringi and Chandrasekar, 2001). Let  $\mathbf{S}(\mathbf{v}, \boldsymbol{\theta})$  denote the Gaussian spectrum model. The parameter vector  $\boldsymbol{\theta} = [p \ v_m \ \sigma_v]^t$  describes the spectral moments of the co-polar signal. The spectral model can be written as (Bringi and Chandrasekar, 2001)

$$\mathbf{S}(\mathbf{v}, \boldsymbol{\theta}) = \frac{p}{\sqrt{2\pi\sigma_v^2}} \exp \left\{ -\frac{(\mathbf{v} - v_m)^2}{2\sigma_v^2} \right\} + \frac{2T_s}{\lambda} p_n \quad (2.6)$$

where  $p_n$  is the noise power. The corresponding covariance matrix is given by

$$\begin{aligned} \gamma(k, l, \boldsymbol{\theta}) &= p \exp \left\{ -\frac{8\pi^2\sigma_v^2 T_s^2 (k-l)^2}{\lambda^2} \right\} \exp \left\{ -j \frac{4\pi v_m T_s (k-l)}{\lambda} \right\} \\ &\quad + p_n \delta(k) \end{aligned} \quad (2.7)$$

$$k, l = 1, 2, \dots, N.$$

where  $T_s$  and  $\lambda$  are the pulse repetition time (PRT) and wavelength respectively.  $\delta(\cdot)$  is the Kronecker delta function. The zeroth, first, and second spectral moments have been used both quantitatively and qualitatively for meteorological applications.

### 2.2.1.1 Reflectivity factor

The back-scattering cross section per unit volume ( $\eta$ ) is commonly referred to as radar reflectivity. It is conventional in radar meteorology to express  $\eta_{hh} = \langle 4\pi r |S_{hh}|^2 \rangle$  (H-channel), in terms of equivalent reflectivity factor ( $Z_e$ ) as

$$Z_e = \frac{\lambda^4}{\pi^5 |K_w|^2} \eta_{hh} \quad (2.8)$$

where  $K_w$  is the dielectric factor of water. The mean received power from a resolution volume at range  $r_0$  is related to the radar reflectivity at range  $r_0$  as

$$\bar{P}_r(r_0) = \left( \frac{cT_0}{2} \right) \left[ \frac{\lambda^2 P_t G_0^2}{(4\pi)^3} \right] \left[ \frac{\pi \theta_B \phi_B}{8 \ln 2} \right] \frac{\eta_{hh}(r_0)}{r_0^2} \quad (2.9)$$

The equivalent reflectivity factor  $Z_h$  (H-channel) is related to the mean received power using (2.8) and (2.9) as

$$Z_h = \frac{1}{\pi^5 |K_w|^2} \left( \frac{2}{cT_0} \right) \left[ \frac{(4\pi)^3}{\lambda^2 P_t G_0^2} \right] \left[ \frac{8 \ln 2}{\pi \theta_B \phi_B} \right] \lambda^2 r_0^2 \bar{P}_r(r_0) \quad (2.10)$$

which is expressed in  $mm^6 m^{-1}$  or  $dBZ$  in decibel scale. The reflectivity factor for the horizontally polarized signal in  $dBZ$  can now be written as

$$Z_h[dBZ] = \hat{P}_{co}^h[dBm] + C + 20 \log r_0[km] \quad (2.11)$$

where  $C$  is the radar constant expressed in  $dB$ ,  $r_0$  is the range in  $km$  and  $\hat{P}_{co}^h$  is received power of the horizontally polarized signal expressed in  $dBm$ . The radar constant  $C$  is given by

$$C = 10 \log \left\{ \frac{10^{21}}{\pi^5 |K_w|^2} \left( \frac{2}{cT_0} \right) \left[ \frac{(4\pi)^3}{\lambda^2 P_t G_0^2} \right] \left[ \frac{8 \ln 2}{\pi \theta_B \phi_B} \right] \lambda^2 \right\} \quad (2.12)$$

and all the parameters in (2.12) are expressed in SI units (for example, CSU-CHILL radar system has  $C \approx 75$  dB). The received mean power is estimated as

$$\hat{P}_h = \frac{1}{N} \sum_{k=0}^{N-1} v_{hh}(k) v_{hh}^*(k) \quad (2.13)$$

$$\hat{P}_{co}^h = G_r + 10 \log(\hat{P}_h) \quad (2.14)$$

where  $G_r$  is the digital receiver gain and is obtained from a thorough receiver calibration procedure. The reflectivity in the vertically polarized channel is also estimated as described above.

### 2.2.1.2 Mean Doppler velocity

In addition to the received power Doppler weather radars have the ability to measure both transmitted as well as received signal phase. The relative phase shift of the received signal from the scatterers in the resolution volume is due to the Doppler shift caused by the motion of the particles. This phase shift is used to estimate the radial velocity of the particles in the resolution volume. The mean Doppler velocity  $\hat{v}$  within the resolution volume is obtained from the lag-1 auto-correlation estimate

$$\hat{R}[n] = \frac{1}{N} \sum_{k=0}^{N-2} v_{hh}(k+n)v_{hh}^*(k) \quad (2.15)$$

$$\hat{v} = -\frac{\lambda}{4\pi T_s} \arctan(\hat{R}[1]) \quad (2.16)$$

### 2.2.1.3 Doppler spectral width

The radar resolution volume consists of a large number of hydrometeors with widely varying velocities. The received signal has Doppler velocity spread about a mean Doppler velocity. This Doppler spectral width is indicative of the turbulence of the medium within the resolution volume. Assuming a Gaussian spectral shape for meteorological echo the Doppler spectrum width is estimated as

$$\hat{\sigma}_v = \frac{\lambda}{2\pi T_s \sqrt{2}} \left[ \ln \left| \frac{R(0)}{R(1)} \right| \right]^{1/2} \quad (2.17)$$

## 2.2.2 Polarimetric variables

The back-scattering properties of the hydrometeors vary with the incident polarization state due to the shape and orientation of these particles. Polarimetric variables provide addition information about the hydrometeors and also enable improved quantitative measurements of precipitation.

### 2.2.2.1 Differential reflectivity ( $Z_{dr}$ )

Differential reflectivity is defined as

$$Z_{dr} = 10 \log \left( \frac{\langle |S_{hh}|^2 \rangle}{\langle |S_{vv}|^2 \rangle} \right) = 10 \log \left( \frac{\hat{P}_h}{\hat{P}_v} \right) \quad (2.18)$$

, is a measure of mean particle shape. For example, rain drops are oblate in shape and result in positive  $Z_{dr}$ .

### 2.2.2.2 Complex co-polar correlation ( $\rho_{hv}$ )

The lag 0 complex correlation between the co-polar signals is given by

$$\hat{R}_{vvhh} = \frac{1}{N} \sum_{k=0}^{N-1} v_{vv}(k) v_{hh}^*(k) \quad (2.19)$$

The magnitude and phase of co-polar correlation coefficient is given by

$$|\rho_{HV}(0)| = \frac{|\hat{R}_{vvhh}|}{\sqrt{\hat{P}_h} \sqrt{\hat{P}_v}} \quad (2.20)$$

$$\arg \left[ \hat{R}_{vvhh}^* \right] = \psi_{dp} = \phi_{dp} + \delta \quad (2.21)$$

where  $\phi_{dp}$  is the differential propagation phase shift and  $\delta$  is the differential phase shift upon scattering. If we assume Rayleigh scattering then  $\delta \approx 0$ .

## 2.3 Single versus distributed radar environments

Current weather surveillance radar systems deployed by U.S. agencies called the Next Generation Radar (NEXRAD) and the European weather radar network are monolithic radars designed for long-range coverage with single-beam antennas. However, these long-range monolithic radars have a variety of shortcomings that limit the systems ability to meet the requirements of its varied end-users. The spatial coverage limitations are imposed by the curvature of the Earth as shown in Fig.2.2. There is no coverage at low altitudes far away from the radars and the data is inadequate

for many applications. The NEXRAD system cannot make measurements for approximately eighty percent of the troposphere's volume below 3 km altitude. This inability constrains quantitative precipitation estimates near the surface and limits the systems ability to detect the complete vertical structure of most tornadic storms. The spatial resolution of the measurements at far ranges is insufficient since the radar beam broadens as a function of range. The cross-range resolution at far ranges span between 1 km to 4 km, therefore these systems are incapable of resolving sub-km scale structures in precipitation. The current radar systems operate in "sit-and-spin" mode. This scan strategy restricts the maximum elevation angle (currently 20 degrees for NEXRAD), mainly to provide an acceptable scan update time. Despite the tremendous capabilities of monolithic radars with large single-beam antennas insufficient spatial and temporal resolution coupled with limited spatial coverage near the surface impedes quantitative precipitation estimation, detection and warning of tornadoes and flash floods. A networked radar environment concept has been proposed by Chandrasekar and Jayasumana (2001) to mitigate the above mentioned limitations of monolithic radars. The basic concept of the networked radar environment is to be able to provide good coverage in terms of accuracy and resolution to a large area through a network of radars operating as one system.

The U.S National Science Foundation established an Engineering Research Center titled the Center for Collaborative Adaptive Sensing of the Atmosphere (CASA), formed by a consortium of four universities (listed alphabetically), Colorado State University, University of Massachusetts(lead university), University of Oklahoma, and University of Puerto Rico and partnership with industry and government laboratories to create the underlying science and engineering basis for the paradigm of networked radars applied to hazardous localized weather detection, tracking and predicting. Many challenges associated with the operation of a networked radar environment is described in Chandrasekar et al. (2004).



radar. The gain of collaborative operations (network gain) is obtained by coordinating the scans of multiple radars to observe the same precipitating atmospheric phenomenon and jointly processing the observations from multiple beams with different view angles of the same scattering region. Adaptive refers to the ability of the individual radars in the network to rapidly reconfigure in response to dynamic weather conditions. The configurations of the radar waveforms, signal processing and scan strategy change in a manner that optimizes the networked radar systems ability to respond to competing end-user demands. For example, a DCAS radar network might pinpoint specific meteorological regions of interest with high spatial resolution for public warning while simultaneously mapping the horizontal wind field associated with the parent thunderstorm and providing quantitative precipitation estimates for input to distributed hydrological models. For example, Wang et al. (2008) describes the development of adaptive scan strategy for dual-Doppler observations in a networked radar environment to map wind fields. The system accomplishes this by continually adjusting the scans of multiple coordinated radars, all in response to changing weather.

#### **2.4 CASA first generation DCAS system**

The new paradigm of DCAS has been instantiated in CASA's first integrative project (IP1) test bed. The IP1 test bed is an end-to-end systems used to develop and demonstrate enabling technologies. The IP1 radar network implementation consists of four polarimetric weather radar nodes (designated with the following FCC identifiers: KSAO, KRSP, KCYR, and KLWE) shown in Fig. 2.3. The geographic location of the four radars is shown in Fig.2.4 and their geolocations listed in Table 2.1.

The IP1 radar, shown in Fig. 2.3, integrates transmitter, receiver and data acquisition subsystems in a single assembly mounted directly behind the antenna. The transmitter is magnetron based with limited agility on duty cycle and supported waveforms. The transmitter delivers a peak power of 25 kW at a maximum duty cycle of

Table 2.1: IP1 network radar nodes location.

Location	FCC Identifier	Latitude $^{\circ}$	Longitude $^{\circ}$	Altitude $m$
Chickasha	KSAO	35.0312	-97.9567	353.99
Rush Springs	KRSP	34.8129	-97.9313	414.84
Lawton	KLWE	34.6238	-98.2720	377.45
Cyril	KCYR	34.8739	-98.2514	445.30

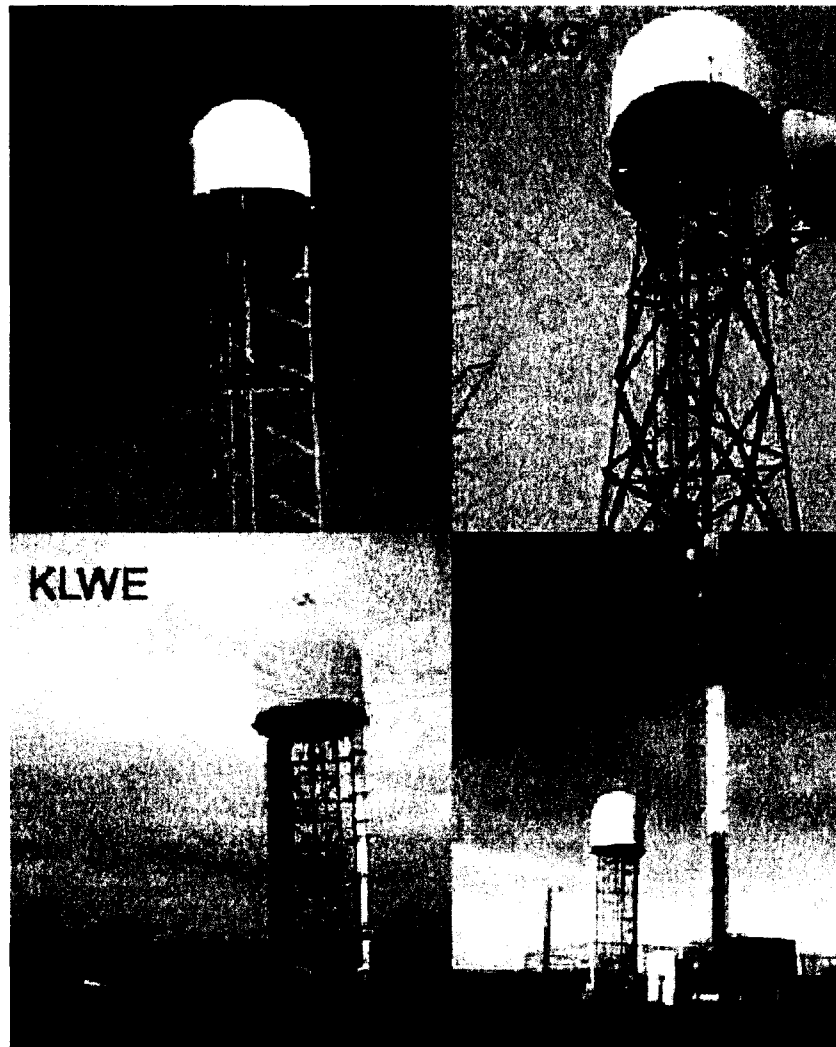


Figure 2.3: The four polarimetric radars forming the IP1 radar network.

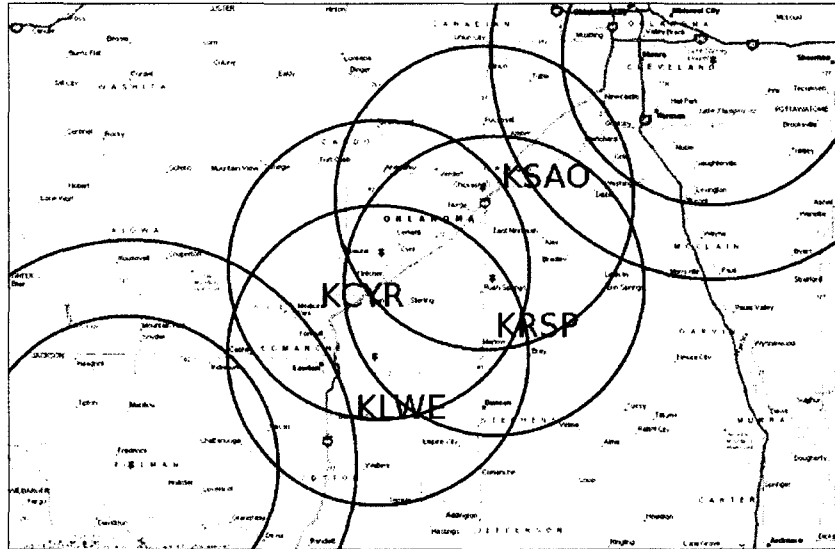


Figure 2.4: Map showing the location of each radar node in the IP1 radar network.

0.1%. The maximum pulse length is  $1 \mu s$ , which yields a maximum average power of 25 W at the maximum Pulse Repetition Frequency (PRF) of 1 kHz. To increase the PRF beyond 1 kHz, the transmitter peak power is reduced from its maximum value, which allows an increase in duty cycle. The antenna is a center-fed reflector supporting dual-polarization, mounted on an agile pedestal. A remotely programmable Direct Digital Synthesizer (DDS), together with an Automatic Frequency Control (AFC) software loop, allow the system to track the transmitted frequency and to digitally control down-conversion frequency. The receiver output is fed into a high-speed, reconfigurable, data acquisition and processing system. The data acquisition system with 14 bit A/D front end and a data processing core built on a high-performance FPGA. A more detailed description of the radar systems deployed in Oklahoma can be found in Junyent et al. (2009).

The four radar nodes are connected to a central data storage and control compute facility known as System Operation and Control Center (SOCC). The SOCC hosts a number of meteorological application for end users to use. The SOCC also hosts the Meteorological Command and Control (MCC). MCC is the software architecture that

performs the implementation of scan strategy in the IP1 radar network. In this closed loop operations, data is ingested from the individual radars, meteorological features are identified in this data, features are reported to end-users. The scan strategy of the individual radar nodes in the networked radar system is based on detected features and end-user requirements. MCC interfaces the radar control and adaptive scanning algorithms to the incoming real-time data stream. This enables adaptive steering without the need for a radar operator. The communication infrastructure provides a sustained data rate of 4 MBps between the nodes and SOCC. A more detailed description of the MCC and its performance can be found in Zink et al. (2008).

During the last three years the IP1 radar network has been operational in many Intensive Operations Periods (IOP). IP1 radar network has collected an extensive data set during the last three years. The data products generated by the radars is a result of the waveforms and advanced signal processing software implemented on the radar nodes. The development and evaluation of the waveform and processing algorithms are described in detail in this dissertation. In addition, the data products of the IP1 radar are further used in the application of networked waveform system and networked resolution enhancement technique developed in this research.

# CHAPTER 3

## SPECTRAL PROCESSING FOR DUAL POLARIZATION WEATHER RADARS

---

---

### 3.1 Introduction

Doppler weather radars have traditionally used auto-covariance based estimators to obtain the spectral moments and polarimetric variables (Doviak and Zrnić, 1993; Bringi and Chandrasekar, 2001). Advance methodologies using spectral processing has been studied in the past decade and it have been found that spectral processing offers several benefits. Spectral processing must be extensively used to phase coded signals for range ambiguity mitigation (Siggia, 1983; Sachidananda and Zrnic, 1999; Bharadwaj and Chandrasekar, 2007). Spectral processing for clutter suppression has showed improved performance for uniform pulse repetition time and staggered waveforms (Siggia and Passarelli, 2004; Sachidananda and Zrnic, 2000). Advantages of spectral processing algorithms with polarimetric radars has been shown with data collected by CSU-CHILL (Seminaro et al., 2001; Moisseev et al., 2006; Moisseev and Chandrasekar, 2007; Chandrasekar and Bharadwaj, 2009). The continuing advances in digital computing makes application of spectral processing in weather radars possible. Spectral processing is extensively used in real-time on the first generation CASA (Collaborative Adaptive Sensing of the Atmosphere) X-band radar network (Bharadwaj et al., 2007). Although, spectral processing offers many benefits there are certain limitations of using spectral processing when compared to time domain processing.

The impact of spectral processing on the spectral moments and polarimetric variables is described in this chapter. The effect of processing window on the accuracy of the estimated parameters is described in Section 3.2. Section 3.3 describes the ground clutter filter methodology in spectral domain while the performance of polarimetric retrieval using spectral clutter filter is described in Section 3.4. The results of spectral processing applied to data collected from CSU-CHILL radar is presented in Section 3.5 and finally Section 3.6 summarizes the findings about spectral processing.

### 3.2 Effect of window function

Spectral processing to estimate the spectral moments requires the use of standard window function to minimize the finite sample window effect. A rectangular window is naturally applied due to finite dwell time during the integration cycle. This leads to spectral leakage because the first side-lobe of rectangular window is only 13 dB below the main-lobe. Therefore, standard window functions are applied to estimate the power spectral density using the periodogram estimate. Let  $\mathbf{v} = [v_1 \ v_2 \ v_3 \ \dots \ v_N]^T$  be the  $N$  samples of the received signal from a given resolution volume. It is assumed that  $\mathbf{v}$  is a circular symmetric complex Gaussian random vector  $\mathcal{N}(\mathbf{0}, \Sigma)$  with a multivariate density function given by

$$f(\mathbf{v}) = \frac{1}{\pi^N \det \Sigma} \exp(-\mathbf{v}^H \Sigma^{-1} \mathbf{v}) \quad (3.1)$$

where  $\Sigma = E\mathbf{v}\mathbf{v}^H$  is the covariance matrix of the complex vector  $\mathbf{v}$  and  $H$  represents a Hermitian operator. Let  $\mathbf{W} = \text{diag}(\text{dim}(\mathbf{w}) \ \mathbf{w}/\|\mathbf{w}\|^2)$  be the window matrix applied to the received signal  $\mathbf{v}$  where  $\mathbf{w}$  is the time domain window function. The spectral coefficients are obtained by applying the normalized DFT operator  $\Phi$  (i.e.,  $\Phi\Phi^H = \mathbf{I}$ ). The modified DFT matrix that includes the effect of the window function is given by  $\Phi_m = \Phi\mathbf{W}$ . It is easy to see that  $\|\mathbf{v}\|^2 = \|\Phi_m\mathbf{v}\|^2$ , which implies the spectral coefficients provide an unbiased estimated of the signal power. The spectral coefficients have a zero mean multivariate circular symmetric complex Gaussian

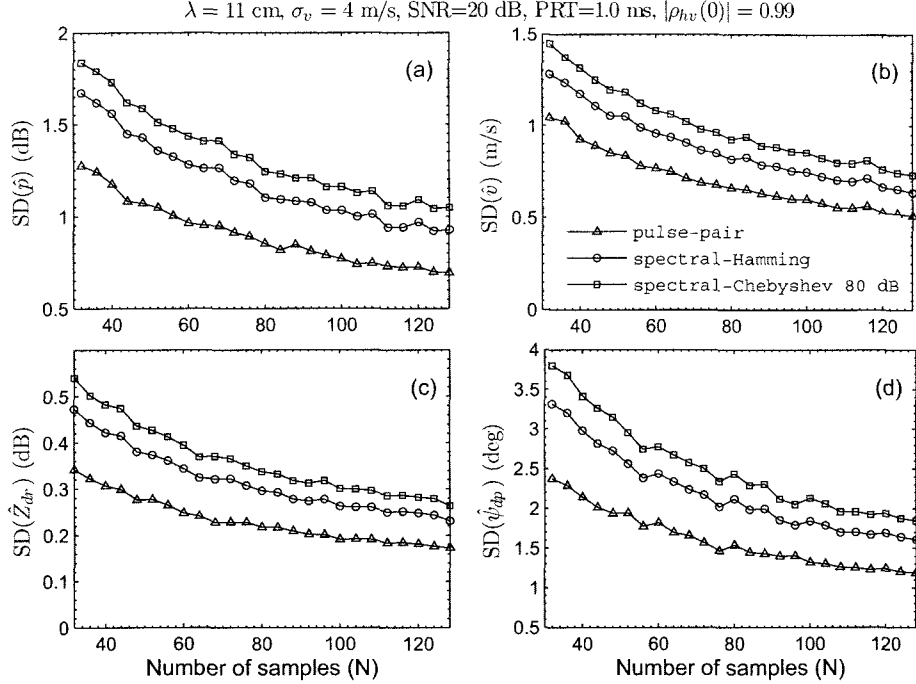


Figure 3.1: Comparison of standard deviation of spectral moments and polarimetric variables as a function of number of samples. (a). Reflectivity (b) Mean Doppler velocity (c). Differential reflectivity and (d). Differential propagation phase shift.

distribution whose covariance matrix is given by

$$\mathbf{\Gamma} = \mathbf{\Phi}_m \mathbf{\Sigma} \mathbf{\Phi}_m^H \quad (3.2)$$

The power spectral coefficients  $\mathbf{s} = |\mathbf{\Phi}_m \mathbf{v}|^2$  is a multivariate exponential distribution (Goodman, 1963; Zrnic, 1980; Brangi and Chandrasekar, 2001). It is important to observe that the diagonal elements of  $\mathbf{\Gamma}$  are not equal. The analytical analysis of such heteroskedastic Gaussian process is beyond the scope of this chapter. However, the impact of window functions on the estimates of Doppler spectral moments and polarimetric variables will be presented based on simulations. Received signal for dual-polarization radars are simulated based on the methodology presented by Chandrasekar et al. (1986).

Signals of longer length are simulated and a rectangular window is applied to simulate the rectangular window effect that naturally occurs due to finite dwell time.

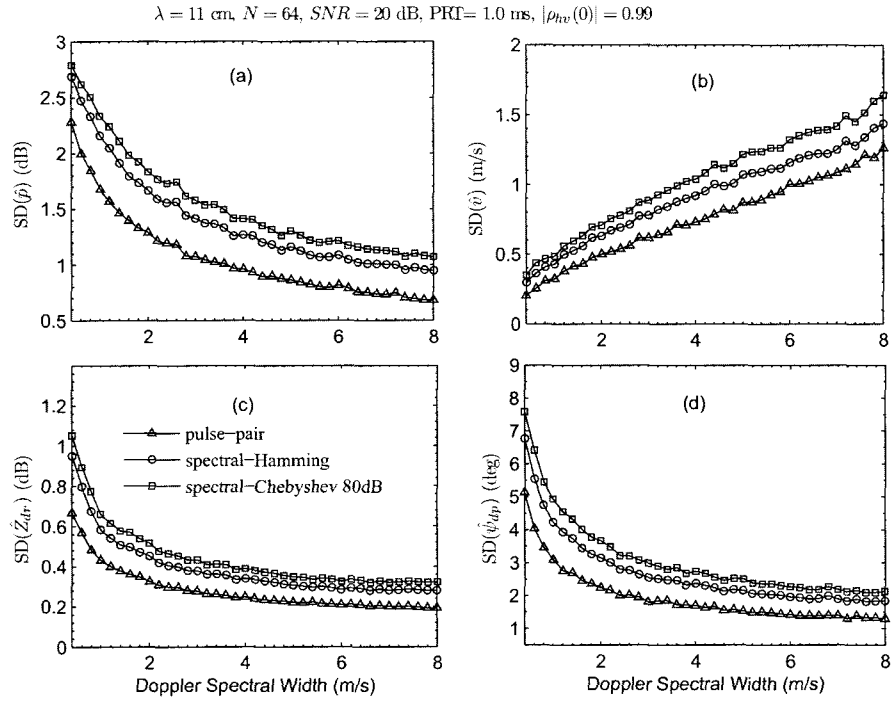


Figure 3.2: Comparison of standard deviation of spectral moments and polarimetric variables as a function of Doppler spectral width. (a). Reflectivity (b) Mean Doppler velocity (c). Differential reflectivity and (d). Differential propagation phase shift.

The simulations are performed for an S-band radar system and the signal-to-noise ratio, SNR=20 dB, is selected minimize the impact of noise on the performance of spectral processing and co-polar correlation coefficient,  $\rho_{hv} = 0.99$ , is used. Such high values of  $\rho_{hv}$  are indicative of rain and it directly influences the error statistics of the polarimetric variables (Bringi and Chandrasekar, 2001). The impact of the processing window on the spectral moments and polarimetric variables are analyzed based on the standard deviations or accuracy of the estimates. The Hamming and 80 dB Chebyshev processing windows will be considered in this section and its performance will be compared with the auto-covariance or pulse-pair estimates of spectral moments and polarimetric variables. The spectral moments and polarimetric variables are obtained as described in Bringi and Chandrasekar (2001). The standard deviation of of the spectral moments and polarimetric variables for  $\sigma_v = 4 \text{ m/s}$  as a function number of samples is shown in Fig.3.1. Figure 3.1(a), (b), (c), and (d) show the standard deviation of the estimated reflectivity, mean Doppler velocity, ZDR and differential phase shift respectively. It is clearly observed that the standard deviation of estimates from spectral processing using a processing window is higher than that obtained from pulse-pair. The standard deviation of reflectivity increases by 0.4-0.5 dB depending on the processing window. The accuracy of mean Doppler velocity is also degraded by 0.3-0.4 m/s. The standard deviation of ZDR and differential phase are increased by 0.1-0.2 dB and 0.5-1.5 degrees respectively. The increase in standard deviation is directly related to the spectral side-lobe performance of the processing window.

The standard deviation of the estimated spectral moments and polarimetric variables as a function of spectral width is shown in Fig. 3.2. The increase in standard deviation of reflectivity, ZDR and differential phase is much more for narrower spectral width ( $\sigma_V \leq 2 \text{ m/s}$ ) when compared to larger spectral width ( $\sigma_V > 2 \text{ m/s}$ ). There is an increase of 0.2-0.3 dB in the standard deviation of ZDR for narrower spectral width and an increase of 0.1-0.15 dB for larger spectrum width. The increase in

standard deviation in reflectivity is also significant. The accuracy of reflectivity is degraded by 0.5-0.6 dB while that of differential phase is degraded by 1-3 degrees.

The degradation of accuracy is consistent for all the parameters when a processing window is used. The use of more aggressive processing window will significantly degrade the accuracy of the spectral moments and polarimetric variables. It is important to acknowledge the fact that spectral processing that uses processing window does have a drawback of increasing the standard deviation of spectral moments and polarimetric variables.

### 3.3 Spectral clutter filtering

Spectral processing offers a better way to effectively mitigate ground clutter contamination. Ground clutter echo is the signal back-scattered from stationary ground targets. Since ground clutter echoes are from the received signals of stationary targets their mean Doppler velocity is zero. This property of clutter has been used to filter ground clutter by designing high pass filters that pass weather signals while notching clutter signals. Traditionally ground clutter filtering has been performed using infinite impulse response (IIR) filters (Groginsky and Glover, 1980). However, such simple filtering techniques induce bias in the estimated spectral moments. The rapid growth in signal processor technology has tremendously increased the computational power of the signal processor. The current signal processor employed in weather radars are general purpose compute servers. Hence, it is feasible to incorporate spectral processing for clutter filtering.

The observed shape of the Doppler spectrum of co-polar and clutter signal can be approximated to be Gaussian (Doviak and Zrnić, 1993; Bringi and Chandrasekar, 2001). Therefore, we model the observed signal as having two Gaussian spectral components, one for co-polar signal and one for clutter signal. Let  $\mathbf{S}(\mathbf{v}, \boldsymbol{\theta})$  denote the Gaussian spectrum model. The parameter vector  $\boldsymbol{\theta} = [p_c \sigma_c p v w]^t$  describes the spectral moments of the clutter and co-polar signals. The subscripts c indicates the

spectral moments of clutter signal. The spectral model can be written as (Bringi and Chandrasekar, 2001)

$$\begin{aligned} \mathbf{S}(\mathbf{v}, \boldsymbol{\theta}) = & \frac{p_c}{\sqrt{2\pi\sigma_c^2}} \exp\left\{-\frac{\mathbf{v}^2}{2\sigma_c^2}\right\} + \\ & \frac{p}{\sqrt{2\pi w^2}} \exp\left\{-\frac{(\mathbf{v}-v)^2}{2w^2}\right\} + \frac{2T_s}{\lambda} p_n \end{aligned} \quad (3.3)$$

where  $p_n$  is the noise power. The corresponding covariance matrix is given by

$$\begin{aligned} \gamma(k, l, \boldsymbol{\theta}) = & p_c \exp\left\{-\frac{8\pi^2\sigma_c^2 T_s^2 (k-l)^2}{\lambda^2}\right\} + \\ & p \exp\left\{-\frac{8\pi^2 w^2 T_s^2 (k-l)^2}{\lambda^2}\right\} \exp\left\{-j\frac{4\pi v T_s (k-l)}{\lambda}\right\} + p_n \delta(k) \\ k, l = & 1, 2, \dots, N. \end{aligned} \quad (3.4)$$

where  $T_s$  and  $\lambda$  are the pulse repetition time (PRT) and wavelength respectively.  $\delta$  is the Kronecker delta function. Siggia and Passarelli (2004) suggested a methodology to use a Gaussian model to filter the ground clutter signal. The following paragraphs describe the methodology used to filter clutter in the spectral domain. The main idea of fitting a Gaussian model to the observed signal spectrum is the same as described by Siggia and Passarelli (2004) but there are differences in the processing steps involved in filtering the clutter signal.

A window function is applied to the received signal before the periodogram estimate of the spectrum is obtained. The window function has an impact on the accuracy of the estimated moments as described in the the previous section. The first step in the filtering process is the estimation of the spectral noise floor. The spectral coefficients are sorted and the mean of the lower quantile gives the spectral noise floor estimate. The number of spectral coefficients within a quantile is empirically obtained and usually about 25% of the total number of spectral coefficients is a good enough. It is important to note that the spectral noise floor is overestimated when it is estimated from aliased spectrum or when spectral width is very large. The noise power obtained from spectral noise floor can be greater than the system thermal noise

floor. This increase in noise floor is due to the phase noise of the transmitter. Parts of the signal power spills over as noise due to the system phase noise.

The next step is obtaining the clutter spectral model based on the that clutter spectrum is centered at zero Doppler velocity. Clutter spectral width is very narrow and increases with scan speed. Clutter spectral width is on the order of 0.1 m/s to 0.3 m/s. The processing window function used also widens the spectral width of clutter. A fixed clutter spectral width is assumed and the effect of the processing window is applied to obtain the clutter spectral width. The clutter model power is obtained by fitting the a least squares curve to the spectral coefficients around zero Doppler region. Typically, three points are sufficient as clutter is very narrow compared to the frequency resolution of the spectrum.

The number of spectral coefficients to notch is obtained by the intersection of the clutter spectral model and the spectral noise floor,  $\tilde{p}_n$ . The number of notch points  $n$  is given by

$$n = \left\lfloor \frac{4\sigma_c T_s}{\lambda} \sqrt{2 \ln \left[ \sqrt{2\pi} \sigma_c \left( \frac{p_c}{\tilde{p}_n} \right) \right]} \right\rfloor \quad (3.5)$$

where  $\lfloor \cdot \rfloor$  is the floor function to extract the integer part. The clutter signal is notch filtered with  $n$  spectral coefficients around zero Doppler.

An initial estimate of the spectral moments is obtained from the notch filtered spectrum. A Gaussian model of the weather echo is obtained using the moments. The notch filtered region is interpolated with the Gaussian model. The process of interpolation is recursively done till the a convergence in the estimated spectral moments is reached. The convergence of the recursive interpolation is set by the change in estimated power and velocity. The iterations are stopped when change in power is less than 0.1 dB and change in velocity is 0.05% of the Nyquist velocity. The interpolation of the notched region minimizes the bias in the power and velocity when the weather echo and clutter co-exist. However, the recovery of weather echo is not

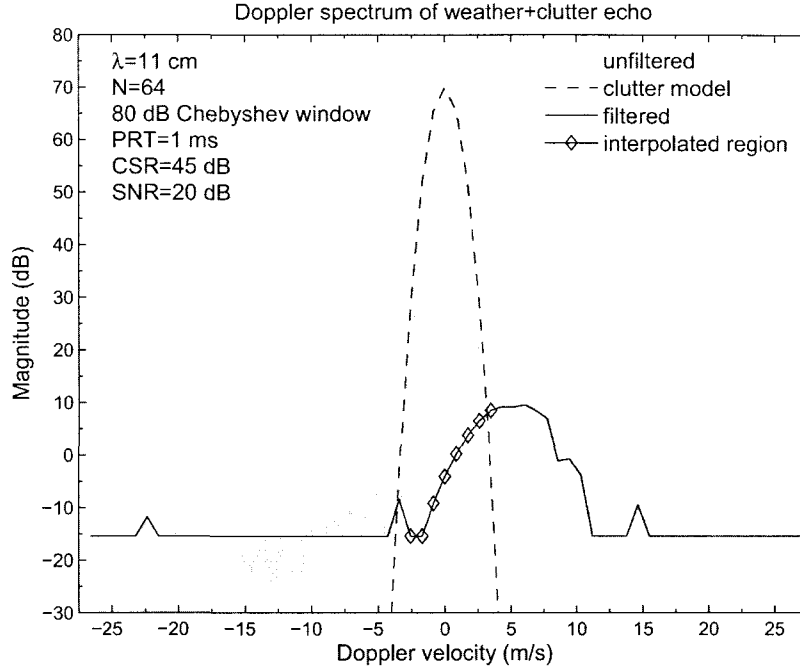


Figure 3.3: Illustration of spectral clutter filtering using a Gaussian model.

satisfactory when weather signal with narrow spectral width overlays on the clutter signal. This shortcoming is inevitable for any clutter filtering technique. This technique is summarized in Fig.3.3 where a simulation is carried out at S-band with  $SNR = 20 \text{ dB}$  and at clutter-to-signal ratio,  $CSR = 45 \text{ dB}$  with  $T_s = 1 \text{ ms}$ . The dashed line shows the clutter model obtained from the observed spectrum while the solid black line shows the weather echo. The diamonds indicates the notch filtered region that has been interpolated using a Gaussian model.

Simulations were carried out for an S-band radar ( $\lambda = 11 \text{ cm}$ ) with  $N = 64$  for a waveform operating at a pulse repetition time,  $T_s = 1 \text{ ms}$ . The signal-to-noise ratio was set at 20 dB and the clutter-to-signal ratio was set to 40 dB. The simulations were performed for spectral widths of  $\sigma_v = 2 \text{ m/s}$  and  $\sigma_v = 4 \text{ m/s}$ . The errors in the estimated moments obtained from spectral processing using a 80 dB Chebyshev processing window were observed by varying the mean Doppler velocity. Figure 3.4

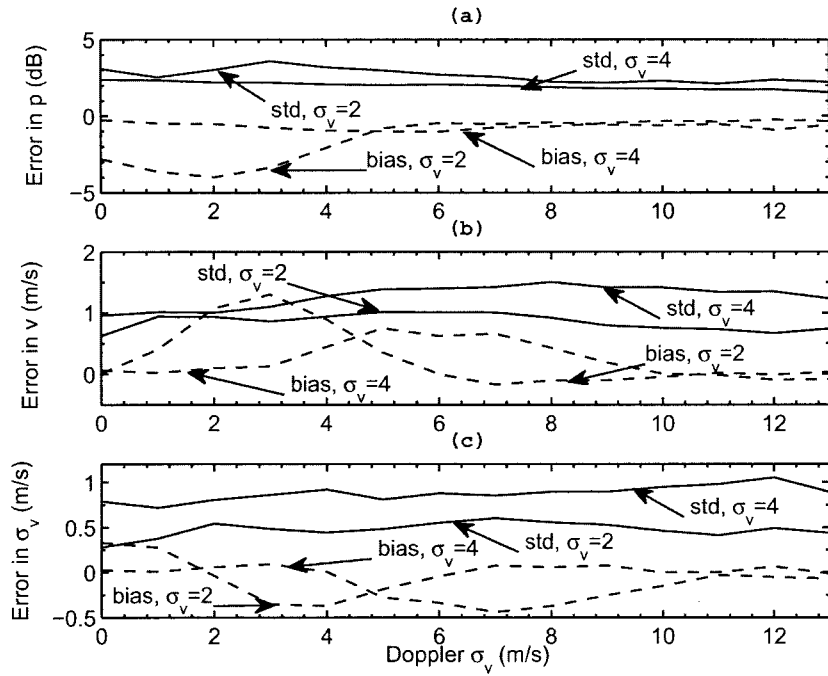


Figure 3.4: Error in the estimated spectral moments (a) Reflectivity (b) Mean Doppler velocity (c) Spectral width. The signal has been simulated for  $N = 64$  samples at  $\lambda = 11$  cm with  $T_s = 1$  ms and  $CSR = 40$  dB.

shows the bias and standard deviation of estimated reflectivity, mean Doppler velocity and spectral width. The bias in reflectivity (Fig. 3.4(a)) is within 1 dB for larger spectral width but is much larger than 1 dB for narrow spectral width when the weather echo is in the vicinity of zero Doppler velocity. This is understandable as most of the weather echo is notched out. The standard deviation of reflectivity is on the order of 2 dB. The bias and standard deviation of mean velocity and spectral width (Fig. 3.4(b)& (c)) are within acceptable range.

### 3.4 Retrieval of polarimetric variables

Hitherto, we considered the retrieval of Doppler spectral moments in the presence of ground clutter. In this section we focus on the retrieval of polarimetric variables that are estimated in the simultaneous transmit and receive (STAR) mode or hybrid mode (Bringi and Chandrasekar, 2001). In the STAR mode only the co-polar signals are available which provide us differential reflectivity ( $Z_{dr}$ ), differential propagation phase ( $\phi_{dp}$ ) and lag-0 co-polar correlation coefficient ( $\rho_{hv}$ ). Since, signals from two channels are used to estimate the polarimetric variables it is very critical that identical processing be performed on both the horizontal (H) and vertical (V) polarization channels. There are two processing steps that can decorrelate the H-channel and V-channel signals. Firstly, the clutter power and therefore the clutter model, are not identical for both the channels. The number points to notch is obtained as

$$n = \max(n_h, n_v) \tag{3.6}$$

where  $n_h$  and  $n_v$  are the notch widths obtained as described in Section 3.3. Secondly, the spectral noise floor in the H-channel and V-channel are not identical. Since the polarimetric variables are obtained from the complex spectral coefficient it is important to notch identical points. Although, the mismatch in notch points do not affect the complex co-polar correlation it is necessary for ZDR computation. The errors in the estimated polarimetric variables are shown in Fig. 3.5. The simulations

are performed by randomly varying the polarimetric variables of clutter and uniformly varying the mean Doppler velocity of the weather echo. The simulation parameters are the same as in Section 3.3. The bias in estimated ZDR is within 0.1 dB for larger spectral width but increases beyond 0.1 dB when the spectral width is narrow and the weather echo is close to zero Doppler velocity (see Fig. 3.5(a)). The standard deviation of ZDR is 0.5-0.6 dB even when the weather signal is not close to zero Doppler velocity. This increase is due to the processing window applied for minimizing spectral leakage. The standard deviation of estimated  $\phi_{dp}$  is about 5 degrees for narrow spectral width when the echo is not close to zero velocity and there is negligible bias in  $\phi_{dp}$  estimate as shown in Fig. 3.5(b). There is a small drop in  $\rho_{hv}$  which is less than 0.01 as seen in Fig. 3.5(c). This drop is due to the residual clutter in the notch filtered signal.

### 3.5 Results

The spectral clutter filtering methodology was implemented on raw time series data collected with the CSU-CHILL radar. The CSU-CHILL radar operates at S-band ( $\lambda = 0.11 \text{ cm}$ ) and operates with two identical transmitters for horizontal polarization and vertical polarization. Time series was collected with a waveform operating at a pulse repetition time of 1 ms. The data obtained is from a snow storm with blizzard conditions on Dec 20, 2006 at 23:58:19 UTC. The raw time series was filtered using a spectral processing which used a 80 dB Chebyshev window with  $N = 64$ . The snow storm is spread over a large area in northern Colorado. The coverage volume of the radar includes very strong ground clutter from the Rocky mountains. Figure 3.6 shows the filtered and unfiltered spectral moments. The strong clutter from the mountains can be observed from 210-300 degrees in azimuth in addition to some strong ground clutter close to the radar (Fig. 3.6(a)). Most of the clutter is suppressed using spectral processing as seen in Fig. 3.6(b) except for regions where there is residual clutter in the mountains. The Doppler velocity in clutter contaminated area is zero as seen over

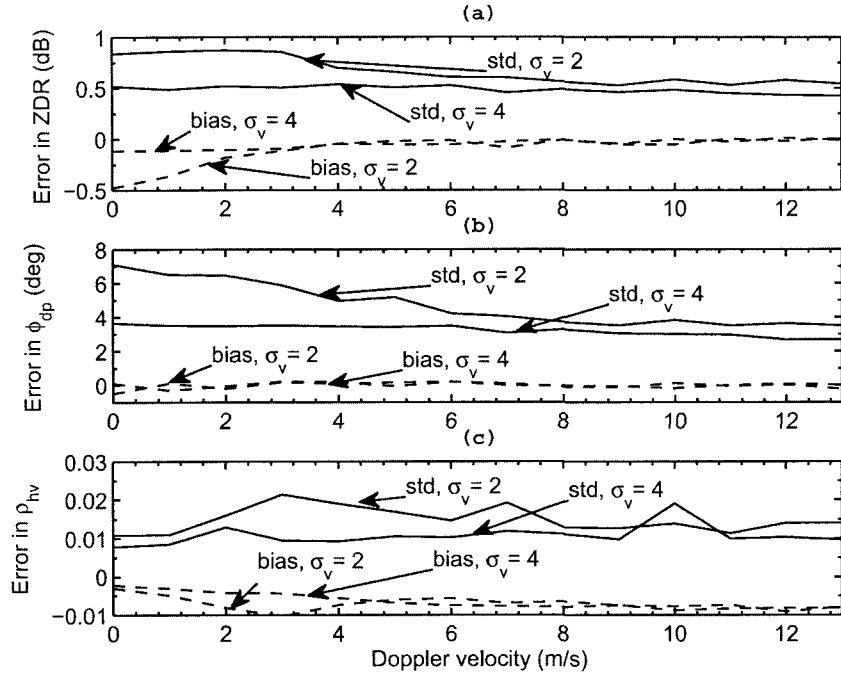


Figure 3.5: Error in the estimated polarimetric variables (a) Differential reflectivity (ZDR) (b) Differential propagation phase  $\phi_{dp}$  (c) Lag 0 co-polar correlation coefficient ( $\rho_{hv}$ ). The signal has been simulated for  $N = 64$  samples at  $\lambda = 11$  cm with  $T_s = 1$  ms and  $CSR = 40$  dB.

the mountains (Fig. 3.6(c)). However, the filtered signal is able to retrieve the velocity even in the strong clutter areas of the mountains (Fig. 3.6(d)). The spectral width over the mountain is very narrow before filtering (Fig. 3.6(e)) but shows increased spectral widths after filtering which is more indicative of blizzard conditions. The polarimetric variables before and after filters are compared side-by-side in Fig. 3.7. The features of ZDR are more prominent in rain when compared to snow. However, the clutter contaminated ZDR close to the radar and over parts of the mountain are negative before filtering (Fig. 3.7(a)) but are recovered at most points using spectral processing (Fig. 3.7(b)). The improvement in differential phase measurements can be seen in the region close to the radar (Fig. 3.7(c) &(d)).

### 3.6 Summary

Spectral processing will be ubiquitous in the near future and therefore it is important to understand the performance of the processing algorithms that use spectral processing. Based on the results from simulations it is observed that the accuracy of both, spectral moments and polarimetric variables, degrade when estimated from spectral processing that use processing window. It is recommended to use spectral processing based on the processing needs. Spectral processing is extensively used in clutter filtering and overlaid echo suppression. The performance of spectral clutter filter were presented for polarimetric variables. The results presenting the statistics were based on simulations. In addition, the performance of spectral clutter filtering for polarimetric variables were demonstrated with raw time series collected by CSU-CHILL radar.

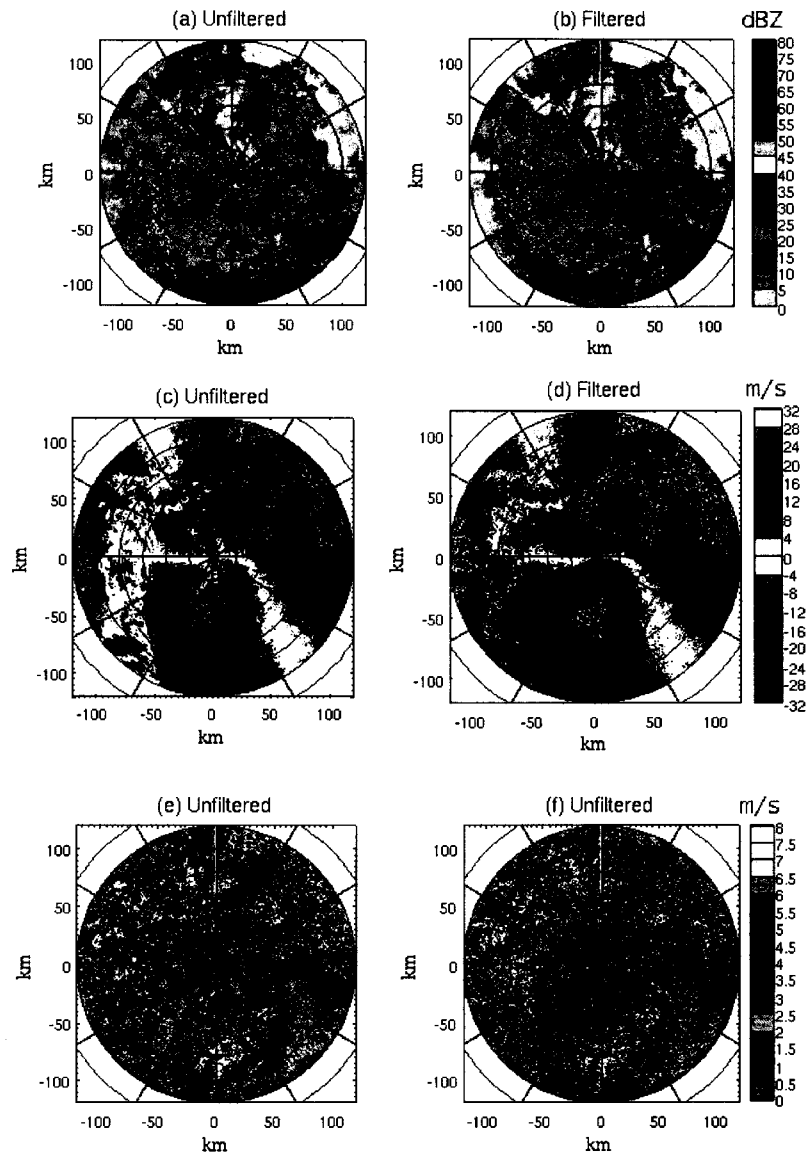


Figure 3.6: Comparison of estimated spectral moments with pulse-pair and spectral processing (a) Reflectivity from pulse-pair (b) Reflectivity from spectral processing (c) Doppler velocity from pulse-pair (d) Doppler velocity from spectral processing (e) Spectral width from pulse-pair and (f) Spectral width from spectral processing. The data obtained is from a snow storm with blizzard conditions on Dec 20, 2006 at 23:58:19 UTC.

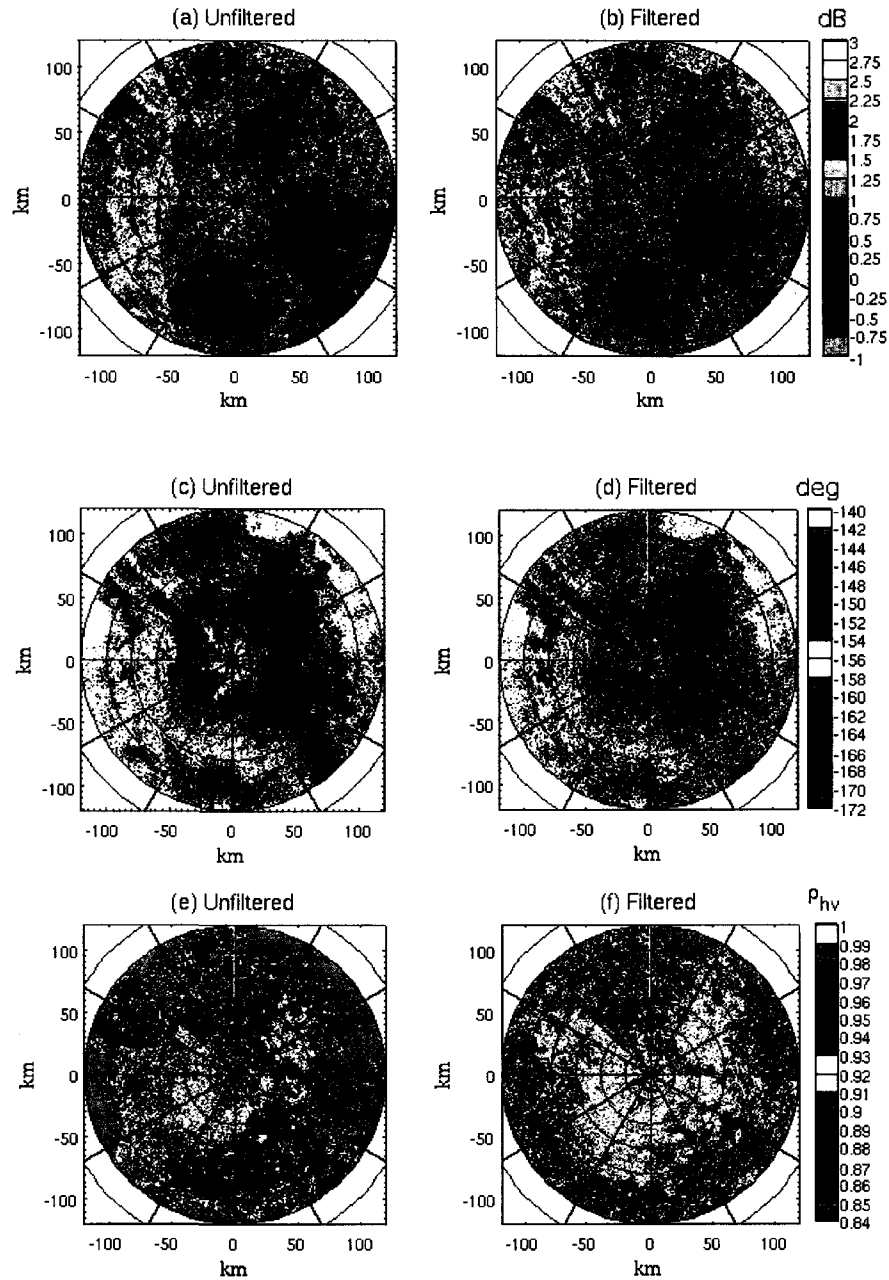


Figure 3.7: Comparison of of estimated polarimetric variables with pulse-pair and spectral processing (a) Differential reflectivity from pulse-pair (b) Differential reflectivity from spectral processing (c) Differential phase from pulse-pair(d) Differential phase from spectral processing (e) Co-polar correlation coefficient from pulse-pair and (f) Co-polar correlation coefficient from spectral processing. The data obtained is from a snow storm with blizzard conditions on Dec 20, 2006 at 23:58:19 UTC.

CHAPTER 4  
WAVEFORM DESIGN AND PROCESSING FOR THE CASA  
X-BAND RADAR SYSTEMS

---

---

#### 4.1 Introduction

The Center for Collaborative Adaptive Sensing of the Atmosphere (CASA), an engineering research center (ERC) established by the National Science Foundation (NSF) deployed its first generation network of four low-power, short-range, X-band, dual-polarized Doppler weather radars known as Networked Radar System (NETRAD). The short range CASA radars have range overlay and velocity folding problems with conventional pulse-pair processing. The first testbed of X-band radar systems (developed within the ERC) is deployed in central Oklahoma called IP-1 (Integrated Project 1). The IP1 radar network consists of four polarimetric weather radar nodes at Cyril (KCYR), Chickasha (KSAO), Rush Springs (KRSP), and Lawton (KLWE). X-band radars with conventional uniform pulsing will have low unambiguous velocity, and increasing the PRF will result in multiple trip overlays since storms can extend over a large distance. In addition, the radar systems deployed use a  $2^\circ$  beam width antenna and are intended to make observation close to the ground. The radar observations with such a system will be severely contaminated by ground clutter (Junyent et al., 2009). The major challenges associated with the deployment of such a networked of short range of radar has been described by Chandrasekar et al. (2004). It is important to address all the above mentioned issues when designing waveforms and associated processing algorithms.

The main objective of designing waveforms is to provide spectral moments and polarimetric variables with desired accuracy and to mitigate the effect of clutter and range-velocity ambiguity. Traditionally, operational radars have operated with simple uniform PRF waveforms with IIR/FIR clutter filter and pulse-pair processing (Groginsky and Glover, 1980; Doviak and Zrnić, 1993; Bringi and Chandrasekar, 2001). Specific waveforms and processing methodologies have been proposed to mitigate range-velocity ambiguities and ground clutter contamination. Phase coding technique to mitigate range overlaid (Siggia, 1983; Sachidananda and Zrnic, 1999) and staggered waveforms for velocity unfolding (Zrnic and Mahapatra, 1985; Holleman and Beekhuis, 2003; Joe and May, 2003; Cho, 2005b) have been proposed and evaluated individually. Similarly clutter filtering has been proposed and tested (Groginsky and Glover, 1980; Sachidananda and Zrnic, 2000; Siggia and Passarelli, 2004; Cho, 2005a) with primary emphasis being only on clutter filtering. However, waveforms and processing methodologies that jointly implement phase coding, dual-PRF and ground clutter filtering into an operational system using adaptive spectral processing has seldom been used operationally. This chapter presents results from CASA's IP1 radar system that takes on the challenging task of combining phase coding, dual-PRF and adaptive spectral processing into an operational system. The advent of modern signal processing techniques and computational power enables us to use complex waveforms and processing to meet the requirements.

This chapter presents waveform design and processing methodologies that jointly consider clutter suppression, ambiguity mitigation, operational requirements and hardware limitations for CASA's IP1 radars. Section 4.2 presents the challenges associated with waveform design for X-band. The hardware and operational requirements for CASA's IP1 radar network are presented in Section 4.3. The performance of waveforms at X-band for clutter suppression is described in Section 4.4. Section 4.5 describes the dual-PRF waveform for ambiguity mitigation and performance of dual pulse repetition frequency waveform in the presence of clutter and a novel spatial

filter to minimize the errors in unfolding velocities. Section 4.6 presents the results from the waveform implemented in the operational IP1 radar network. A description of the waveforms, the real-time environment and performance is presented in Section 4.6. The chapter concludes with a summary in Section 4.7.

## 4.2 Waveform design perspective

The objective of waveform design for Doppler weather radars is to provide a waveform that minimizes errors and ambiguity in Doppler spectral moment estimates. The following sections describe the issues that are considered when designing waveforms for Doppler weather radars.

### 4.2.1 Range-velocity ambiguity

Doppler weather radars transmitting pulses with uniform pulse repetition frequency (PRF) have a fundamental limitation on maximum unambiguous range ( $r_{max}$ ) and maximum unambiguous velocity ( $v_{max}$ ) given by

$$r_{max}v_{max} = \frac{c\lambda}{8} \quad (4.1)$$

In (4.1),  $\lambda$  is radar wavelength and  $c$  is the velocity of light. The  $r_{max}v_{max}$  limit reduces by a factor of three when the wavelength is changed from S-band to X-band. There is always a trade off between  $r_{max}$  and  $v_{max}$  (range-velocity ambiguity). Precipitation particles can be distributed over a large area and the dynamic range of the radar reflectivity can be as high as 80 dB which results in range overlay. Velocity measurements can span  $\pm 50$  m/s in severe storms resulting in velocity folding. Networked radar system deployed by CASA are primarily for “Targeted applications” such as tornado detection, flash flood monitoring, and hydrological applications. Such applications will have range overlay and velocity folding problems with conventional pulse-pair processing. The IP1 testbed with smaller X-band radar systems developed within CASA (Junyent et al., 2009) is a facility to demonstrate networked radar operations for targeted applications. Figure 4.1 shows the range-velocity limitation of

an X-band radar compared to S-band radar. X-band radars have a low unambiguous velocity due to their short wavelength, and increasing the pulse repetition frequency (PRF) will result in multiple trip overlays since storms can extend over a large distance. It can be observed that range-velocity ambiguity is more severe for X-band radars compared to the conventional S-band. For example, a commonly used one millisecond PRT at S-band results in an unambiguous velocity of only 7.5 m/s at X-band compared to the 25 m/s at S-band.

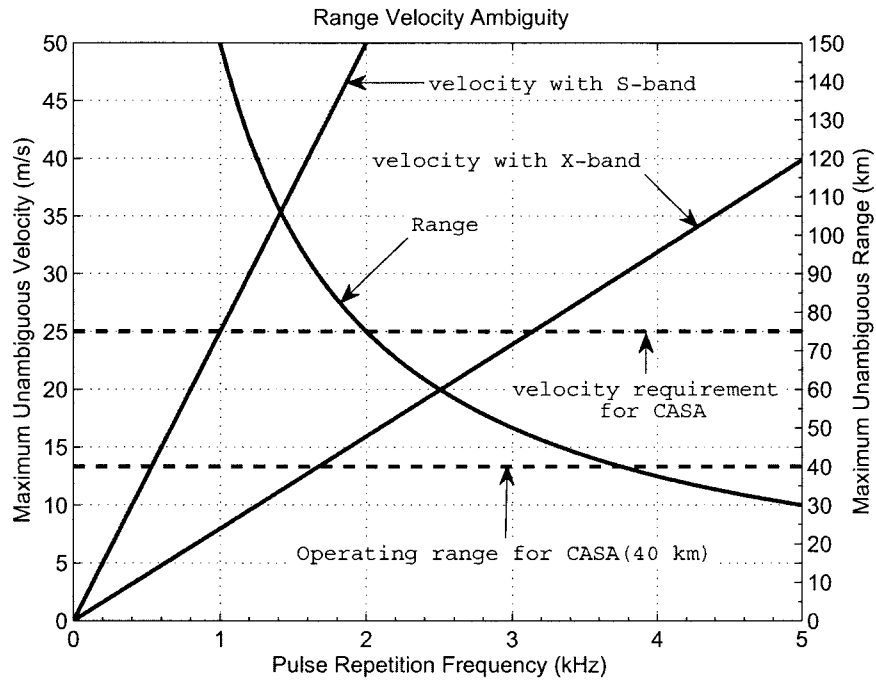


Figure 4.1: Comparisons of range-velocity limitations for S-band and X-band radars

Several range-velocity ambiguity mitigation schemes have been proposed in the past. Staggered pulse-repetition-time (PRT) pulsing can be used to increase the unambiguous velocity Zrnic and Mahapatra (1985), and Golestani et al. (1995) extends this concept for dual-polarized radars. Random phase coding of the transmitted pulse was proposed by Siggia (1983) to mitigate range overlay, and a systematic phase code and associated processing was suggested in Sachidananda and Zrnic (1999). A sys-

tematic phase code has been known to give better performance than random phase codes but requires a phase controlled amplifier klystron, traveling wave tube (TWT) or solid-state transmitter. All the above methods have been tested with S-band and C-band radars.

#### 4.2.2 Ground Clutter

The CASA concept advocates radars designed for “targeted applications” at short ranges. A dense network of short range radars mitigate the Earth’s curvature problem and provide finer resolution with smaller antennas when compared to their S-band counterparts. However, radar observations at short ranges are contaminated by ground clutter. Ground clutter is the radar return from non-meteorological targets that bias the reflectivity and velocity estimates. Ground clutter at close range could come from side lobes or main lobe of the antenna, depending on the radar altitude or the phenomena being observed. Specifically, designing radars for short-range operation needs emphasis on clutter mitigation. At close ranges the equivalent radar reflectivity due to clutter can easily be in the 40 to 60 dBZ range, whereas the phenomena being observed, such as light rain or tornadoes may have echoes in the range of 20 to 40 dBZ. Therefore, the waveform must consider clutter mitigation along with range-velocity ambiguity.

### 4.3 Design Considerations

Waveforms for the individual radar nodes are based on IP1 operational requirements such as scan speeds, volume coverage pattern, and system/hardware limitations (imposed by budgetary/market constraints) in addition to their ability to mitigate range-velocity ambiguities and suppress ground clutter echoes. The waveform considered for X-band implementation includes phase coding and multi-PRF capabilities using spectral processing. The advent of high-speed digital processors and extensive computational power with the capability of real time spectral processing makes

such waveforms viable for operational use. The number of waveforms for the radar is constrained by the hardware and system requirements. The following sections describe the requirements for the IP1 radars that impose constraints on the IP1 radar waveform.

### 4.3.1 Operation Requirements

The main goal of CASA is to provide an efficient system for hazardous weather detection and prediction using a collaborative network of radars operating in a closed loop with end-users. The radars are intended to provide short-range coverage with a range of 40 km for each node. In order to efficiently detect different weather phenomenon each radar must provide data that satisfies the recommended data specifications. Each low powered radar must provide a sensitivity of at least 10 dBZ at 30 km (unattenuated) with an accuracy of 1 dB . The radars must also provide a Nyquist velocity of at least 25 m/s when operating in the Doppler mode with an accuracy of 1 m/s at an SNR of 10 dB. The accuracy of both reflectivity and velocity mentioned above will be applicable in the absence of clutter filtering. In addition to the basic requirements there are several spatial and temporal aspects in the data specifications based on weather detection algorithms. One of the main requirement based on detection algorithms is the need for an azimuthal sampling resolution of 1 degree. The azimuthal sampling resolution directly places a constraint on the dwell time and scan speed.

The system “heartbeat” of CASA’s first generation radar network is 40s. This means that the entire system updates its state every 40 seconds. In order to operate within the “heartbeat” the scan speed of the radar nodes is very high (in excess of 15 deg/s). The radar operates in a surveillance mode to assess the overall weather pattern and updates the feature repository. The captured features of the weather event are used to generate new radar scan strategies.

### 4.3.2 Hardware requirements

In order to make a network of radars affordable, one of the drivers is to work with smaller less expensive radars, which dictates the hardware requirements. The first generation CASA radar systems are magnetron based with limited agility on duty cycle and supported waveforms. Junyent et al. (2009) gives a complete description of the radar system along with its features. The specifications of the radar system is listed in Table 4.1. The transmitter can deliver a maximum peak power of 25 kW at a duty cycle of 0.1%. Hence only a PRF of 1.5 kHz can be used at the peak power of 25 kW. The transmitter can be tuned below its maximum peak power allowing one to increase the duty cycle, which is used to accommodate the higher PRF bursts. For example, a 3.3 dB reduction in peak power will enable the transmitter to pulse at a PRF of 3.2 kHz. A direct result of lowering the peak power to accommodate higher PRF is the loss in sensitivity. However, the maximum PRF that can be achieved is still limited by the duty cycle and any high PRF pulse train that is beyond the rated duty cycle has to be compensated an operating with a lower PRF. In addition to loss in sensitivity there will be significant frequency drifts in the magnetron due to temperature fluctuations if the PRF is very high. There is also a limitation on the ability to phase code the transmit pulses because a magnetron based system has a random start-up phase. Therefore, random phase coding is the only scheme that can be implemented.

### 4.4 Ground clutter filtering

Ground clutter echo is the signal back-scattered from fixed targets such as terrain, buildings, trees and non-meteorological targets. The ground clutter echo from antenna side-lobes or main-lobe has zero mean Doppler velocity. This property is used to filter or eliminate the contamination caused by ground clutter. Ground clutter filtering is performed by applying a notch filter centered at zero Doppler velocity.

Table 4.1: IP1 radar node design characteristics

<b>Transmitter</b>	
Type	Magnetron
Center frequency	$9410 \pm 30$ MHz
Peak power output	8.0 kW (per channel)
Average power output	12 W (per channel)
Pulse width	660 ns
Polarization	Dual linear, H and V
Max. Duty Cycle	0.16%
<b>Antenna and Pedestal</b>	
Type (diameter)	Parabolic reflector (1.2 m)
3-dB Beam width	$1.80^\circ$
Gain	38.0 dB
Azimuth scan rate	up to $240^\circ/s$
Elevation scan rate	up to $30^\circ/s$
Acceleration	up to $120^\circ/s^2$
<b>Receiver</b>	
Type	Dual-channel digital
Dynamic range (BW=1.5 MHz)	103 dB
Noise figure	6.5 dB
Sampling rate	100 MSps
Dynamic range (BW=500 KHz)	113 dB
Data transfer rate	88.3 MBps
Decimation factor	Adjustable
Video Bandwidth	Adjustable

Elliptic filters have been traditionally used for clutter filtering. The advent of high speed digital processors enables clutter filtering in spectral domain. Siggia and Pasarelli (2004) suggested an adaptive spectral filtering technique called Gaussian Model Adaptive Processing (GMAP) to filter ground clutter. In this chapter an adaptive spectral domain filter similar to GMAP is used to suppress ground clutter. The following paragraph provides a brief description of the assumption and methodology for clutter filtering in the spectral domain.

The spectral clutter filtering algorithm operates on the two polarization channels jointly and does not process the horizontal polarization channel and vertical polarization channel independently. The assumptions made for the processing are as follows:

- i. Both clutter and weather spectral density function are Gaussian (Doviak and Zrnić, 1993; Bringi and Chandrasekar, 2001). The clutter contaminated weather echo can be modeled with a spectral density given by

$$S_m(\mu) = \frac{S_{0c}}{\sqrt{2\pi\sigma_c^2}} \exp\left\{-\frac{v_k^2}{2\sigma_c^2}\right\} + \frac{S_0}{\sqrt{2\pi\sigma_v^2}} \exp\left\{-\frac{(v_k - v_m)^2}{2\sigma_v^2}\right\} + N_0, \quad (4.2)$$

where  $\mu = [S_{0c}, \sigma_c, S_0, v_m, \sigma_v, N]^T$  with the subscripts “c” indicating clutter parameters and  $N_0$  is the noise power density.

- ii. Clutter signal has a very narrow Doppler spectrum width ( 0.2-0.3 m/s) and is centered on zero Doppler velocity.
- iii. The spectral width of weather is greater than spectral width of clutter.
- iv. The distribution of co-polar correlation for clutter is fairly wide.  $|\rho_{hv}(0)|$  is very low for side-lobe clutter while it can be very high for main-lobe clutter.
- v. The co-polar correlation of precipitation is very high (0.99 or greater).

- vi. The noise power density  $N_0$  is the superposition of system noise floor and noise contribution due to phase noise.

The processing steps involved in spectral clutter filtering are as follows:

- i. A window function is applied to the received signal in both H and V polarization channels. The complex spectral coefficients are computed using the DFT and the periodogram estimate of the spectral density in both channels is estimated.
- ii. The spectral noise floor in both the polarization channel is obtained from the sorted power spectral coefficients.
- iii. The clutter power is computed from the samples around zero Doppler velocity
- iv. The Gaussian clutter model is fit based on the clutter power and an *a priori* clutter spectral width
- v. The Gaussian clutter model along with the spectral noise floor in each polarization channel is used to determine the width of the spectral clipper.
- vi. The spectral clipper and noise floor from both polarization channels are used to notch the complex spectral coefficients in each polarization channel.
- vii. The polarimetric variables are computed from the filtered complex spectral coefficients.
- viii. A Gaussian weather spectral density is recursively fit to the remaining power spectral density points and the notched power spectral coefficients are interpolated with the fitted model.

Figure 4.2 illustrates the clutter filtering process for a clutter-to-signal ratio (CSR) of 20 dB (CSR is a measure of the clutter suppression ability) with a clutter spectral width  $\sigma_c = 0.3$  m/s. A Gaussian clutter model is obtained from the received signal, and this model is used to notch the clutter spectral coefficients. The notched region

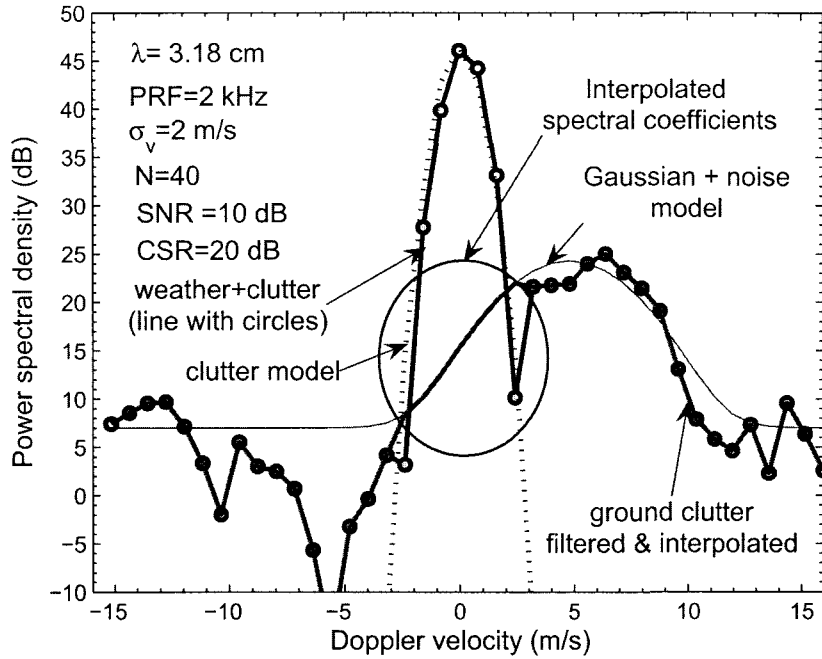


Figure 4.2: Clutter filtering with Gaussian spectral density fits

is recursively interpolated with a Gaussian spectral density fitted to the remaining signal to obtain the filtered signal. The ability to suppress clutter and estimate the Doppler moments and polarimetric variables are dependent on various factors such as system phase noise and desired accuracy. The impact of phase noise and number of pulses is studied by simulating weather and clutter signal with varying properties. The polarimetric signals are simulated based on procedure described by Chandrasekar et al. (1986). In this chapter the measure of clutter contamination used is the clutter-to-signal ratio (CSR).

The spectral method to reject clutter is possible in coherent pulsed Doppler radar. However, coherent radars often have phase errors from pulse-to-pulse due to phase stability of the oscillator and transmitter. This random phase noise modulates the received signal with a random phase code which results in distribution of power from the coherent received signal into white noise. The amount of signal converted to noise

is dependent on the phase noise of the system. The ability of the system to reject clutter is related the effective signal-to-noise ratio that can be achieved. The effective signal-to-noise ratio that can be achieved is given by (Passarelli and Zrnic, 1989)

$$SNR_e = \frac{e^{-\delta\theta^2}}{1 - e^{-\delta\theta^2}}, \quad (4.3)$$

where  $\delta\theta$  is the phase noise of the system in radians. For example,  $\delta\theta = 0.25^\circ$  results in  $SNR_e = 47.20 \text{ dB}$ . The impact of phase noise on clutter suppression ability is

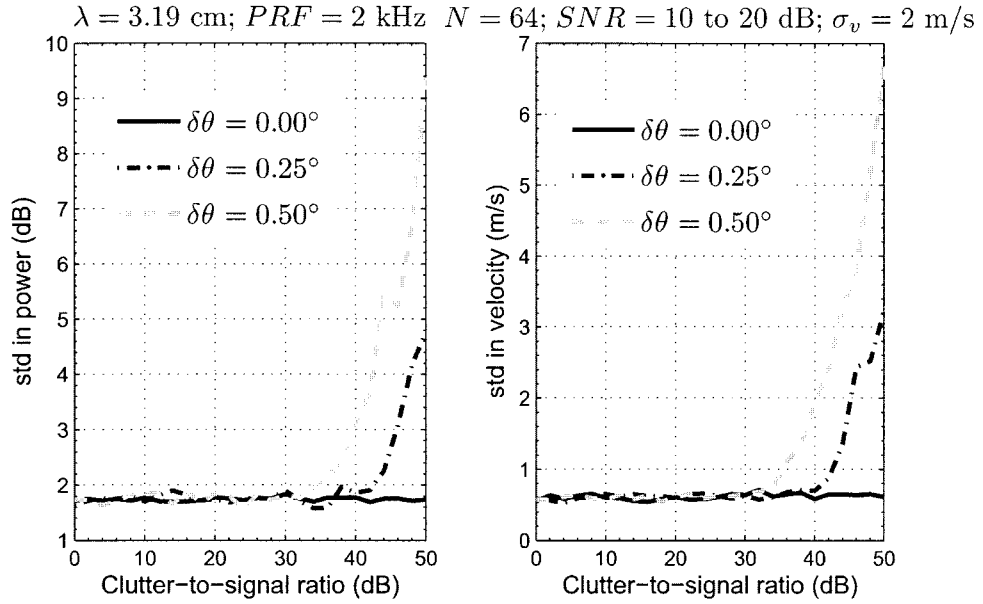


Figure 4.3: Standard deviation of power and mean Doppler velocity as a function of clutter-to-signal ratio for a weather signal with  $N = 64$  samples,  $\sigma_v = 2 \text{ m/s}$ , and  $SNR = 10 - 20 \text{ dB}$ . The weather echo is located at half the Nyquist velocity at  $PRF=2 \text{ kHz}$ .

evaluated by varying CSR and estimating the errors in the Doppler moments and polarimetric variables. In order to eliminate the effect of low SNR simulations are performed for SNR varying from 10 to 20 dB. The errors are averaged for SNR varying from 10 to 20 dB. The standard deviation is estimated for varying CSR with phase noise as a parameters. The mean Doppler velocity is selected to be half the Nyquist velocity so that clutter suppression ability is only affected by phase noise.

The standard deviations of power and mean Doppler velocity as a function of CSR are shown in Fig.4.3 for  $N = 64$  and  $\sigma_v = 2 \text{ m/s}$  at a nominal  $PRF = 2 \text{ kHz}$  operating at X-band. It can be observed that a system without any phase noise is capable of suppressing clutter up to 50 dB with acceptable accuracy while the clutter suppression degrades as phase noise increases from  $0.25^\circ$  to  $0.50^\circ$ .  $CSR = 43 \text{ dB}$  can be achieved for a system with  $0.25^\circ$  where the standard deviation of power is less than 2 dB and standard deviation of mean Doppler velocity is less than 2 m/s. However, the clutter suppression ability is lower when the accuracy of polarimetric variables are considered. The standard deviation of  $Z_{dr}$  and  $\phi_{dp}$  are shown as a function of CSR with phase noise as a parameter in Fig. 4.4. Clutter suppression up to 50 dB can be achieved in the absence of phase noise but only  $CSR = 35 \text{ dB}$  can be achieved for a system with  $0.25^\circ$  where the standard deviation of  $Z_{dr}$  is less than 0.6 dB and standard deviation of  $\phi_{dp}$  is less than  $5^\circ$ . It can be observed in Fig.4.3 and Fig. 4.4 that the clutter suppression ability drops to about 35 dB for Doppler moments and about 30 dB for polarimetric variables when the phase noise is increased to  $\delta\theta = 0.5^\circ$ . The system phase noise plays an important role in clutter suppression ability and forms one of the key design parameters for pulsed Doppler weather radars.

The number of pulses used to estimated the Doppler spectrum and filter out clutter has a direct impact on accuracy of the Doppler moments and polarimetric variables. The accuracy of Doppler moments and polarimetric variables as a function of number of samples can be obtained by assuming a Gaussian spectral model and covariance processing (Bringi and Chandrasekar, 2001). However, the accuracy of Doppler moments and polarimetric variables estimated after spectral clutter suppression is obtained based on simulations. The accuracy of Doppler moments and polarimetric variables is computed for  $PRF = 1.6 \text{ kHz}$  and  $PRF = 2.4 \text{ kHz}$ . The clutter-to-signal ratio is set to 25 dB and simulations are performed for varying number of pulses and with phase noise  $\delta\theta = 0.25^\circ$ . The standard deviations of power and mean Doppler velocity are shown in Fig. 4.5. The standard deviation of power

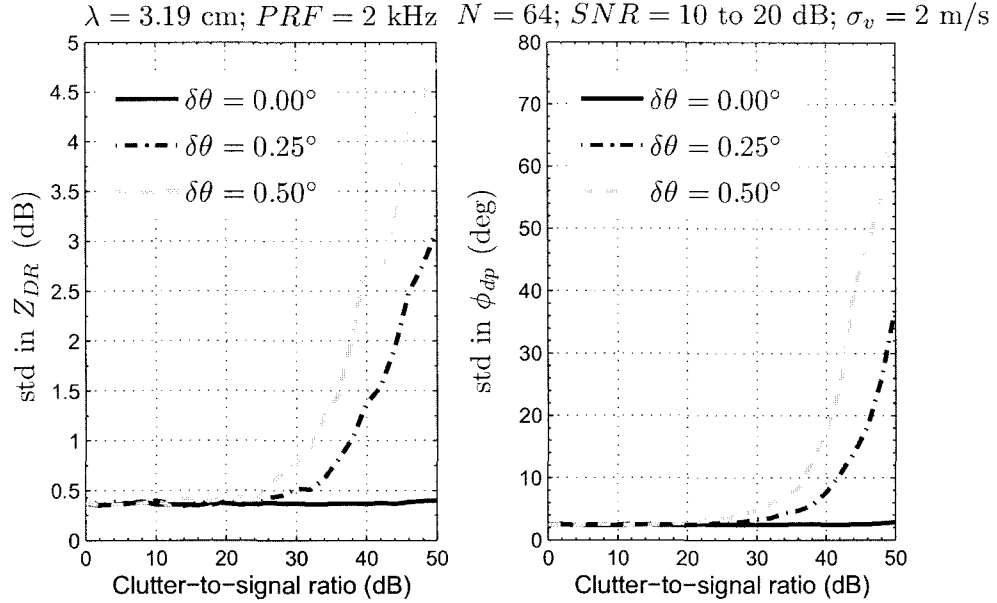


Figure 4.4: Standard deviation of  $Z_{dr}$  and  $\phi_{dp}$  as a function of clutter-to-signal ratio for a weather signal with  $N = 64$  samples,  $\sigma_v = 2 \text{ m/s}$ , and  $SNR = 10 - 20 \text{ dB}$ . The weather echo is located at half the Nyquist velocity at  $PRF=2 \text{ kHz}$ .

is generally less than 2 dB while the standard deviation of velocity is within 2 m/s when  $N = 40$  or more pulses are used. The standard deviations of  $Z_{dr}$  and  $\phi_{dp}$  are shown in Fig. 4.6. The standard deviation of  $Z_{dr}$  is less than 0.6 dB and standard deviation of  $\phi_{dp}$  is less than  $5^\circ$  when 40 or more samples are used.

#### 4.5 Dual-PRF waveform

Staggered PRT and staggered-PRF techniques for extending the unambiguous velocity have been known for more than two decades and are available on several operational Doppler weather radars, especially longer wavelength radar systems. The long standing problem with staggered PRT waveforms have been effective clutter filtering. Sachidananda and Znic (2000, 2002) proposed a spectral method for ground clutter filtering for staggered PRT and this technique was demonstrated for WSR-88D using the KOUN radar (Torres et al., 2004). However, this technique is not suitable at X-band because the reduction in wavelength from S-band to X-band dra-

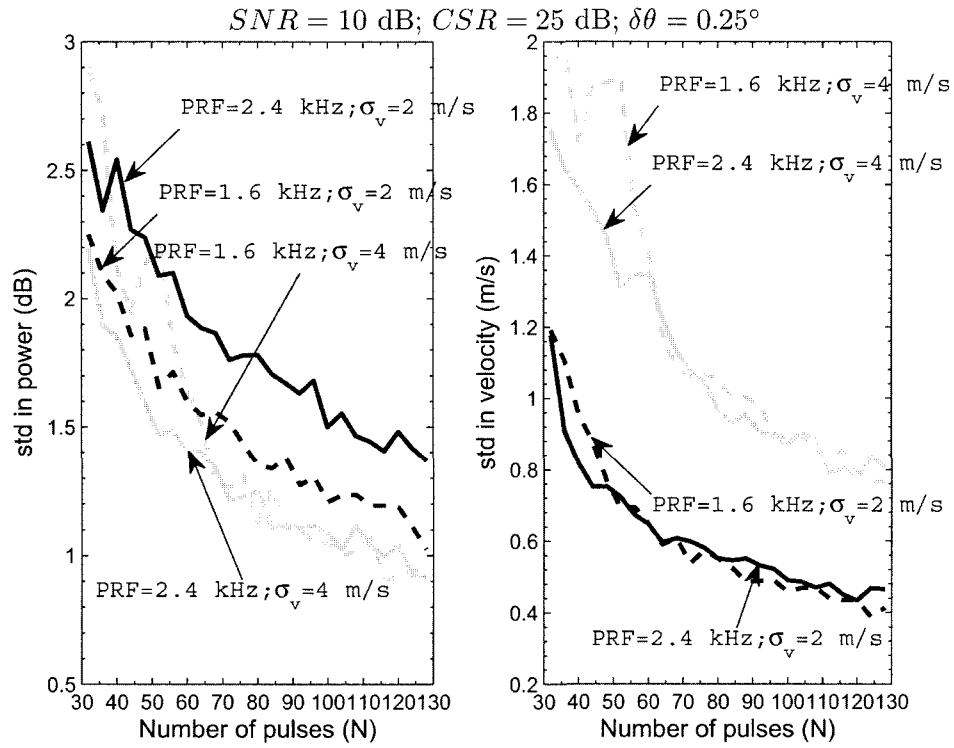


Figure 4.5: Standard deviation of reflectivity and mean Doppler velocity after ground clutter filtering as a function of number of pulses for  $\sigma_v = 2 \text{ m/s}$  and  $\sigma_v = 4 \text{ m/s}$ . The standard deviation is plotted for  $PRF = 1.6 \text{ kHz}$  and  $PRF = 2.4 \text{ kHz}$  for an  $SNR = 10 \text{ dB}$ ,  $CSR = 25 \text{ dB}$  and  $0.25^\circ$  phase noise.

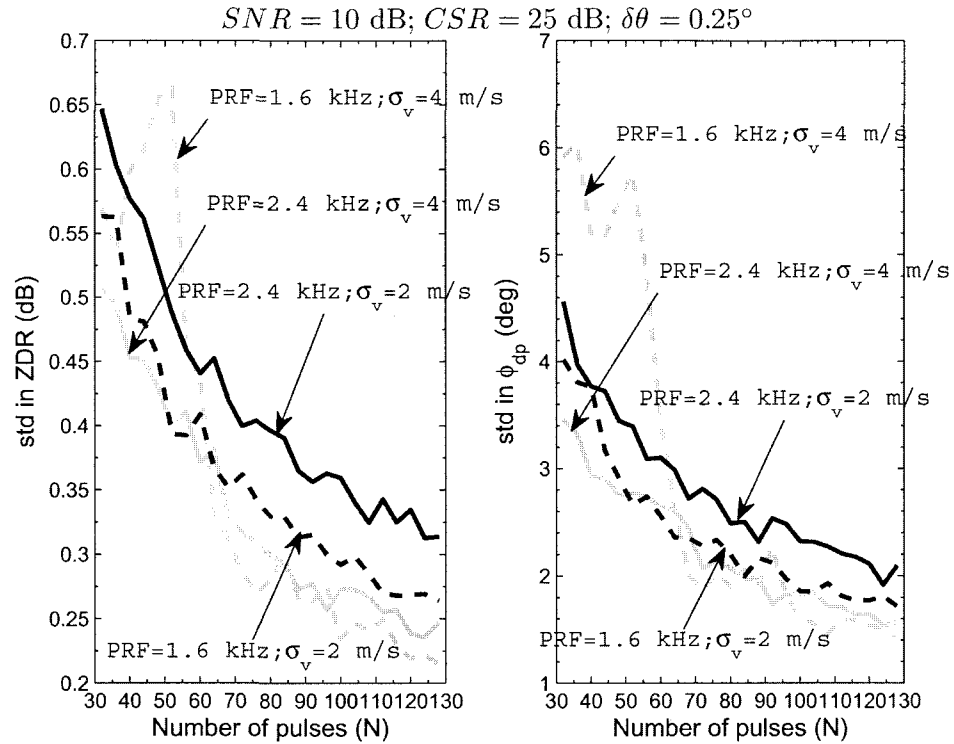


Figure 4.6: Standard deviation of  $Z_{dr}$  and  $\phi_{dp}$  after ground clutter filtering as a function of number of pulses for  $\sigma_v = 2 \text{ m/s}$  and  $\sigma_v = 4 \text{ m/s}$ . The standard deviation is plotted for  $PRF = 1.6 \text{ kHz}$  and  $PRF = 2.4 \text{ kHz}$  for an  $SNR = 10 \text{ dB}$ ,  $CSR = 25 \text{ dB}$  and  $0.25^\circ$  phase noise.

matically reduces the operating Doppler spectrum range (Nyquist bandwidth) of the staggered PRT waveform. Moisseev et al. (2008) suggested a time-domain parametric method for effective clutter filtering for staggered PRT and this method is suitable for implementation at X-band. However, the time-domain parametric method is computationally intensive and is currently not a viable option for real-time operations. A staggered PRF provides an alternative approach to mitigate the range-velocity ambiguity while still enabling effective clutter filtering.

Staggered PRF consists of a large block and typically the block size is the same as the integration cycle or the dwell time. For example, a dual-PRF waveform with  $\kappa = 2 : 3$  can be represented by

$$p_h = p_v = \left[ \underbrace{1, 0, 1, 0, 1, 0, \dots, 1, 0}_{PRF_1}, \underbrace{1, 0, 0, 1, 0, 0, 1, 0, 0, \dots, 1, 0, 0}_{PRF_2} \right], \quad (4.4)$$

where  $p_h$  and  $p_v$  are indicator function representation of the transmitted waveform as described by Bringi and Chandrasekar (2001). The subscripts ‘h’ and ‘v’ represent the transmit polarization state. The ‘1’s indicate the time instant when a pulse is transmitted and ‘0’s indicate that no pulse is fired. Any arbitrary waveform can be represented using this generalized representation. Consider a waveform with  $\kappa = 2 : 3$  with two different pulse spacings  $T_1 = 2T_u$  and  $T_2 = 3T_u$  where  $T_u$  is a fundamental pulse repetition time. The auto-correlation estimates,  $\hat{R}_1$  at lag  $T_1$  and  $\hat{R}_2$  at lag  $T_2$  are obtained from pulse-pair estimates. The mean velocity estimate and the maximum unambiguous velocity are estimated as

$$\hat{v} = \frac{\lambda}{4\pi T_u} \arctan \left( \hat{R}_1 \hat{R}_2^* \right) \quad (4.5)$$

$$v_a = \frac{\lambda}{4\pi T_u} \quad (4.6)$$

Smaller the  $T_u$ , larger the unambiguous velocity. However the maximum unambiguous velocity is limited by the accuracy of the estimator in (4.5) because the errors

Table 4.2: Dual-PRF unfolding for a stagger ratio of 2/3.

$v_1 - v_2$ in the vicinity of	$v_1$ correction term	$v_2$ correction term
$-2v_{a2} + 2v_{a1}$	$-2v_{a1}$	$-2v_{a2}$
$-2v_{a2}$	0	$-2v_{a2}$
0	0	0
$+2v_{a2}$	0	$+2v_{a2}$
$+2v_{a2} - 2v_{a1}$	$+2v_{a1}$	$+2v_{a2}$

in  $\hat{v}$  are inversely proportional to  $T_u$ . The best accuracy in the estimate of mean Doppler velocity is obtained for a stagger ratio  $\kappa = 2 : 3$  (Zrnic and Mahapatra, 1985). However, the accuracy of velocity estimated from (4.5) is much higher than the accuracy of velocity estimated from  $\hat{R}_1$  and  $\hat{R}_2$ . The Doppler velocities from the two auto-covariance estimates are obtained as below.

$$v_1 = \frac{\lambda}{4\pi T_1} \arctan(R_1) \quad (4.7)$$

$$v_2 = \frac{\lambda}{4\pi T_2} \arctan(R_2) \quad (4.8)$$

The velocity folding of  $v_1$  and  $v_2$  occur at different Doppler velocities. Therefore, a comparison of the two velocities can be used to obtain unfolded velocities. The  $v_1 - v_2$  velocity difference remains unique within the interval  $\pm v_a$  for a stagger ratio  $\kappa = 2 : 3$  (Nathanson, 1969). The unfolded velocity is obtained as

$$\hat{v}_{1u(2u)} = \hat{v}_{1u(2u)} + \alpha, \quad (4.9)$$

where  $\alpha$  is the velocity correction term. The velocity correction term is obtained based on the  $v_1 - v_2$  velocity difference and is given in Table 4.2.

Figure 4.7 shows a scatter plot of unfolded velocity versus true velocity for  $\sigma_v = 4 \text{ m/s}$  with two different dual-PRF waveforms. Waveform-I uses  $PRF_1 = 2.4 \text{ kHz}$  with  $N_1 = 54$  and  $PRF_2 = 1.6 \text{ kHz}$  with  $N_2 = 40$ . Waveform-I provides an unambiguous velocity  $v_a = 38.3 \text{ m/s}$ . Waveform-II uses  $PRF_1 = 3.0 \text{ kHz}$  with  $N_1 = 64$  and  $PRF_2 = 2.0 \text{ kHz}$  with  $N_2 = 56$ . Waveform-II provides an unambiguous velocity  $v_a = 47.8 \text{ m/s}$ . Both waveform-I and waveform-II can provide an integration period

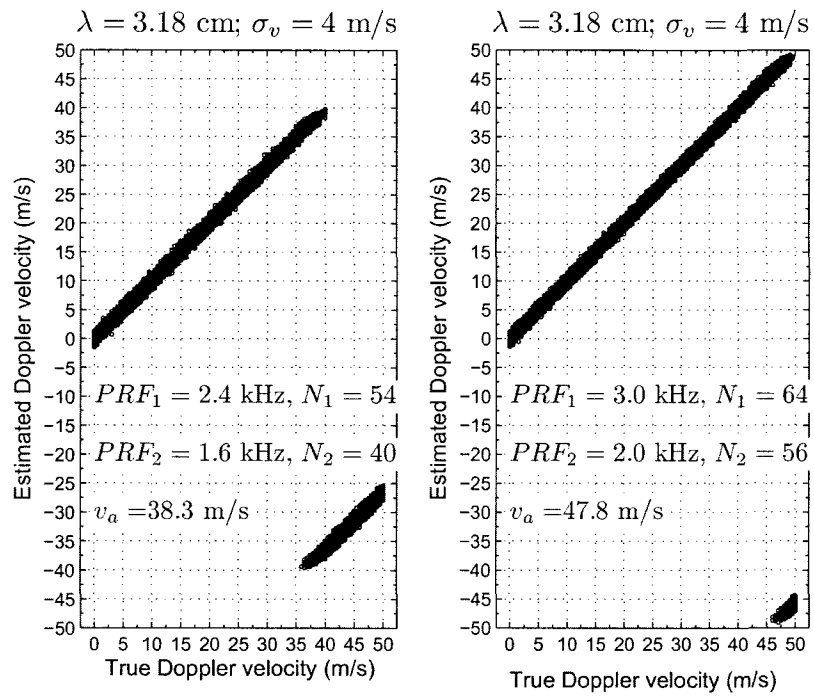


Figure 4.7: Scatter plot of unfolded Doppler velocity versus the true Doppler velocity for  $\sigma_v = 4 \text{ m/s}$  for two different dual-PRF waveform at X-band.

of  $1^\circ$  at a scan speed of 21 deg/s. It can be observed in Fig. 4.7 that the unfolding based on  $v_1 - v_2$  velocity difference provides satisfactory results. However, the presence of ground clutter and clutter filtering will result in higher errors in the unfolded velocities.

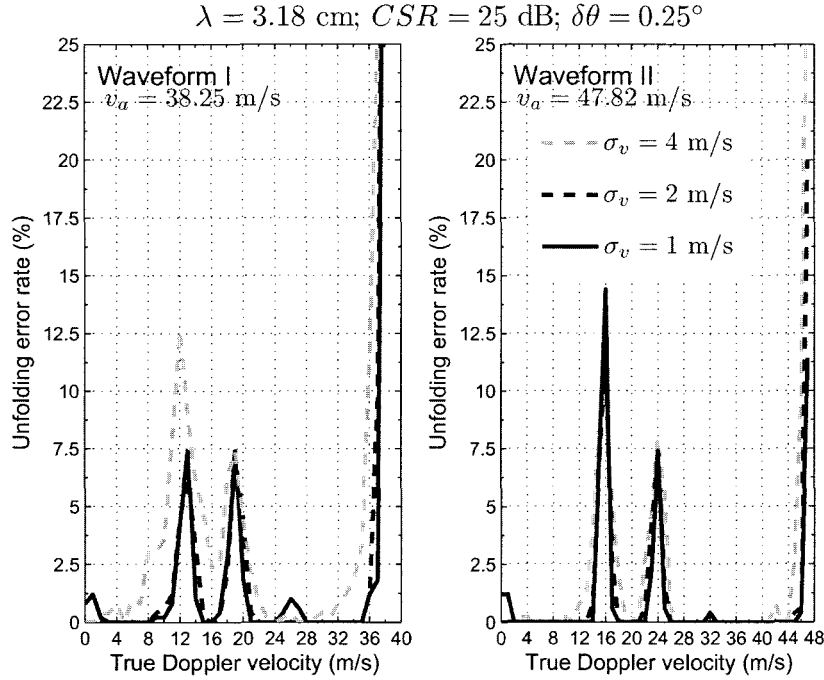


Figure 4.8: Unfolding error rate as a function of mean Doppler velocity for  $CSR = 25$  dB and phase noise  $\delta\theta = 0.25^\circ$ . Waveform-I:  $PRF_1 = 2.4$  kHz,  $N_1 = 54$ ,  $PRF_2 = 1.6$  kHz,  $N_2 = 40$  and  $v_a = 38.3$  m/s. Waveform-II:  $PRF_1 = 3.0$  kHz,  $N_1 = 64$ ,  $PRF_2 = 2.0$  kHz,  $N_2 = 56$  and  $v_a = 47.8$  m/s.

The unfolding error rate for waveform-I and waveform-II after ground clutter filtering with  $CSR = 25$  dB is shown in Fig. 4.8 as a function of mean Doppler velocity. The unfolding error rate in Fig. 4.8 is shown for Doppler spectral width of  $\sigma_v = 1, 2, 3$  m/s and it can be observed that the unfolding errors are high at the Nyquist folding velocities of  $PRF_1 = 2.4$  kHz and  $PRF_2 = 1.6$  kHz in Waveform-I, and at Nyquist folding velocities of  $PRF_1 = 3.0$  kHz and  $PRF_2 = 2.0$  kHz, in Waveform-II. The velocity unfolding errors are larger than 5% at the Nyquist folding

velocities. The presence of measurement errors in the estimated velocities at each PRF may results in  $v_1 - v_2$  velocity difference that produce outliers in the unfolded velocity field. Such outliers have been reported in Holleman and Beekhuis (2003); Joe and May (2003) and spatial filtering has been suggested to remove the outliers. In this section a phasor median filter (PMF) is utilized to remove outliers in the velocity field. The PMF is based on multi-channel median filtering proposed by Astola et al. (1990) for non-linear filtering of images. A phasor field is obtained from the unfolded velocity estimates as

$$\mathcal{V} = \exp\left(j\frac{\hat{v}\pi}{v_a}\right), \quad (4.10)$$

where  $\hat{v}$  is the measured velocity and  $\mathcal{V}$  is the phasor representation of the velocity. Let  $W = \{\mathcal{V}_i; i = 1, 2, 3, \dots, n^2\}$  be the phasors within an  $n \times n$  processing window in the range-azimuth dimension. The absolute distance associated with the sample  $\mathcal{V}_i$  is given by

$$D_i = \sum_{j=1}^{n^2} |\mathcal{V}_i - \mathcal{V}_j|, \quad \forall i = 1, 2, 3, \dots, n^2, \quad (4.11)$$

where  $D_i$  is the aggregated vector distances. The output of the PMF is given by

$$\mathcal{V}_{PMF} = \min_{\mathcal{V}_i} D_i, \quad (4.12)$$

which is the measurement sample that minimizes the distance to other samples within the processing window. To evaluate the performance of PMF a two dimensional wind field is simulated (Wood and Brown, 1992) and the observed velocity with waveform-I and waveform-II is obtained. A Gaussian distributed noise with standard deviation  $\sigma(v)$  that corresponds to measurement error in Doppler velocity is added to the radial velocities at each PRF. The unfolding of velocities is performed on the observation with noise added to it. The velocity unfolding error is computed by comparing the unfolded velocities with the true velocities. The velocity unfolding error obtained from raw unfolded velocities, velocity filtered with PMF of order  $n$  and velocity filtered

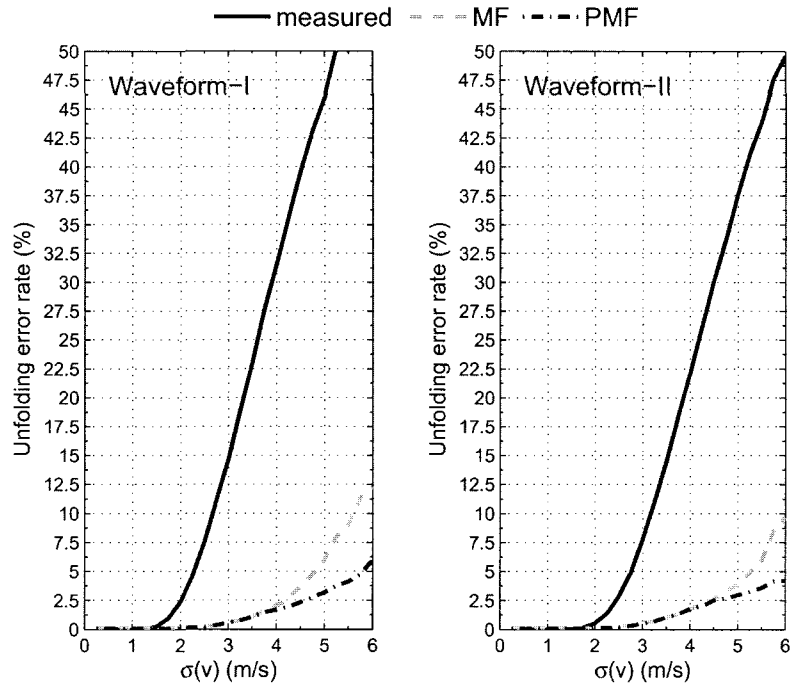


Figure 4.9: Unfolding error rate as a function of variance of mean Doppler velocity for raw unfolded velocity, phasor median filter, and median filter data. Waveform-I:  $PRF_1 = 2.4 \text{ kHz}, N_1 = 54, PRF_2 = 1.6 \text{ kHz}, N_2 = 40$  and  $v_a = 38.3 \text{ m/s}$ . Waveform-II:  $PRF_1 = 3.0 \text{ kHz}, N_1 = 64, PRF_2 = 2.0 \text{ kHz}, N_2 = 56$  and  $v_a = 47.8 \text{ m/s}$ .

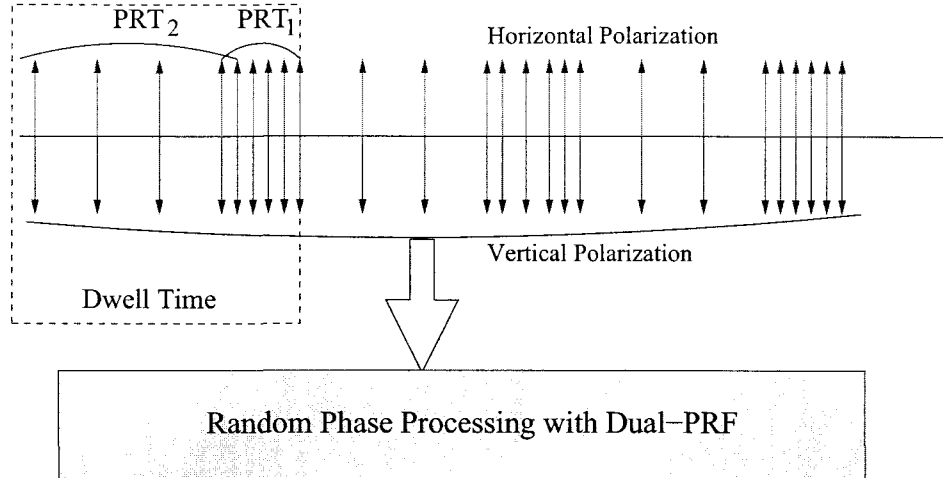


Figure 4.10: Illustration of dual-PRF waveform implemented in CASA IP1 radars.

with a simple median filter (MF) of order  $n$  is shown in Fig. 4.9. The unfolding error in Fig. 4.9 is plotted as a function of  $\sigma(v)$  and it can be observed that the raw unfolded estimates can have very high errors for  $\sigma(v) \geq 2.5 \text{ m/s}$  while the errors are small ( $\leq 5\%$ ) when spatial filters are used. The performance of PMF and MF are comparable in the region where  $\sigma(v) \leq 4 \text{ m/s}$ . However, the performance of PMF is better than MF when there are large errors in the Doppler velocity field.

#### 4.6 Waveform for first generation CASA radars

Based on the requirements for the first generation CASA radar network a dual-PRF waveform has been recommended for operations. The waveform consists of two PRFs with  $N_1 = 40$  pulses at  $PRF_1 = 1.6 \text{ kHz}$  and  $N_2 = 54$  pulses at  $PRF_2 = 2.4 \text{ kHz}$ . This dual-PRF waveform as shown in Fig.4.10 has been operational on the IP1 radar network. The waveform is processed with full spectral processing to enable spectral clutter filtering and overlay echo suppression. The dual-PRF measurements are used to unfold the velocity and the naturally occurring random phase coding with magnetron radars is used for range overlay suppression.

### 4.6.1 Real-time environment and data

The data acquisition system is a FPGA system with Ethernet based data interfaces to the real-time signal processor. The real-time signal processing is performed on a general purpose server running a Linux operating system. The servers currently used in CASA's first generation radars use a single Intel Quad core Xeon processor with a clock speed of 2.33 GHz and 3 GB of RAM. The calibration and timing information are inputs to the signal processor to process staggered waveforms and provide calibrated products. A more detailed description of the hardware, data acquisition system, and operations is presented in Junyent et al. (2009).

The signal processor has been constantly operated without failure for several years. Extensive data sets have been archived during operations. Figure 4.11 and Fig. 4.12 illustrate the Doppler moments and polarimetric variables estimated in the KSAO radar obtained with spectral processing and dual-PRF waveform using  $PRF_1 = 2.4 \text{ kHz}$ ,  $N_1 = 54$ ,  $PRF_2 = 1.6 \text{ kHz}$ , and  $N_2 = 40$ . A Range Height Indicator (RHI) scan performed at an azimuth of  $0^\circ$  from  $0 - 30^\circ$  during a widespread shower event on May 04, 2009 at 19:34:18 UTC is shown in Fig. 4.11 and Fig. 4.12. Figure 4.11(a), (b) shows the filtered reflectivity and Doppler velocity along with the unfiltered products. The suppression of ground clutter closer to the ground can easily be observed. However, there is residual clutter in regions where the ground clutter signal is very strong. The filtered  $Z_{dr}$  and  $|\rho_{hv}(0)|$  along with the unfiltered data are shown in Fig.4.12(a), (b). There is a slight increase in  $|\rho_{hv}(0)|$  that occurs after filtering because noise spectral coefficients are notched which results in slightly improving the co-polar correlation coefficient. A scatter plot of  $Z_h$  versus  $Z_{dr}$  from RHI data collected with KSAO radar at different azimuths during a wide spread showers on May 04, 2009 from 19:24 to 19:34 UTC is shown in Fig. 4.13. The scatter plot is shown for both unfiltered data and filtered data. The data points selected in the scatter plots are based on a reflectivity threshold  $Z_h \geq 10 \text{ dBZ}$  and co-polar correlation coefficient

$|\rho_{hv}(0)| \geq 0.99$ . The impact of clutter and filtering can be observed in Fig. 4.13 where the strong clutter signals provides very noise  $Z_{dr}$  data for reflectivities greater than 30 dBZ. The outliers in the filtered data can be attributed to the residual clutter.

#### 4.6.2 Clutter suppression in IP1

Ground clutter suppression is one of the critical aspects for IP1 radars because the antenna beam width is  $2^\circ$  which results severe clutter contamination at lower elevation angles. The ground clutter signals can be side-lobe clutter and main lobe clutter. Traditionally, clutter maps are used to identify the clutter region and clutter filter is applied only as indicated by clutter maps. However, no clutter map is used in IP1 radar and the filter is applied in all regions. Figure 4.14 shows the observations with and without clutter filtering. The phenomenon shown in Fig.4.14(a) is a hook echo observed from the Lawton radar on May 09, 2007 at 00:37:42 UTC. Hook echoes are associated with tornadoes in a storms. It can be observed that the spectral clutter filtering suppresses the strong ground clutter closer to the hook echo. The circulation feature is more clear after spectral filtering as shown in Fig.4.14(b).

Ground clutter suppression has been traditionally viewed in terms of its impact on the spectral moments. However, in a networked radar environment the estimated moments are used to adaptively steer the antenna. The adaptive steering of the antenna will not have the optimal volume coverage pattern if there are a lot false detection due to clutter. Therefore, in addition to providing filtered spectral moments, the spectral clutter filter also minimizes the false detection for adaptive scanning which is very critical for a networked radar operations.

To evaluate clutter suppression in the IP1 radar network the clutter suppressed is decomposed into two types. That is to say the amount of clutter suppressed when there is no meteorological signal and the amount of clutter suppressed when there is weather echo present along with clutter. In order to achieve this goal an estimate of the SNR is used to classify the CSR measurements. The SNR and CSR were estimated

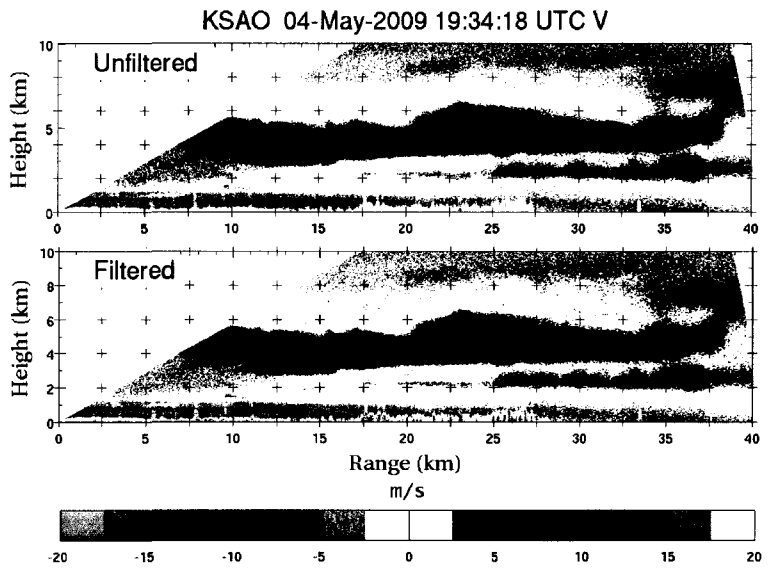
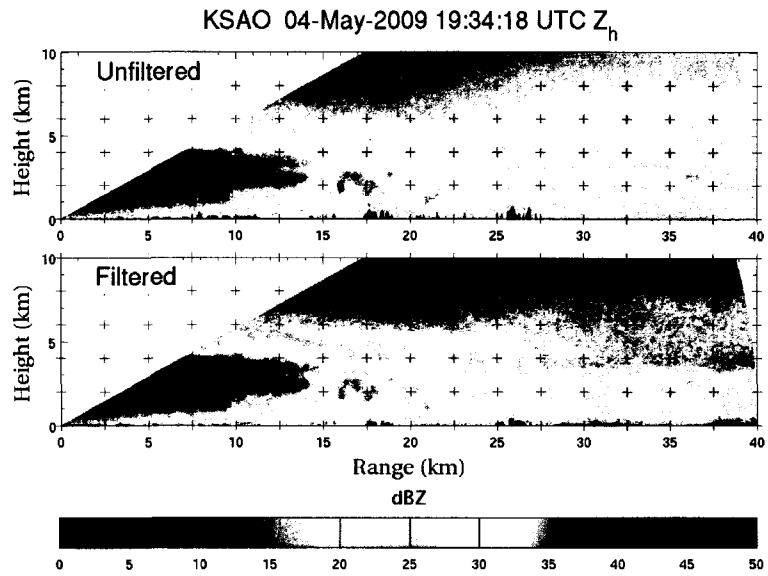


Figure 4.11: RHI plots of dual-PRF data collected with Chickasha radar on May 04, 2009 at 19:34:18 UTC:(a) The unfiltered and filtered reflectivity;(b) The unfiltered and filtered mean Doppler velocity.

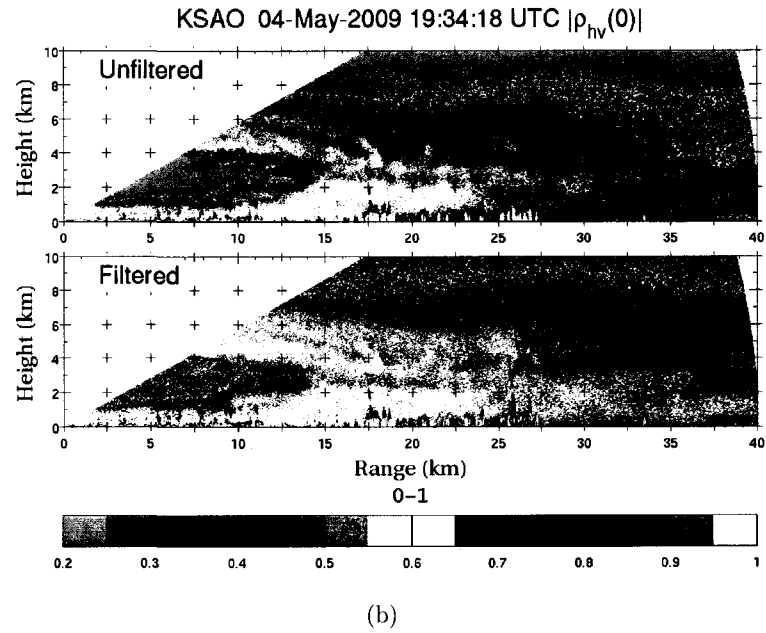
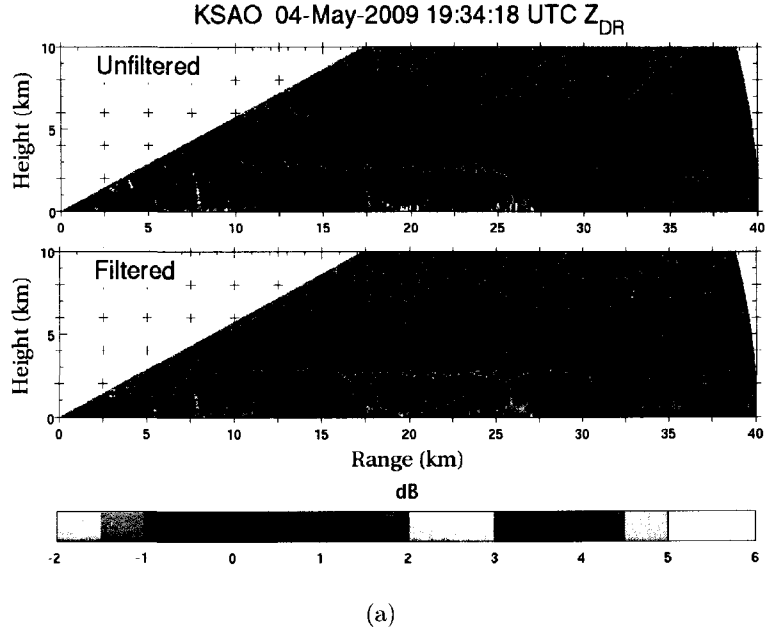


Figure 4.12: RHI plots of dual-PRF data collected with Chickasha radar on May 04, 2009 at 19:34:18 UTC:(a) The unfiltered and filtered  $Z_{dr}$ ;(b) The unfiltered and filtered  $|\rho_{hv}(0)|$ .

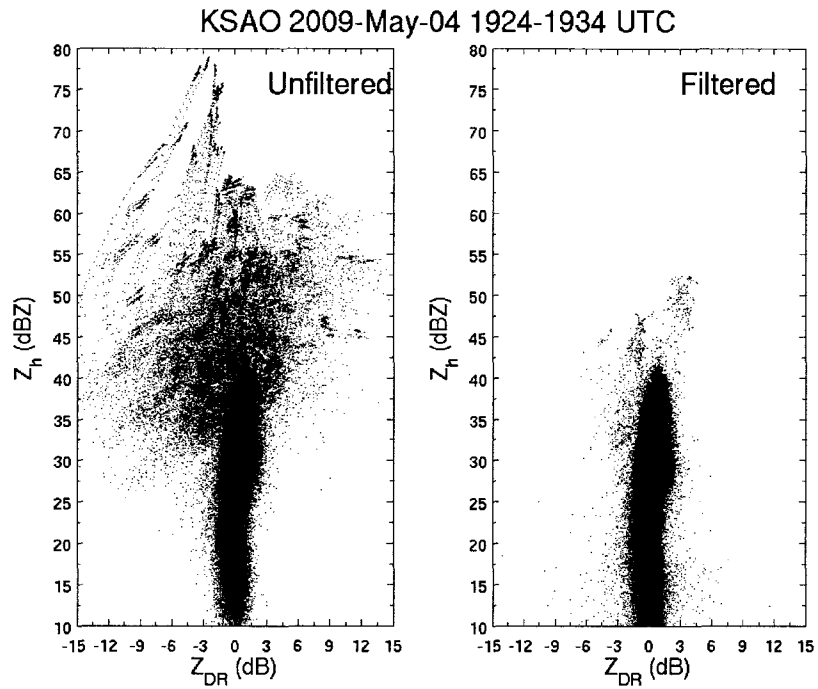
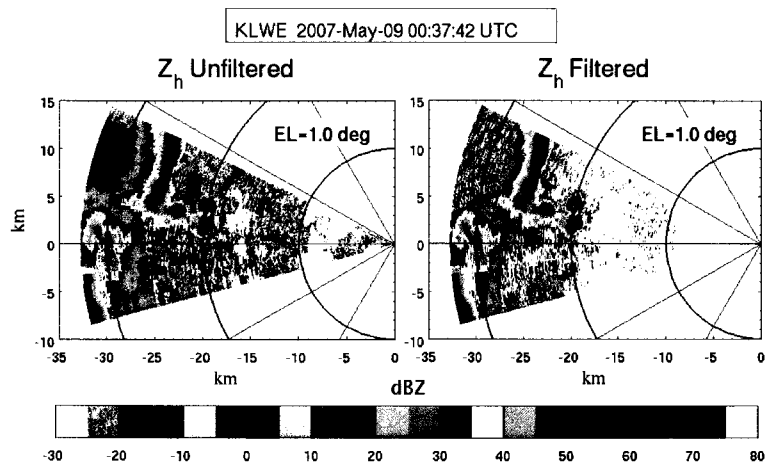
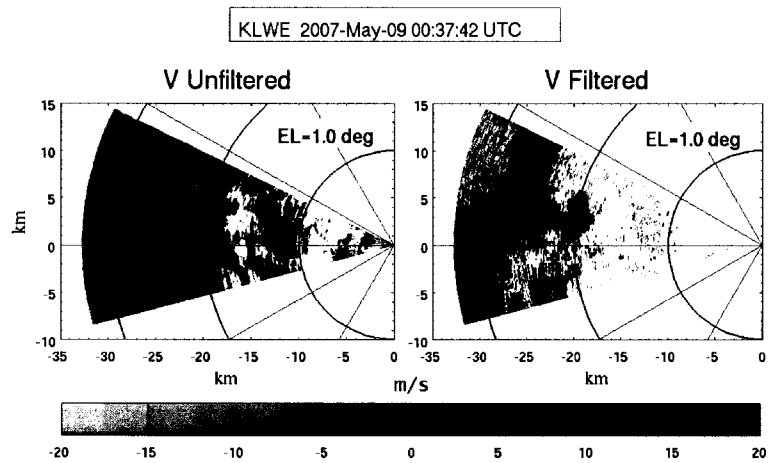


Figure 4.13: Scatter plot of  $Z_h$  versus  $Z_{dr}$  from RHI data collected with KSAO radar at different azimuths during a wide spread showers on May 04, 2009 from 19:24 to 19:34 UTC. The scatter plot is done for data with unfiltered and filtered data.



(a)



(b)

Figure 4.14: PPI plots of dual-PRF data collected with Cyril radar on May 09, 2007 at 00:37:42 UTC:(a) The unfiltered and filtered reflectivity;(b) The unfiltered and filtered velocity.

Table 4.3: Ground clutter suppression

Date	Radars	CSR with no weather (dB)	CSR with weather (dB)
May 06, 2007	KCYR, KLWE	27.50	19.25
May 07, 2007	KCYR, KLWE	26.25	15.25
May 09, 2007	KCYR, KLWE	26.00	17.50
Jun 14, 2007	KCYR, KSAO, KRSP, KLWE	31.25	21.00
Jun 20, 2007	KCYR, KSAO, KRSP, KLWE	30.50	19.50
Mar 31, 2008	KSAO	33.50	21.00
Apr 09, 2008	KSAO	33.00	21.25
May 02, 2008	KCYR, KSAO	29.50	19.50
May 07, 2008	KCYR, KSAO, KRSP, KLWE	30.25	19.00
Jun 17, 2008	KCYR, KRSP	30.00	24.25

in the spectral domain. Figure 4.15 shows the cumulative distribution function (CDF) of CSR. The CDF of CSR when meteorological signal is present is shown in Fig.4.15(a) and CSR when no meteorological signal is present is shown in Fig.4.15(b). A SNR threshold greater than 3 dB was used to identify meteorological signal. The CDFs shown are for ten data sets collected with the IP1 radar nodes during experiments conducted in 2007 and 2008. Table 4.3 lists the clutter suppressed for the specified date. The clutter suppression is obtained as the 99% value of CSR from the CDF for each date. The data set corresponding to each date can be from more than one radar as shown in second column of Table 4.3. The clutter suppressed when the received signal is purely clutter is much higher than when weather echo is contaminated by clutter. The total SNR of the signal is limited by the phase noise of the system. which implies that the signal plus clutter power is limited by the phase noise. Therefore, the clutter suppression observed with the system is about 33 dB based on the observation from IP1 CSR data.

#### 4.6.3 Overlay echo suppression in IP1

Among the various possibilities, phase coding of transmitted waveform has been deployed with some degree of success, with weather radars. In the phase coding

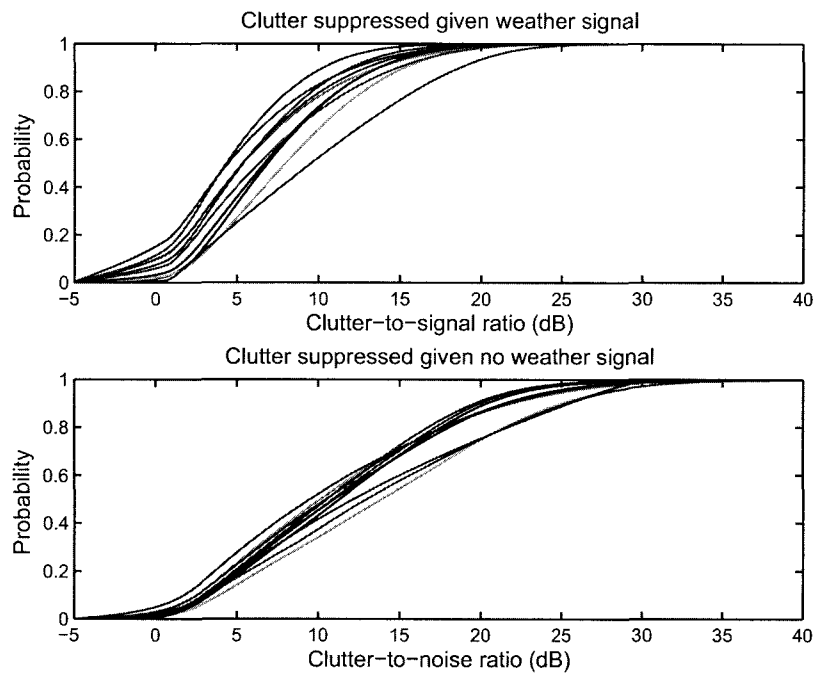


Figure 4.15: Cumulative distribution function of clutter suppressed (a) with weather signal (b) without weather echo. The cumulative distribution functions plotted is for ten data sets collected with the IP1 radar network.

scheme the transmitted pulses are tagged with a phase code or *switching phase* ( $\psi_k$ ). The received signal is phase corrected (cohered) to account for the switching phase. Only the selected trip, say the first trip signal is cohered, the second-trip is then phase modulated by the phase sequence  $\phi_k = \psi_{k-1} - \psi_k$ . Let  $V_1(k)$  and  $V_2(k)$  be the two distinct weather echoes from the first and second-trip respectively. The received signal after re-cohering for the first trip echo can be written as

$$\begin{aligned} V(k) &= (V_1(k)e^{j\psi_k} + V_2(k)e^{j\psi_{k-1}})e^{-j\psi_k} \\ &= V_1(k) + V_2(k)e^{j(\psi_{k-1}-\psi_k)} \end{aligned} \quad (4.13)$$

where the sequence  $\phi_k = \psi_{k-1} - \psi_k$  is called the *modulation code*. The second-trip signal  $V_2(k)$  is phase modulated by the poly-phase sequence  $e^{j\phi_k}$ . In real operational scenarios there can be third and fourth trip signals and these signals are also phase modulated by  $\psi_{k-2} - \psi_k$  and  $\psi_{k-3} - \psi_k$  respectively but only second-trip signal will be considered in this section. The modulation code alters the spectral distribution of the overlaid second-trip signal,  $V_2(k)$ . The exact nature of this change in spectral distribution depends on the modulation code  $\phi_k$ .

Let  $\mathbf{v}_1$  and  $\mathbf{v}_2$  be the first and second trip signal vectors respectively. The cohered received signal can be written as

$$\mathbf{v} = \mathbf{v}_1 + \boldsymbol{\phi}\mathbf{v}_2 \quad (4.14)$$

where  $\boldsymbol{\phi} = \text{diag}[\exp(j\phi_k)]$  matrix. In frequency domain with DFT on both sides of (4.14).

$$\mathbf{V} = \mathbf{V}_1 + \boldsymbol{\Phi}\mathbf{V}_2 \quad (4.15)$$

Note that circular convolution of the DFTs can be represented as matrix multiplication. This convolution matrix,  $\boldsymbol{\Phi}$ , is a circulant matrix whose first row is the discrete Fourier transform of  $\phi_k$ . The spectral distribution of  $\boldsymbol{\Phi}$  determines the nature of  $\boldsymbol{\Phi}\mathbf{V}_2$ . For example, if  $\boldsymbol{\Phi}$  is uniformly distributed (i.e.,  $\phi_k$  is a random phase sequence) in the

Nyquist bandwidth then the second trip echo,  $\mathbf{v}_2$  is whitened and appears as noise. Random phase coding of transmitted pulses was proposed by Siggia (1983). Random phase coding occurs naturally with magnetron transmitters. Many of the weather radars deployed around of world use magnetron transmitter and random phase coding can be used to suppress range overlaid echoes. Alternatively,  $\Phi$  can selected such that the spectral distribution  $\Phi$  has only a finite number of non zero spectral coefficients resulting in weighted replicas of  $\mathbf{V}_2$  in the Nyquist bandwidth.  $\Phi$  with finite number of non zero spectral lines are obtained from systematic phase sequences or systematic phase codes. Systematic phase sequences have been proposed and evaluated for range ambiguity mitigation (Sachidananda and Zrnic, 1999; Bharadwaj and Chandrasekar, 2007).

The IP1 radar use magnetron transmitter which forces the use of random phase coding that naturally occurs with magnetron. Figure 4.16 shows the observations of reflectivity with and without overlaid echo suppression for a precipitating region with light rain. The phenomenon shown in Fig.4.16 is observed from the Cyril radar on Feb 09, 2007 at 00:37:42 UTC. The presence of overlaid echoes can lead to biases in precipitation estimation. The presence of overlaid echo is very clearly observed in Fig.4.16 without any spectral processing to remove second trip echoes while the filtered reflectivity has both ground clutter as well as overlaid echoes filtered. In addition to biasing precipitation estimates overlaid echoes lead to serous problem in adaptive scanning systems that rely on precipitation detection such as the MC&C in CASA's IP1 radar network. The presence of overlaid echoes will lead to precipitation detection where there is no echo. Therefore, it is very important to mitigate and filter the overlaid echoes to enable adaptive scanning. The use of random phase coding to suppress overlaid echoes has been operation in CASA's IP1 radars. Figure 4.17 shows the cumulative distribution function (CDF) of overlaid echo suppressed. The CDFs shown are for ten data sets collected with the IP1 radar nodes during experiments conducted in 2007 and 2008. Table 4.4 lists the overlaid echo suppressed for the

specified date. The amount of suppression is measured as the 99% value of overlaid echo suppression from the CDF for each date. The data set corresponding to each date can be from more than one radar as shown in second column of Table 4.4.

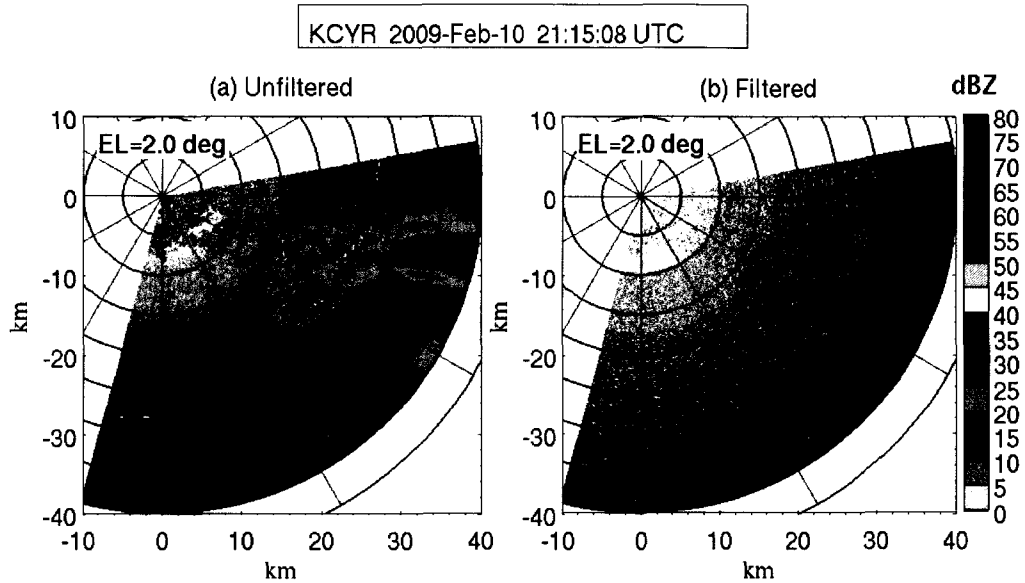


Figure 4.16: Reflectivity of a precipitation cell contaminated with ground clutter and overlaid echoes. (a) Unfiltered reflectivity (b) Filtered reflectivity. Data collected from Cyril on Feb 10, 2009 at 21:15:08 UTC with a dual-PRF waveform.

#### 4.6.4 Velocity dealiasing in IP1

The dual-PRF waveform has been used in the IP1 radar network to dealias radial velocities. Figure 4.18 shows the reflectivity observations from a hook echo observed from Cyril. The data set was collected on Feb 10, 2009 at 21:15:39 UTC at an elevation of 3.0 degrees. The radial velocity at the individual PRFs are shown in Fig. 4.19(a). The velocity aliasing effect is clearly observed as radial streaks. The estimated radial velocities are dealiased by comparing the difference of the adjacent radial velocity

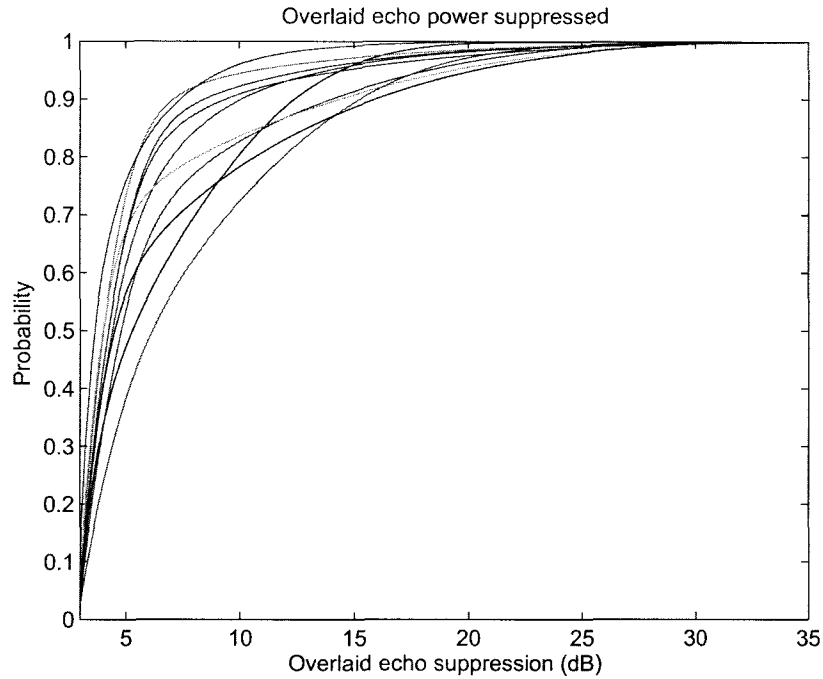


Figure 4.17: Cumulative distribution function of overlaid echo suppressed. The cumulative distribution functions plotted is for ten data sets collected with the IP1 radar network.

Table 4.4: Overlaid echo suppression

Date	Radars	Overlaid echo suppressed (dB)
May 06, 2007	KCYR, KLWE	18.00
May 07, 2007	KCYR, KLWE	22.75
May 09, 2007	KCYR, KLWE	23.75
Jun 14, 2007	KCYR, KSAO, KRSP, KLWE	22.25
Jun 20, 2007	KCYR, KSAO, KRSP, KLWE	25.00
Mar 31, 2008	KSAO	27.00
Apr 09, 2008	KSAO	23.50
May 02, 2008	KCYR, KSAO	27.50
May 07, 2008	KCYR, KSAO, KRSP, KLWE	25.25
Jun 17, 2008	KCYR, KRSP	14.25

from the same range gate. The measure velocities at the individual PRFs are less than  $13\text{ m/s}$  and  $20\text{ m/s}$  for the long and short PRT bursts. The dealiased velocities are shown in Fig. 4.19(b) and it can be observed that velocities greater than  $20\text{ m/s}$  are retrieved. This can be observed around the zero degree azimuth from 10 km to 15 km in range. However, dual-PRF dealiasing does have unfolding errors and this can be observed in Fig. 4.19(b). Such error have been reported in literature and can be corrected for by using spatial filtering as described in Section 4.5. Figure

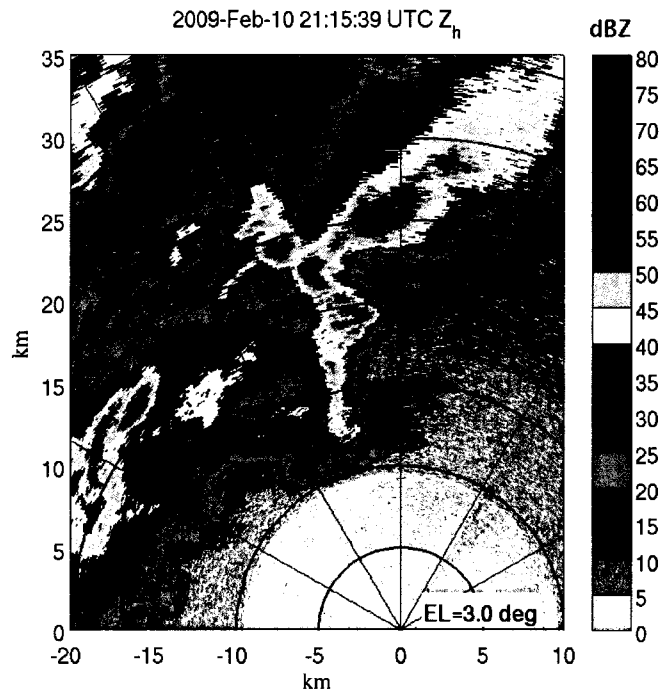


Figure 4.18: Reflectivity of a precipitation cell forming a hook echo. Data collected from Cyril on Feb 10, 2009 at 21:15:39 UTC with a dual-PRF waveform.

4.20 shows a comparison of the spatially filtered Doppler velocity field and the raw unfolded velocity obtained from the dual-PRF waveform. The data shown in Fig.4.20 is an example obtained from IP1 operations from Cyril radar on Mar 24, 2009 at 00:50:15 UTC. Figure 4.20(a) shows the attenuation corrected reflectivity obtained after spectral filtering. Figure 4.20(b) shows the raw unfolded velocity obtained and the speckle noise in the velocity field easily observed. This noise in the velocity field

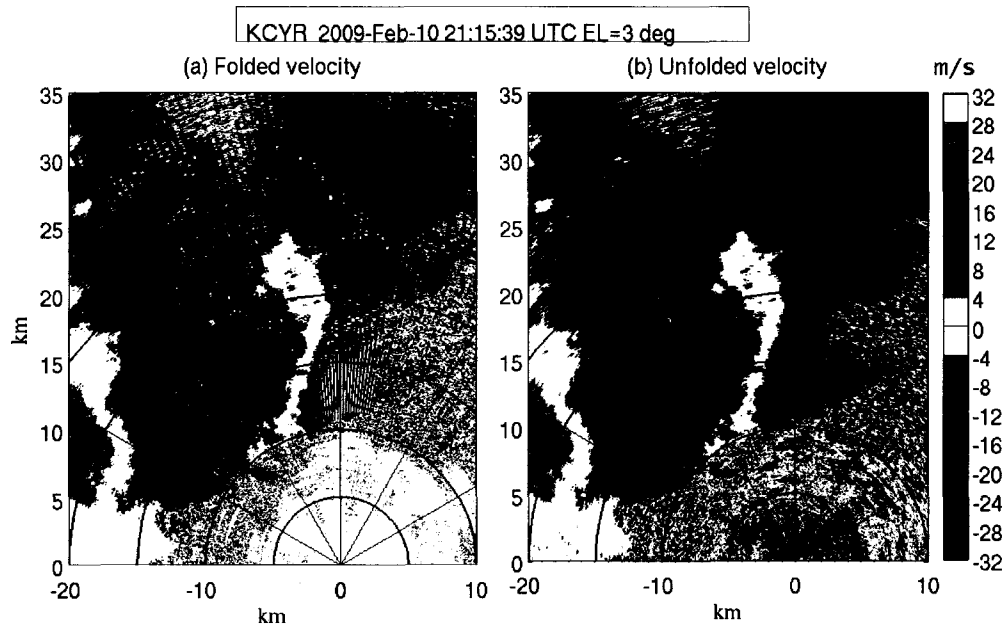


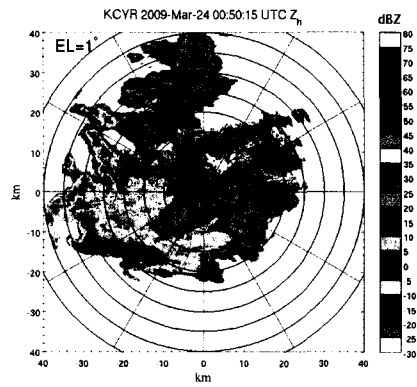
Figure 4.19: Doppler velocity of a precipitation cell forming a hook echo (a) Folded velocity (b) Unfolded velocity. Data collected from Cyril on Feb 10, 2009 at 21:15:39 UTC with a dual-PRF waveform.

occurs as a result of incorrect unfolding and this error in unfolding is because of increased variance after spectral filtering. Figure 4.20(c) shows the filtered velocity field after nonlinear filtering using PMF. There is a reduction in the speckle noise in the velocity field after the application of PMF. The order of PMF chosen in this case is  $n = 5$ . It is important to select  $n$  depending on the desired level of smoothing of the velocity field.

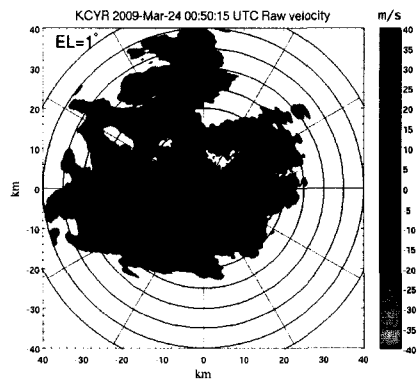
#### 4.7 Summary

This chapter described the design, implementation and demonstration of spectral processing for staggered waveforms with simulations as well as on CASA's IP1 radars operating at X-band. The challenges associated with designing waveforms for an X-band radar system were described and mainly included issues relating to range-velocity ambiguity and ground clutter suppression. In addition to range-velocity ambiguity and clutter filtering the waveforms design needs to take into considerations operational requirements and hardware limitations. The important factors affecting the waveform design for precipitation radars is the resulting dwell time based on scan speeds and the agility of the transmitter to implement complex waveforms.

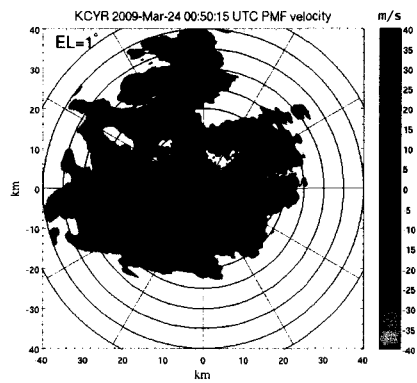
Spectral processing is used for ground clutter suppression. The proposed spectral filter uses an adaptive notch filter and recursive interpolation to minimize the impact of notch filtering. The recursive interpolation is beneficial for estimating the Doppler spectral moments. However, no interpolation is required for the complex spectral coefficient to estimate the polarimetric variables. It is critical that identical notch filters and noise filters be applied in both the horizontal polarization and vertical polarization channels. The clutter suppression ability based on the phase noise of the system and the number of pulses used. A phase noise of  $0.25^\circ$  will provide adequate clutter suppression. The number of pulses is determined by the accuracy requirement and the operational scan speeds. A design space with the number of pulses, Doppler



(a)



(b)



(c)

Figure 4.20: PPI plots of dual-PRF data collected with Cyril radar on Mar 24, 2009 at 00:50:15 UTC:(a) The filtered reflectivity;(b) Raw unfolded velocity and (c) PMF filtered velocity.

spectral moments and polarimetric variables has been presented in this chapter at X-band.

Dual-PRF waveform is suggested to mitigate the ambiguity in measurements. A simple unfolding algorithm for dealiasing the velocities is described and its performance in the presence errors due to ground clutter filtering was described. The outliers or high errors in velocity mostly lie in the vicinity of the Nyquist folding velocities of the waveform. The outliers due to incorrect unfolding can be minimized by applying spatial filters. A phasor median filter (PMF) was presented to reduce the unfolding errors and a simulation study showed better performance of PMF compared to traditional median filters when errors in Doppler velocity estimates are high. The PMF is suggested for filtering outliers from the spatial velocity field prior to applying any detection algorithms.

Waveforms based on ambiguity mitigation and clutter filtering enables the selection of waveforms for operational use. However, both operational requirement and hardware requirements ultimately play a major role in the selection of the waveform. First, faster scanning operational requirement for the IP1 radars reduces the dwell time thereby reducing the number of pulses that can be used for integration. Second, cheaper and low-power magnetron transmitter with very limited agility in terms of duty cycle that were used in CASA's IP1 radars reduced the possible waveforms for implementation. A dual-PRF waveform with  $N_1 = 40$  pulses at  $PRF_1 = 1.6$  kHz and  $N_2 = 54$  pulses at  $PRF_2 = 2.4$  kHz has been implemented in operational use. The random phase coding of magnetron has been used to mitigate range overlaid echoes. The operations range of IP1 radars is 40 km and hence, random phase coding was not used to extend the operating range but only to suppress range overlaid echoes. The dual-PRF waveform provides azimuth integration period of  $1^\circ$  at a scan speed of 21 deg/s. The clutter suppression ability and overlaid echo suppression based on operations of the IP1 radar has been described along with the application of dual-PRF unfolding for increasing the unambiguous velocity. A clutter suppression of about

30 dB and overlaid echo suppression of about 23 dB has been observed with the IP1 radars. The PMF filter along with staggered PRF waveforms provides a viable means to measure very high velocities at X-band.

## CHAPTER 5

### WIDEBAND WAVEFORMS FOR POLARIMETRIC RADARS WITH SOLID-STATE TRANSMITTERS

---

---

#### 5.1 Introduction

Weather radar systems using solid-state transmitters are becoming increasingly viable. The transition from traditional high powered transmitters to solid-state transmitter is also useful to realize a network of low cost electronically steered X-band radars. However, solid-state transmitters have low peak powers which degrades the sensitivity of the radar if used in a conventional way with narrow transmit pulse. Sensitivity requirements with low peak power transmitters necessitates the use of pulse compression waveforms. Pulse compression radars transmit long wideband pulses to achieve adequate sensitivity and range resolution. Pulse compression has been in use with hard target radars for several decades and significant advances have been made in the technology and implementation (Cook and Bernfeld, 1993; Skolnik, 1990). Pulse compression techniques for non-weather radar systems are well documented in literature (Skolnik, 1990; Peebles, 1998). Their applicability to weather radar, however, is relatively rare. Typically weather radar targets are extended volume scatterers and range side-lobes are a major source of error for quantitative applications (Mudukutore et al., 1998). Mismatch filtering techniques to improve the range side-lobes have been studied, keeping in mind the applicability to weather radar.

Although pulse compression waveforms provide adequate sensitivity they have a major drawback in providing coverage at close range. Pulse compression waveforms

suffer from blind zone that occur because the receiver does not receive any signal while the long pulse is being transmitted. The transmission of long pulses is necessary to achieve adequate sensitivity but results in blind ranges. Radars using pulse compression waveforms overcome blind range problem by staggering short and long pulses. The long pulse provides adequate sensitivity at farther ranges and short pulse provides coverage in the blind range region. However, alternating between long and short pulses reduces maximum unambiguous velocity. A pulse train of short pulse followed by a pulse train of long pulses can be used to provide adequate sensitivity and provide coverage in the blind range region. However, such a pulsing scheme will increase the dwell time resulting in slower scan speed.

In this paper a class of frequency diversity wideband waveforms are presented to mitigate low sensitivity of solid-state transmitters and also mitigate the blind zone problem associated with pulse compression. The proposed waveform is designed and implemented for a dual-polarization X-band radar operating in Simultaneous Transmit & Receive (STAR) mode. Frequency diversity is viable because a solid-state transmitters can achieve a much wider bandwidth with acceptable efficiency. The proliferation of low cost advanced digital processors, as well as the advances in digital transmitter control technology and low-power solid state transmitter technology makes the class of frequency diversity wideband waveforms viable for implementation. Some of the major considerations that needs to be taken into account for weather radars using solid-state transmitters is described in George et al. (2008).

This paper is organized as follows: Section 5.2 provides the relation between transmit waveform and sensitivity to develop a sensitivity mapped generalized waveform. The non-linear frequency modulation (NLFM) pulse compression waveform, its parameterization and associated compression filter design is presented in Section 5.3. The side lobe characterization of the NLFM pulse compression waveform is described in Section 5.4. The performance of the NLFM pulse compression waveform in the retrieval of the spectral moments and polarimetric variables for volume targets is

described in Section 5.5. A frequency diversity pulse compression waveform which mitigates the low sensitivity of solid state transmitter radars and mitigates blind range issues of pulse compression waveform is presented in Section 5.6. The paper ends with the summary and conclusions presented in Section 5.7.

## 5.2 Sensitivity Mapped Generalized Waveforms

The reflectivity is estimated from the received power at the reference plane and the equation assumes a common reference plane at the antenna feed horn port. The reflectivity is given by

$$Z_e = C' \bar{P}_{ref} R^2 \quad (5.1)$$

In the above equation  $\bar{P}_{ref}$  is the received power at the reference antenna port,  $R$  is the radar range and  $C'$  is a constant given below.

$$C' = \frac{1}{\pi^5 |K_w|^2} \left( \frac{2}{c\tau} \right) \left[ \frac{(4\pi^3 l_{wg}^2)}{P_t G_0^2} \right] \left( \frac{8 \ln 2}{\pi \theta_B \phi_B} \right) \lambda^2 \quad (5.2)$$

In the above equation  $K_w$  is the dielectric factor of water,  $\tau$  is the pulse width,  $P_t$  is the peak transmit power,  $G_0/l_{wg}$  is the antenna gain including the waveguide loss,  $\theta_B$  and  $\phi_B$  are the 3-db beam-widths, and  $\lambda$  is the operating wavelength of the radar. In practice  $Z_e$  is expressed in  $mm^2 m^{-1}$  (dBZ in decibel scale). The radar equation can now be written as

$$Z_e [dBZ] = \bar{P}_{ref} [dBm] + C [dB] + 20 \log (R [km]) \quad (5.3)$$

where the radar constant  $C$  is given by

$$C = 10 \log \left\{ \frac{1}{\pi^5 |K_w|^2} \left( \frac{2}{c\tau} \right) \left[ \frac{(4\pi^3 l_{wg}^2)}{P_t G_0^2} \right] \left( \frac{8 \ln 2}{\pi \theta_B \phi_B} \right) \lambda^2 10^{21} \right\} \quad (5.4)$$

It is customary to define the minimum detectable reflectivity at a specified range when the signal-to-noise ratio is 0 dB (Bringi and Chandrasekar, 2001). Therefore, the sensitivity of the radar is studied in terms of the minimum detectable reflectivity. The

sensitivity is governed by the radar constant given in (5.4) and the receiver equivalent noise bandwidth which dictates the amount of noise power in the received signal. For a given antenna the sensitivity is directly proportional to the receiver bandwidth and inversely proportional to the product of pulse width and peak power. Conventional weather radars operating at S-band such as WSR-88D and CSU-CHILL transmit a  $1\mu s$  pulse with peak power in excess of 500 kW. However, solid-state transmitters have low peak power and are generally on the order of 100 W or less. Therefore, in order to attain adequate sensitivity a much longer pulses must be transmitted. One of the drawbacks of improving sensitivity solely by transmitting long pulses is degradation of range resolution. The resolution of the measurements along range is a function of the transmit pulse width. Pulse compression technique using modulated long pulses have been used to improve sensitivity and achieve range resolution similar to a short pulse (Skolnik, 1990; Peebles, 1998).

Pulse compression waveforms enables the use of low peak power transmitter to achieve adequate sensitivity but these waveforms have extended blind ranges or blind zone. The inherent problem of using a single antenna is that the antenna is not used in receive mode while the waveform is being transmitted. Therefore, there is no received signal for the duration of the time while the transmission is active. This results in a blind range (blind zone or range eclipsing) for the radar where there is no observations available. The problem of blind range has been addressed by alternating short and long pulses (Skolnik, 1990). Such solutions have be implemented for weather radars using pulse compression (Nakagawa et al., 2005). However, alternating between short and long pulses typically lead to two drawbacks. First, if the long and short pulses are switched on a pulse-to-pulse basis then the maximum unambiguous velocity is halved. Second, if a pulse train of short pulses is alternated with a pulse train of long pulses then the dwell times is made much larger.

In this section a sensitivity mapped generalized waveform is proposed that uses frequency diversity to mitigate blind range and pulse compression waveform to negate

the impact of low peak power of solid-state transmitters. Frequency diversity is viable because a solid-state transmitters can achieve a much wider bandwidth with acceptable efficiency. In addition, the electronically scanned (phase-phase steering) will employ solid-state transmit and receive (T/R) modules making it critical to design waveforms for such systems. For a generalized transmit-waveform, the complex envelope can be written as a sum of  $N$  components. In order to be able to avoid contamination of echoes from these individual components from the various ranges, the receiver must be able to separate the received signals corresponding to each component. This is accomplished by frequency diversity. The transmit pulse is a frequency-diversity pulse compression waveform. The complex envelope of the generalized waveform is given by

$$g(t) = \sum_{i=1}^N g_i(t - T_{i-1}) e^{j2\pi f_i(t - T_{i-1})} \quad (5.5)$$

$$\text{and} \quad T_1 > T_2 > T_3 > \dots > T_N \quad (5.6)$$

$$\text{and} \quad \sum_{i=1}^N T_i \leq T_{max} \quad (5.7)$$

where  $g_i(t)$  is the complex envelope of the  $i^{th}$  component of the waveform at a frequency offset  $f_i$  and  $T_i$  is the pulse width of each component with  $T_0 = 0$ . By design guidelines the first component is the longest with the largest blind range and the last component is the shortest with minimal blind range. The transmit waveform is subsequently obtained by mapping the operational and hardware requirements as given below

$$g(t) = \varphi(Z_{min}(r), T_{max}, P_t, T_s) \quad (5.8)$$

where  $T_{max}$  is the maximum transmit pulse length limited by the hardware,  $Z_{min}(r)$  is the required sensitivity at range  $r$ ,  $P_t$  is the peak transmit power and  $T_s$  is the pulse repetition time (PRT). For example, based on the requirement of 10 dBZ sensitivity at 40 km using a transmitter with  $P_t = 100W$  a frequency diversity waveform consisting

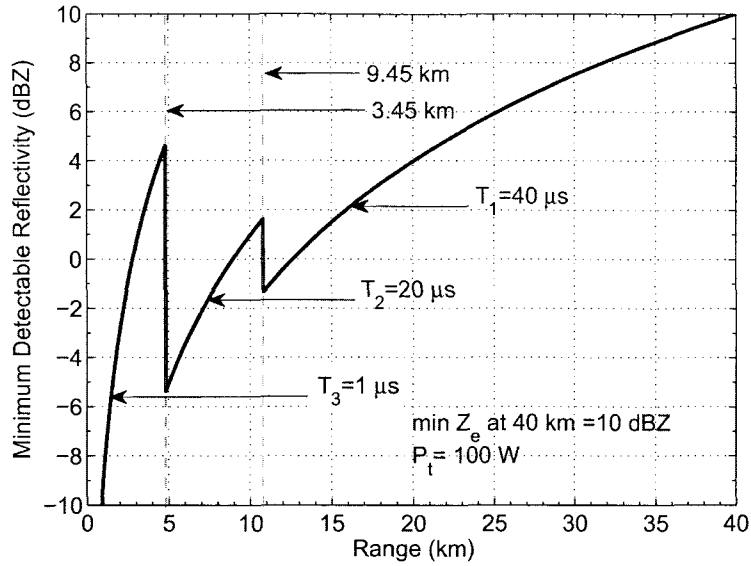


Figure 5.1: Minimum detectable reflectivity of a sensitivity mapped frequency diversity waveform with three components. The peak transmit power  $P_t = 100\text{ W}$  operating at X-band.

of three components is obtained. The sensitivity from the three component frequency diversity is shown in Fig. 5.1 where the pulse widths of the three components are  $T_1 = 40\ \mu\text{s}$ ,  $T_2 = 20\ \mu\text{s}$  and  $T_3 = 1\ \mu\text{s}$ . A similar waveforms is described by Carswell et al. (2008)

### 5.3 Pulse compression waveforms

A basic pulse compression waveform consists of a coding signal that modulates the transmitted pulse. Phase and frequency modulation have been widely used for pulse compression applications. For a pulse compression waveform the complex envelope of the transmitted wideband pulse is given by

$$g(t) = u(t) \exp \left\{ j2\pi \int_{-T/2}^t f(\tau) d\tau \right\} \quad (5.9)$$

where  $u(t)$  and  $T$  are the envelope, length of the transmitted pulse respectively and  $g(t)$  is the complex envelope of the transmitted pulse. The frequency modulation

is governed by  $f(t)$ . The matched filter which maximizes the signal-to-noise ratio is obtained as  $g^*(-t)$  where  $*$  indicates complex conjugate. The matched filter is completely determined by the complex envelope of the transmit pulse.

### 5.3.1 Nonlinear frequency modulation (NLFM)

The FM characteristic similar to waveform described by Griffiths and Vinagre (1994) is proposed for pulse compression. The FM characteristic is decomposed into linear and nonlinear component as

$$f(t) = \begin{cases} \frac{B}{T} \left( \frac{1 - k_B}{1 - k_T} \right) & |t| \leq T(1 - k_T) \\ \varphi(t) \operatorname{sgn}(t) & |t| > T(1 - k_T) \end{cases} \quad (5.10)$$

where  $B$  is the total bandwidth of the chirp;  $0 < k_T < 1$  and  $0 < k_B < 1$  are parameters that control non-linearity of the chirp frequency. The nonlinear portion of the chirp  $\varphi(t)$  is given by

$$\varphi(t) = \mathbf{G}^{-1} \begin{bmatrix} B(1 - k_B) \\ B \\ B(1 - k_B) \\ T(1 - k_T) \end{bmatrix} \begin{bmatrix} t^2 & 0 & 0 \\ 0 & t & 0 \\ 0 & 0 & 1 \end{bmatrix} \quad (5.11)$$

where

$$\mathbf{G} = \begin{bmatrix} T^2(1 - k_T)^2 & T(1 - k_T) & 1 \\ T^2 & T & 1 \\ 2T(1 - k_T) & 1 & 0 \end{bmatrix}. \quad (5.12)$$

Figure 5.2 shows the frequency characteristics of the nonlinear FM given in (5.10). A major disadvantage of pulse compression waveforms are the presence of range side-lobes. Very low side-lobe level (SLL) are essential for weather radar applications as very strong gradients of reflectivity up to 30-40 dB/km can occur in precipitation (Bringi and Chandrasekar, 2001). The side-lobe level is often described in terms of peak side-lobe level (PSL) and integrated side lobe level (ISL) (Mudukutore et al., 1998). It is important to have low ISL because weather radars observe volume targets that extend over large areas. The range side-lobes can be reduced by the application

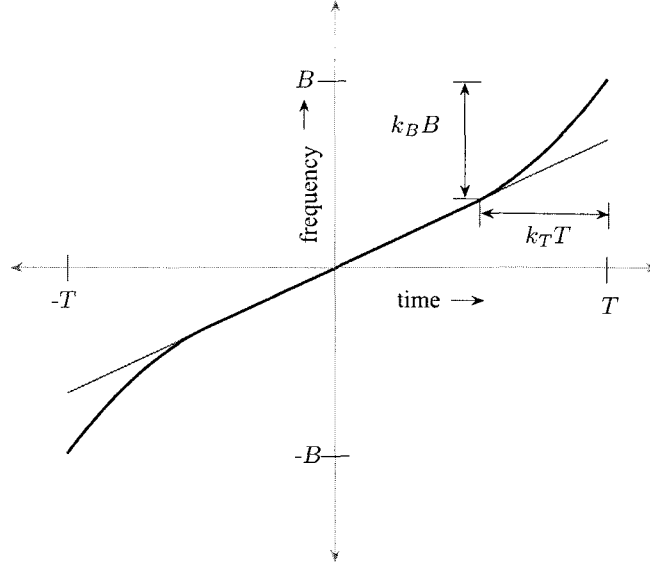


Figure 5.2: Nonlinear FM characteristics

of a compression filter that is not matched to the transmit pulse. The application of mismatch filters results in a loss of signal-to-noise ratio (SNR) as the compression filter is no longer designed to maximize signal-to-noise ratio.

### 5.3.2 Compression filters

The range side-lobes can be reduced by using a mismatch filter. The mismatch filters are obtained by using standard window functions and least-squares filters.

#### 5.3.2.1 Window function filters

Standard window functions have been used to shape the spectrum of the transmitted pulse to attain lower side-lobes. Ideally the square root of the window functions must be applied to the transmit pulse which results in a matched filters with low side-lobe levels. However, this would require a linear power amplifier which is not an efficient in utilizing power. Thus, window functions are applied on receive to improve

side-lobe performance. The application of standard window functions such as Taylor, Hamming and Chebyshev weighting are readily available from literature (Cook and Bernfeld, 1993; Skolnik, 1990; Peebles, 1998). The loss in SNR is given by

$$SNR_{loss} = \frac{\left(\sum_{n=1}^N w_n\right)^2}{N \sum_{n=1}^N w_n^2} \quad (5.13)$$

The loss in SNR is typically determined by the window function used. A very aggressive window function will have a loss in excess of 5 dB. There is a trade-off between side-lobe reduction and loss in SNR.

### 5.3.2.2 Optimal ISL filter

Mismatch filters obtained from least-squares minimization have been known to provide good performance for some pulse compression waveforms. Ackroyd and Ghani (1973) proposed an inverse filter based on Wiener-Hopf equations and Mudukutore et al. (1998) evaluated the applicability of inverse filter using Barker codes for weather radars. Baden and Cohen (1990) proposed the optimal ISL filter that minimized the ISL in a least squares sense while Cilliers and Smit (2007) provided a generalization of the optimal ISL filter by extending the minimization in  $L_p$  norm sense. The following section describes the derivation of the compression filter using  $L_2$  norm (least squares). Let  $\mathbf{G}$  be the transmit convolution matrix obtained from the discrete complex envelope of the transmit pulse  $\mathbf{g}$  and  $\mathbf{h}$  be the FIR filter coefficients of the required compression filter. The output of the compression filter with the transmit pulse as the input is given by

$$\mathbf{y} = \mathbf{G}^T \mathbf{h} \quad (5.14)$$

where  $\mathbf{y}$  is the output of the compression filter. Let  $\mathbf{G}_m$  be the modified transmit convolution matrix obtained by deleting the columns of  $\mathbf{G}$  that corresponds to the main-lobe of the ambiguity function obtained from  $\mathbf{y}$ . The ISL is considered as the

cost function that has to be minimized to obtain the FIR filter coefficients. The ISL is given by

$$ISL = f(\mathbf{h}) = \mathbf{h}^H \mathbf{G}_m^* \mathbf{G}_m^T \mathbf{h} \quad (5.15)$$

The ISL is minimized by using using method of Lagrange Multipliers with the constraint on the peak of  $\mathbf{y}$  as  $\mathbf{g}^T \mathbf{h} = \alpha$  where  $\alpha$  is an arbitrary constant. The equation to be solved is obtained from the Lagrangian given below.

$$\frac{\partial f(\mathbf{h})}{\partial \mathbf{h}^*} + \lambda \frac{\partial \Re e(\mathbf{g}^T \mathbf{h} - \alpha)}{\partial \mathbf{h}^*} = \mathbf{0} \quad (5.16)$$

The closed form solution for the above equation is given below.

$$\mathbf{h} = \frac{\alpha (\mathbf{G}_m^* \mathbf{G}_m^T)^{-1} \mathbf{g}^H}{\mathbf{g} (\mathbf{G}_m^* \mathbf{G}_m^T)^{-1} \mathbf{g}^H} \quad (5.17)$$

The minimum ISL compression FIR filter is normalized to have unity gain at zero frequency and is given by

$$\mathbf{b} = \frac{\mathbf{h}}{|\langle \mathbf{1}, \mathbf{h} \rangle|} \quad (5.18)$$

where  $\mathbf{1}$  is a vector whose elements are 1 and  $\langle \cdot, \cdot \rangle$  represents inner-product.

#### 5.4 Side lobe characterization for NLFM pulse compression

The performance of the pulse compression waveforms depends on many factors such as  $BT$ ,  $k_T$ ,  $k_B$  and compression filter used. For a given value of  $B$  and  $T$  there are many waveforms that can be designed by varying  $k_T$  and  $k_B$ . In general the chirp bandwidth  $B$  is limited by the base-band sampling frequency as dictated by sampling theorem and the pulse lengths are selected based on the hardware limitations and sensitivity mapping as described in Section 5.2. The envelope  $u(t)$  is selected such that there are no instantaneous rise time which reduces ringing in the transmitted spectrum. A Tukey window is proposed because a single tunable parameter,  $\alpha_T$ , controls the rise time and fall time of the pulse envelope. The tuning parameter is

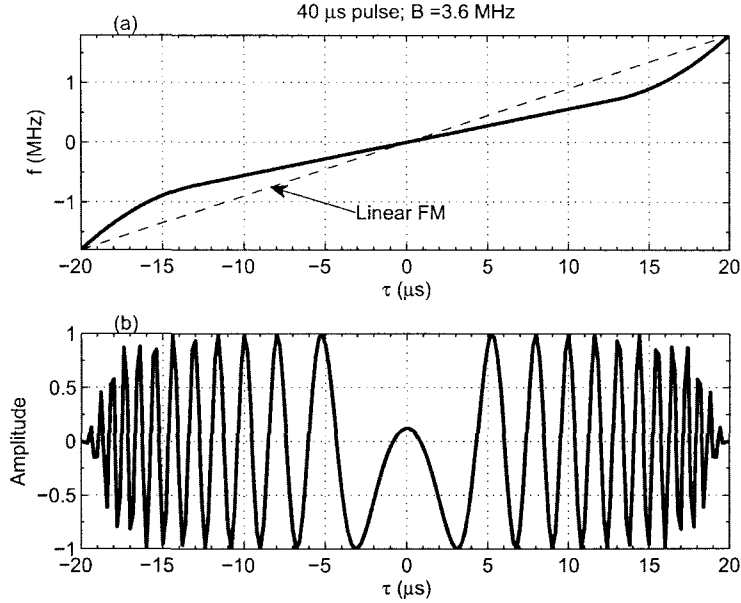


Figure 5.3: Nonlinear FM Pulse compression waveform (a) FM characteristics (b) Amplitude of transmit pulse. The Pulse compression waveform has a nonlinear chirp of  $B = 3.6 \text{ MHz}$ ,  $T = 40 \text{ }\mu\text{s}$  pulse length, and base-band sampling frequency  $f_s = 5 \text{ MHz}$ .

part of the specification of the transmit waveform. Hence, in practical conditions the waveform is governed by three parameters:  $\alpha_T$ ,  $k_T$  and  $k_B$ . Figure 5.3 shows a waveform with a chirp bandwidth  $B = 3.6 \text{ MHz}$  and  $T = 40 \text{ }\mu\text{s}$  operating at a base band sampling frequency  $f_s = 5 \text{ MHz}$ . The waveform parameters are  $\alpha_T = 0.127$ ,  $k_T = 0.354$  and  $k_B = 0.6$ .

#### 5.4.1 Doppler tolerance

The main drawback of the minimum ISL filter is limited Doppler tolerance while the window function filter is known to be Doppler tolerant. To compare the performance of the compression filter to Doppler shifts the received signal is shifted in frequency based on the mean Doppler velocity of the resolution volume. The increase in side-lobe level due to Doppler shift is shown as a function of velocity in Fig. 5.4. The peak side-lobe level and integrated side-lobe level are almost invariant

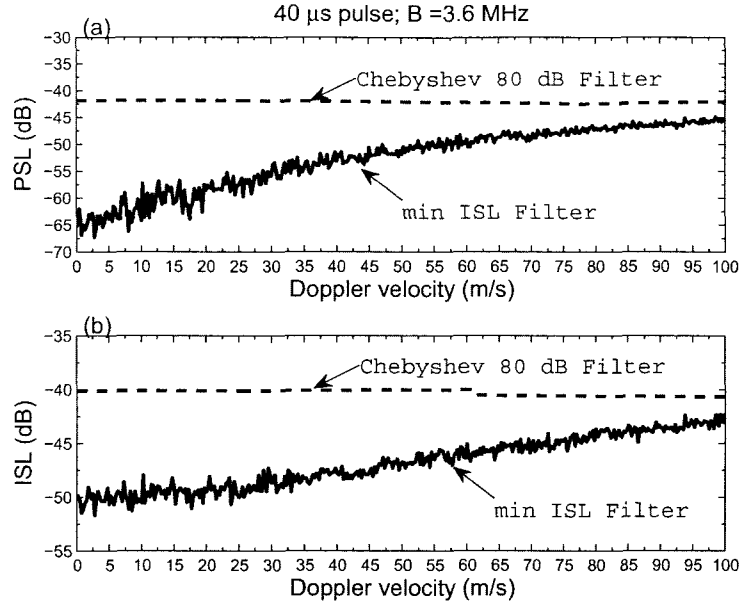


Figure 5.4: Side lobe level as a function of Doppler velocity (a) Peak size-lobe level (b) Integrated side-lobe level. The Pulse compression waveform has a nonlinear chirp of  $B = 3.6 \text{ MHz}$ ,  $T = 40 \mu\text{s}$  pulse length, and base-band sampling frequency  $f_s = 5 \text{ MHz}$ .

with velocity for the window function while both peak side-lobe level and integrated side-lobe level increase for the minimum ISL filter as shown in Fig. 5.4(a) and (b). But it is important to note that although the side-lobe level increases with velocity the performance of minimum ISL filter is much better than the 80 dB Chebyshev window filter. The ISL of the minimum ISL filter is better than -45 dB for Doppler velocities less than 50 m/s.

#### 5.4.2 Phase noise tolerance

The nonlinear FM is implemented as a digital FM signal and up-converted to the RF frequency. The phase on the transmitted sub-pulses have random phase errors due to the phase noise of the system. The individual elements in the radar system such as STALO, mixers, transmitter contribute to the system phase noise. The system phase noise has an impact on the performance of the pulse compression waveform. The

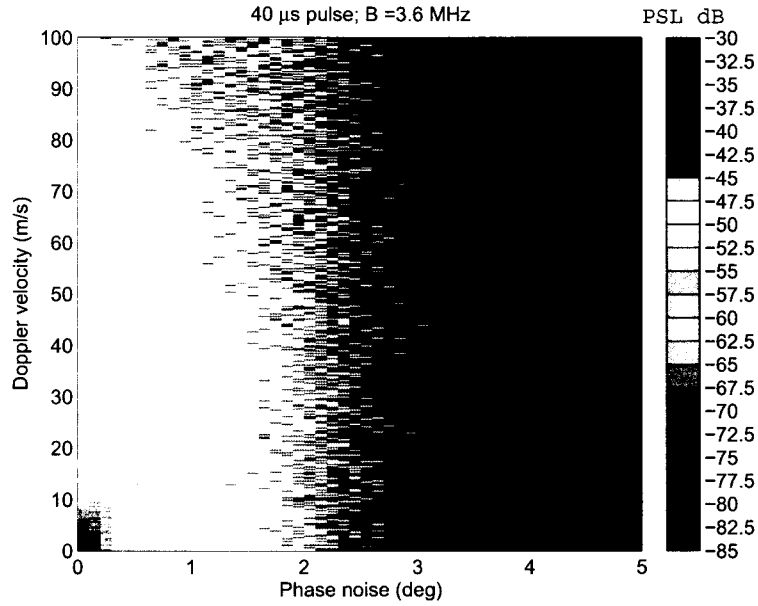


Figure 5.5: Peak side-lobe level as a function of Doppler velocity and system phase noise. The Pulse compression waveform has a nonlinear chirp of  $B = 3.6 \text{ MHz}$ ,  $T = 40 \mu\text{s}$  pulse length, and base-band sampling frequency  $f_s = 5 \text{ MHz}$ .

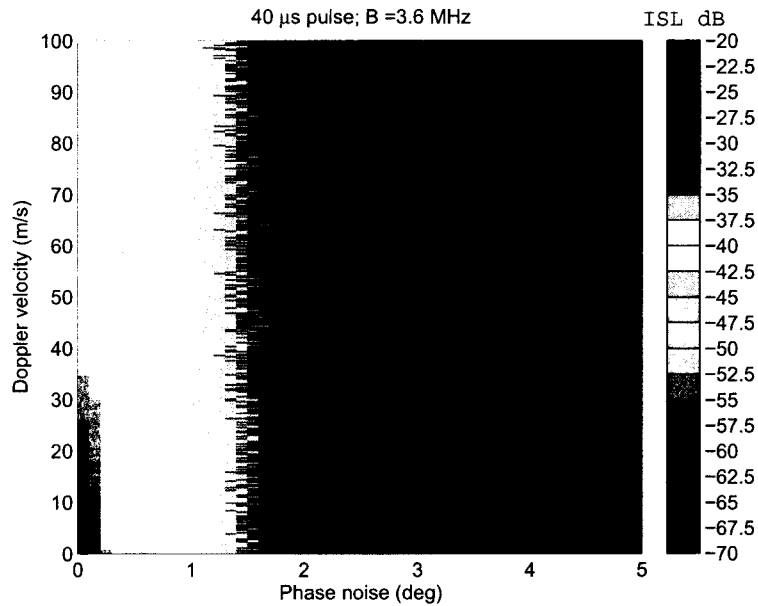


Figure 5.6: Integrated side-lobe level as a function of Doppler velocity and system phase noise. The Pulse compression waveform has a nonlinear chirp of  $B = 3.6 \text{ MHz}$ ,  $T = 40 \mu\text{s}$  pulse length, and base-band sampling frequency  $f_s = 5 \text{ MHz}$ .

PSL and ISL as a function of phase noise is shown in Fig.5.5 and Fig.5.6 respectively. It can be observed that both PSL and ISL decrease with increase in phase noise. A phase noise of 0.25 deg is required to achieve an ISL better than 50 dB and phase noise of 0.5 deg is required to achieve an ISL better than 40 dB. Therefore, phase noise is an important factor that must be taken into consideration to ascertain the performance of a pulse compression radar.

## 5.5 Pulse compression for volume targets

The impact of phase noise, Doppler velocity and choice of filter was described in the previous sections. In this section we describe the resolution and receiver bandwidth of the proposed pulse compression waveform. In addition, the effect of the side lobe levels on the estimated Doppler spectral moments and polarimetric variables for volume targets is presented.

### 5.5.1 Range resolution

In a traditional pulsed Doppler weather radar the range resolution is determined by the transmitted pulse width. However, the range resolution with a pulse compression waveforms is determined by the chirp bandwidth  $B$  and compression filter. In a matched filtered the range resolution is  $c/2B$  where  $c$  is the speed of light. The range resolution with a pulse compression waveform is obtained by simulating a point target and calculating the effective pulse width after the compression (Peebles, 1998). Figure 5.7 shows a comparison of the range resolution using a minimum ISL filter and Chebyshev-80 dB mismatch filter. The comparison of range resolution is shown for pulse compression waveform using  $B = 3.6 \text{ MHz}$ ,  $T = 40 \mu\text{s}$  and  $T = 20 \mu\text{s}$  pulse length. The minimum ISL filter provides a range resolution  $\Delta r = 60 \text{ m}$  for both  $T = 40 \mu\text{s}$  and  $T = 20 \mu\text{s}$  while Chebyshev-80 dB mismatch filter provides a range resolution  $\Delta r = 118 \text{ m}$  and  $\Delta r = 96 \text{ m}$  for  $T = 40 \mu\text{s}$  and  $T = 20 \mu\text{s}$  respectively. The minimum ISL filter provides better range resolution than Chebyshev-80 dB mismatch filter in addition to providing better range side lobe suppression.

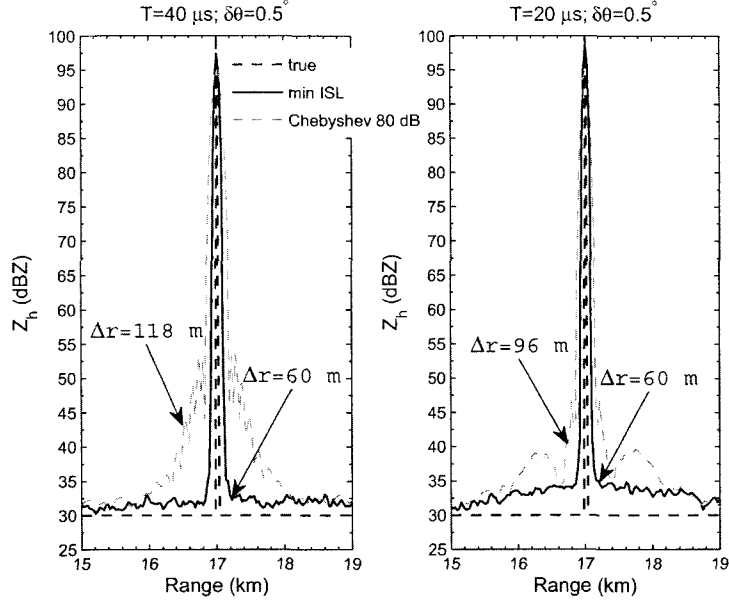


Figure 5.7: Comparison of range resolution using Chebyshev-80 dB mismatch filter and minimum ISL filter for Pulse compression waveform using  $B = 3.6 \text{ MHz}$ ,  $T = 40 \mu\text{s}$  and  $T = 20 \mu\text{s}$  pulse length, and base-band sampling frequency  $f_s = 5 \text{ MHz}$ .

### 5.5.2 Receiver bandwidth

The spectrum of the transmitted pulse is shown in Fig. 5.8(a) along with the filter characteristics of the minimum ISL filter and 80 dB Chebyshev window mismatch filter. It can be observed that the minimum ISL filter retains most of the frequency components while the 80 dB Chebyshev window filter has a much narrower bandwidth. Both the filters reduce the side-lobe level as shown in Fig. 5.8(b). However, the minimum ISL filter has a much lower side-lobe level when compared to the window function. This is an obvious results since the minimum ISL filter was designed to minimize the total energy in the side-lobes. The bandwidth of the receiver is finite and this finite bandwidth results in the loss of in received power because some of the spectral components of the received signal will be filtered out. It is important to have a filter which does not have a large finite bandwidth loss ( $\ell_r$ ). The finite bandwidth loss must be taken into account while estimating a calibrated reflectivity factor( $Z_h$ ).

Table 5.1: Finite bandwidth filter loss for frequency diversity pulse compression waveform,  $B = 3.6 \text{ MHz}$

Filter	$T = 20 \mu s, \alpha_T = 0.1944$	$T = 40 \mu s, \alpha_T = 0.1268$
	Filter loss ( $\ell_r$ )	Filter loss ( $\ell_r$ )
min ISL	2.49 dB	1.83 dB
Hamming	3.47 dB	3.71 dB
Hann	3.70 dB	3.92 dB
Chebyshev 80 dB	4.65 dB	4.88 dB

Table 5.1 lists the finite bandwidth loss for various compression filters applied to the proposed pulse compression waveform. The minimum ISL filter has the least finite bandwidth loss  $\ell_r = 2.49 \text{ dB}$  for  $T = 20 \mu s$  pulse and  $\ell_r = 1.83 \text{ dB}$  for  $T = 40 \mu s$ . The mismatch filter using window functions which provide relatively lesser finite bandwidth loss do not have very good performance in terms of side lobe suppression. The Chebyshev 80 dB mismatch filter provides good side lobe suppression but due to its narrower bandwidth it also has a larger finite bandwidth loss  $\ell_r \geq 4.5 \text{ dB}$ . The minimum ISL filter has lower finite bandwidth loss when compared to window based mismatch filter in addition to providing better range side lobe suppression.

### 5.5.3 Impact on Doppler spectral moments

A simulation is performed to evaluate the impact of SLL. The simulations of weather echoes are based on the methodology presented by Chandrasekar et al. (1986) and this methodology is used to simulate the received signal from pulse compression waveform as described by Mudukutore et al. (1998). A trapezoidal profile of reflectivity is used to simulate the range profile. The height and gradient of reflectivity can be controlled to evaluate the impact of reflectivity variation along range.

Figure 5.9 shows the simulation results for a  $T = 40 \mu s$  pulse compression waveform with  $N = 64$  pulses. The simulations were carried out for a spectral width of  $\sigma_v = 2 \text{ m/s}$  using a PRF of 2 kHz. Simulations were repeated 100 times for the same reflectivity profile. The dashed gray line in Fig. 5.9(a) is the true profile with a

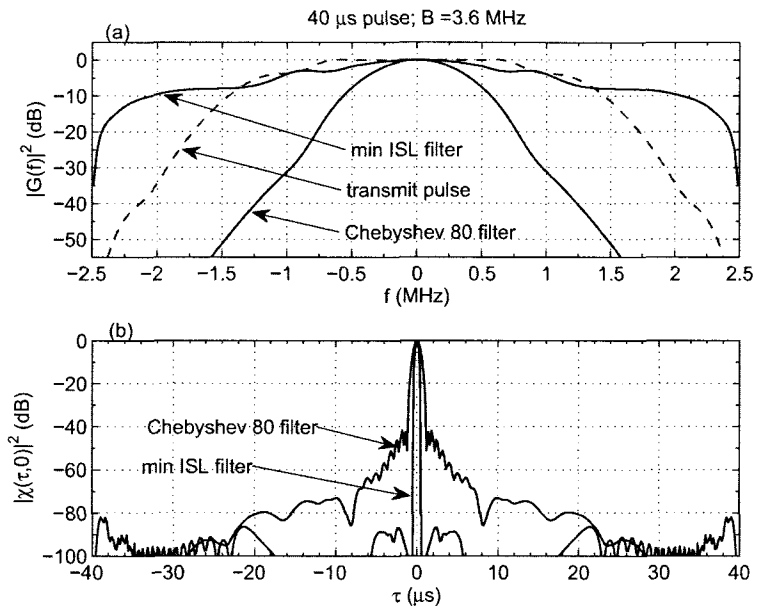


Figure 5.8: (a) Spectrum of transmit pulse and compression filter characteristics (b) Comparison of ambiguity function with 80 dB Chebyshev window filter and minimum ISL filter. The Pulse compression waveform has a nonlinear chirp of  $B = 3.6$  MHz,  $T = 40$   $\mu\text{s}$  pulse length, and base-band sampling frequency  $f_s = 5$  MHz.

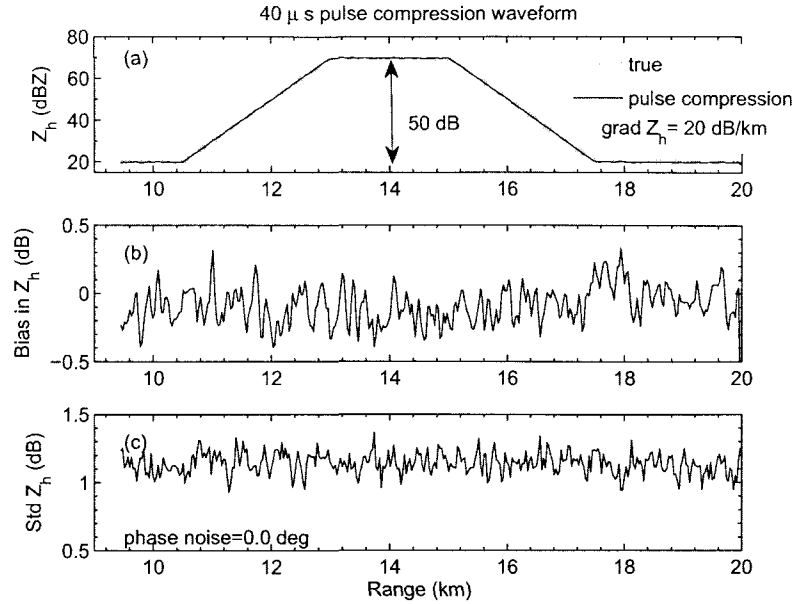


Figure 5.9: Observation of a trapezoidal reflectivity profile with 20 *db/km* gradient. (a) Observed mean reflectivity (b) Bias in measured reflectivity (c) Standard deviation of reflectivity. The Pulse compression waveform has a nonlinear chirp of  $B = 3.6 \text{ MHz}$ ,  $T = 40 \mu\text{s}$  pulse length, and base-band sampling frequency  $f_s = 5 \text{ MHz}$ . The phase noise of the system is 0 degrees

reflectivity gradient of 20 *db/km*. The floor of the profiles is well above the noise floor. Figure 5.9(a) shows the estimated reflectivity for an ideal system with zero phase noise. It can be observed that ISL does not bias the reflectivity estimates more than 0.5 dB (Fig. 5.9(b)) and the standard deviation are less than 1.5 dB.

However, the presence of phase errors will lead to degraded performance in side-lobe levels. A simulation with the same parameters are described above is performed but with a phase noise of 0.5 degree. Figure 5.10 and Fig. 5.11 show the estimated reflectivity and error in the estimated reflectivity for two different reflectivity profile. The gradient of reflectivity is 20 *dB/km* for both the cases.

It can be observed from Fig. 5.10 and Fig. 5.11 that an change of 25 dB in range does not bias the reflectivity estimates but a change of 50 dB (Fig. 5.11(a)) introduces a bias greater than 3 dB due to side lobes. Therefore, phase noise plays a

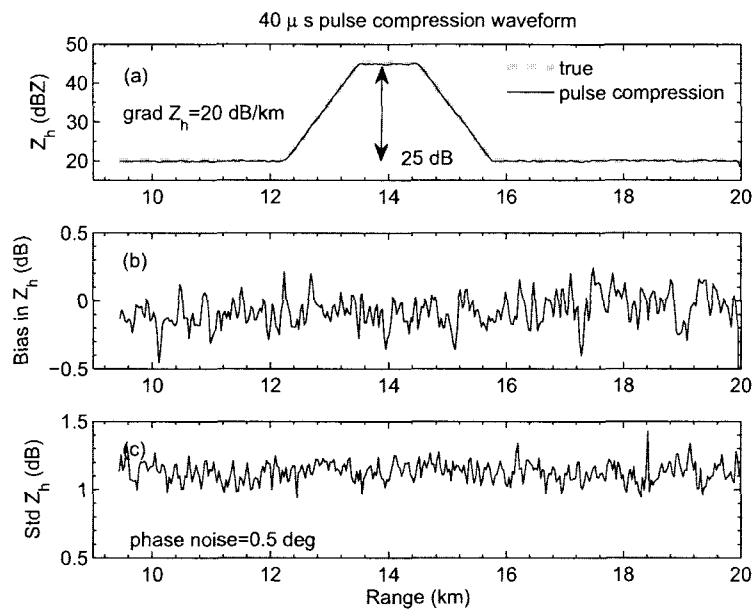


Figure 5.10: Observation of a trapezoidal reflectivity profile with 20  $db/km$  gradient. (a) Observed mean reflectivity (b) Bias in measured reflectivity (c) Standard deviation of reflectivity. The Pulse compression waveform has a nonlinear chirp of  $B = 3.6 MHz$ ,  $T = 40 \mu s$  pulse length, and base-band sampling frequency  $f_s = 5 MHz$ . The phase noise of the system is 0.5 degrees

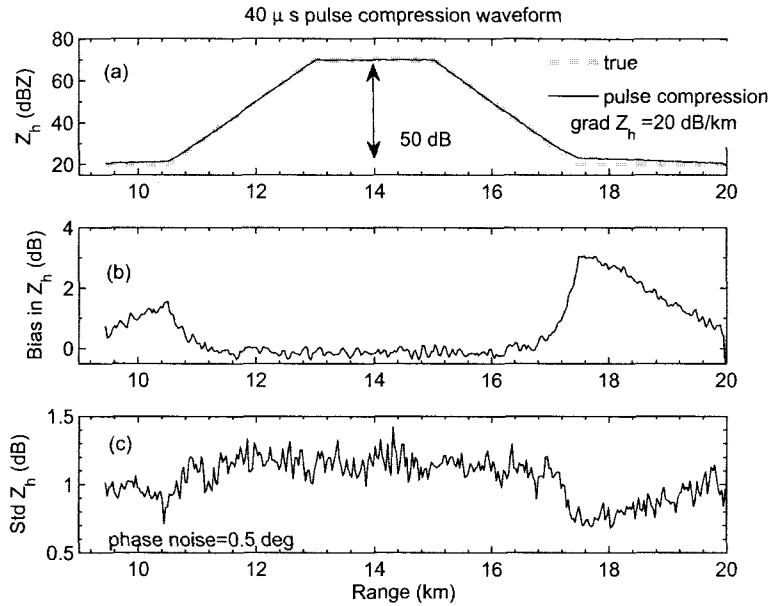


Figure 5.11: Observation of a trapezoidal reflectivity profile with 20  $db/km$  gradient. (a) Observed mean reflectivity (b) Bias in measured reflectivity (c) Standard deviation of reflectivity. The Pulse compression waveform has a nonlinear chirp of  $B = 3.6 \text{ MHz}$ ,  $T = 40 \mu s$  pulse length, and base-band sampling frequency  $f_s = 5 \text{ MHz}$ . The phase noise of the system is 0.5 degrees

important role in governing the performance of pulse compression waveform.

Very high gradients in reflectivity ( $Z_h$ ) within the long pulse can occur at the edges of strong convective cells and regions where there is clutter contamination. A step function with varying step sizes is simulated to analyze the limitation of the pulse compression waveform with a phase noise of  $\delta\theta = 0.25^\circ$  operating at X-band and  $PRF = 2 \text{ kHz}$ . The floor of the step function is set at 30 dBZ so that low signal-to-noise ratio is avoided. The step size is increased from 20 dB to 50 dB in increments of 10 dB. The mean Doppler velocity is set to two levels; one at 10 m/s in the 30 dBZ region and -10 m/s in the stepped reflectivity region. The impact of the step size on the observed reflectivity and mean Doppler velocity is shown in Fig. 5.12 and Fig. 5.13 respectively for  $T = 40 \mu\text{s}$ . Figure 5.12 shows the input profiles (left panel) and the bias in the estimated reflectivity (right panel). The bias in reflectivity is within acceptable levels of  $\pm 0.5$  dB for a step size up to 40 dB but the impact of side lobe is clearly seen as a biased reflectivity estimate for a step size of 50 dB. Similar results were obtained for  $T = 20 \mu\text{s}$  but are not shown in this paper. The ISL of at least 40 dB is required to handle large gradients in reflectivity and provide estimated Doppler moments with acceptable bias.

#### 5.5.4 Impact on polarimetric variables

The simulation set up described in Section 5.5.5.3 is also used to analyze the impact of range side lobes on the retrieval of polarimetric variables. Two sets of polarimetric variables are used; One for the floor of the step function and the other for the stepped region. The differential reflectivity ( $Z_{dr}$ ) is set to 1 dB and 3 dB; Differential phase  $\phi_{dp}$  is set to  $-65^\circ$  and  $35^\circ$ ; Co-polar correlation coefficient ( $\rho_{hv}$ ) between the horizontal and vertical polarization channel is set to 0.99 and 0.88. Lower values of  $\rho_{hv}$  can occur in very strong reflectivity cores usually containing hail/ice. The  $Z_{dr}$  profiles and the bias in estimated  $Z_{dr}$  is shown in Fig.5.14 and the bias is within 0.1 dB for reflectivity step sizes up to 40 dB. For step size of 50 dB the presence

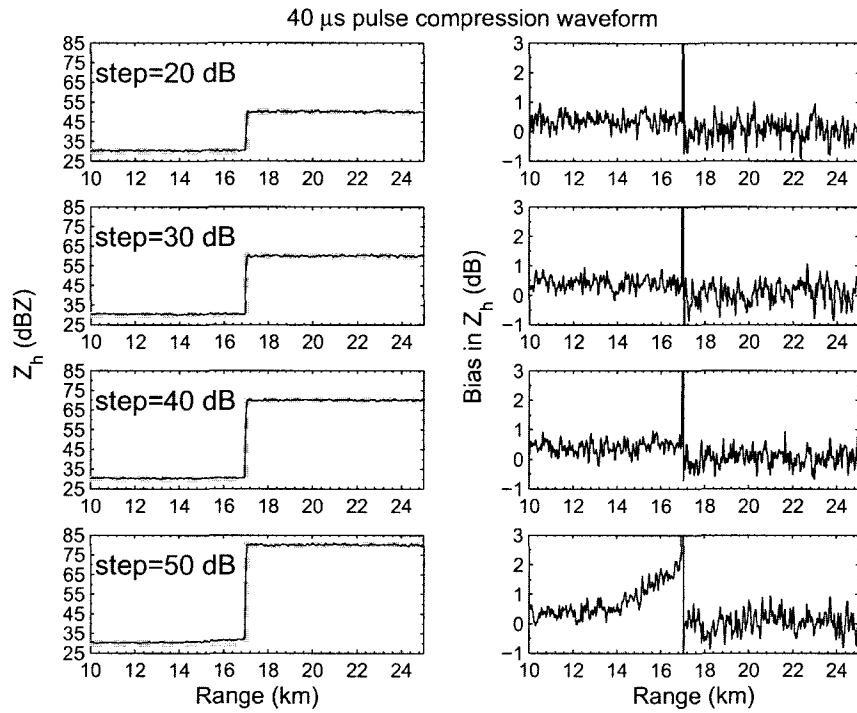


Figure 5.12: The impact of side lobe level on  $Z_h$  using a step function profile with varying step sizes of reflectivity with phase noise  $\delta\theta = 0.25^\circ$ .

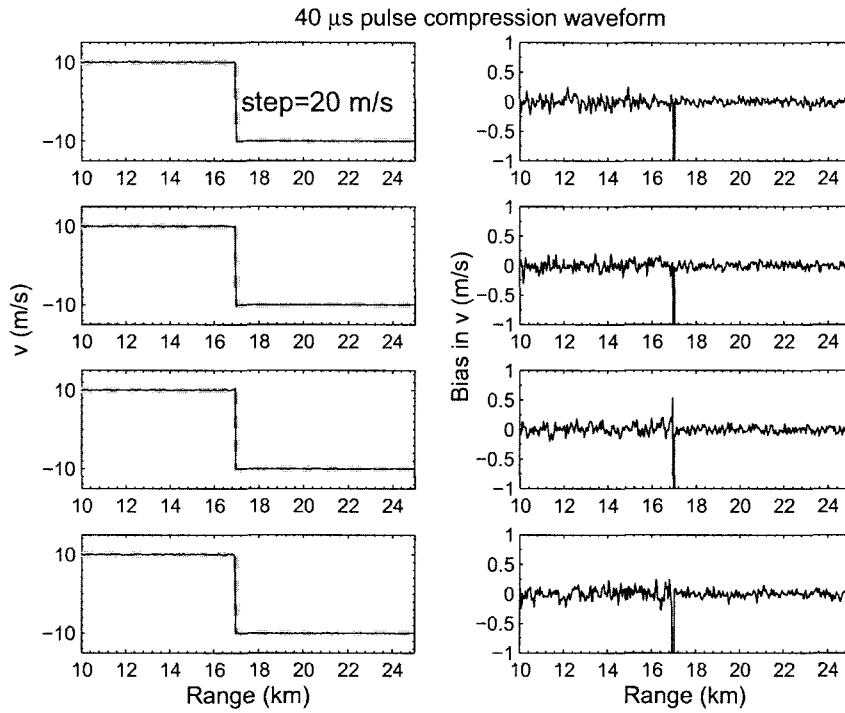


Figure 5.13: The impact of side lobe level on  $v$  using a step function profile with varying step sizes of reflectivity with phase noise  $\delta\theta = 0.25^\circ$ .

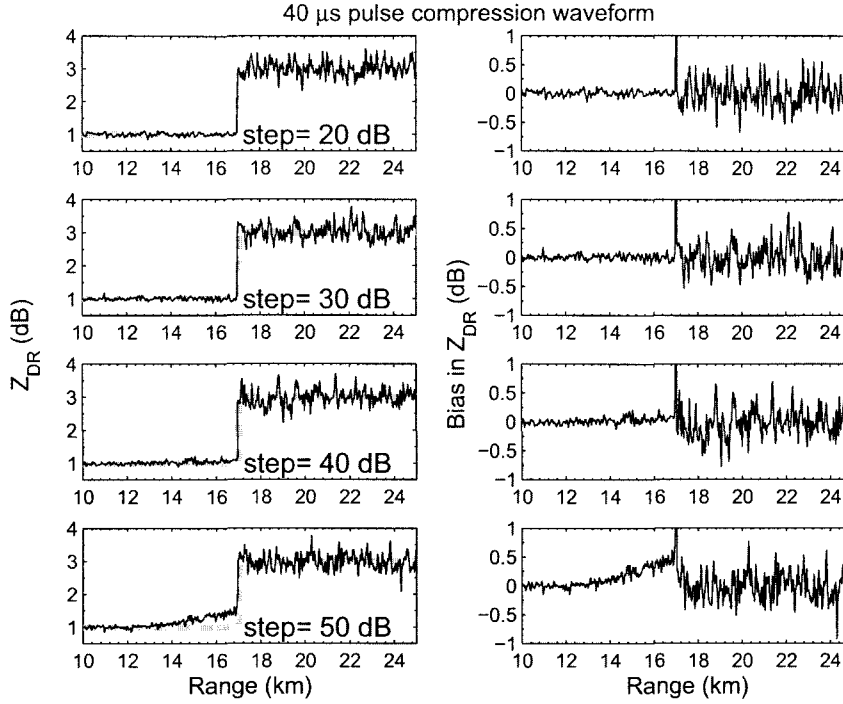


Figure 5.14: The impact of side lobe level on  $Z_{dr}$  using a step function profile with varying step sizes of reflectivity with phase noise  $\delta\theta = 0.25^\circ$ .

of range side lobes results in larger biases in  $Z_{dr}$ . The bias in  $Z_{dr}$  exceeds 0.25 dB for step size greater than 40 dB. The profile and bias in estimated differential propagation phase shift ( $\phi_{dp}$ ) is shown in Fig. 5.15. The bias in  $\phi_{dp}$  is not very significant even at large step size of 50 dB. The most significant impact of the range side lobe can be seen in  $\rho_{hv}$ . The  $\rho_{hv}$  profiles and bias in estimated  $\rho_{hv}$  is shown in Fig. 5.16. The bias in  $\rho_{hv}$  is not very significant for step sizes up to 40 dB. However, there is a dramatic reduction in  $\rho_{hv}$  in the vicinity of the step function when there is a 50 dB step.  $\rho_{hv}$  drops to less than 0.8 from 0.99 due to the presence of range side lobe contamination from a region of low  $\rho_{hv}$ . It is important to note that such drop in  $\rho_{hv}$  will not occur if the  $\rho_{hv}$  in the range side lobe is same or as high as the range gate of interest.

The accuracy of the polarimetric variables such as  $Z_{dr}$  and  $\phi_{dp}$  is directly affected by the magnitude of  $\rho_{hv}$ . Figure 5.17 (a) and Figure 5.17 (b) show the standard

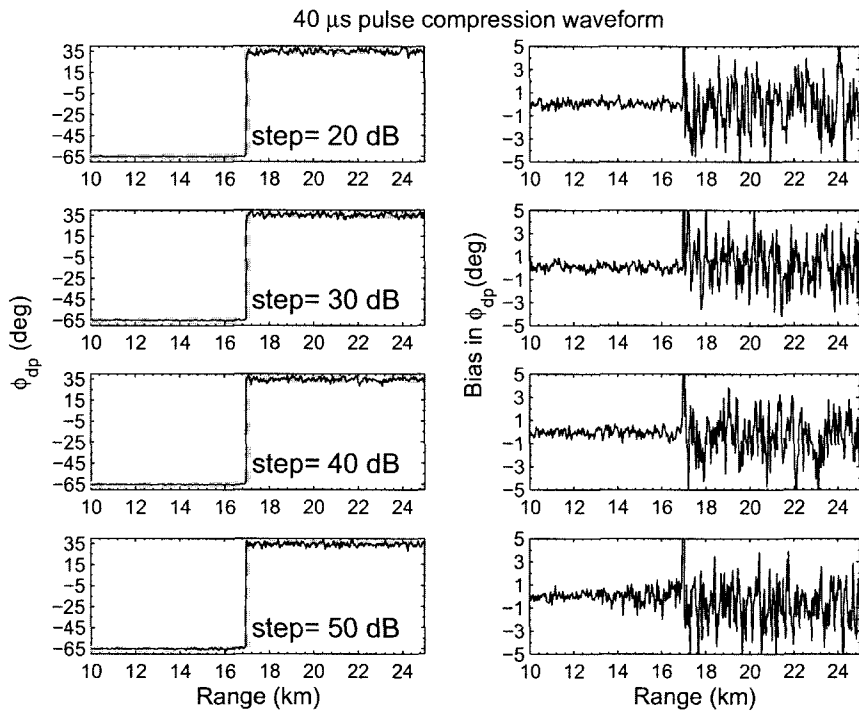


Figure 5.15: The impact of side lobe level on  $\phi_{dp}$  using a step function profile with varying step sizes of reflectivity with phase noise  $\delta\theta = 0.25^\circ$ .

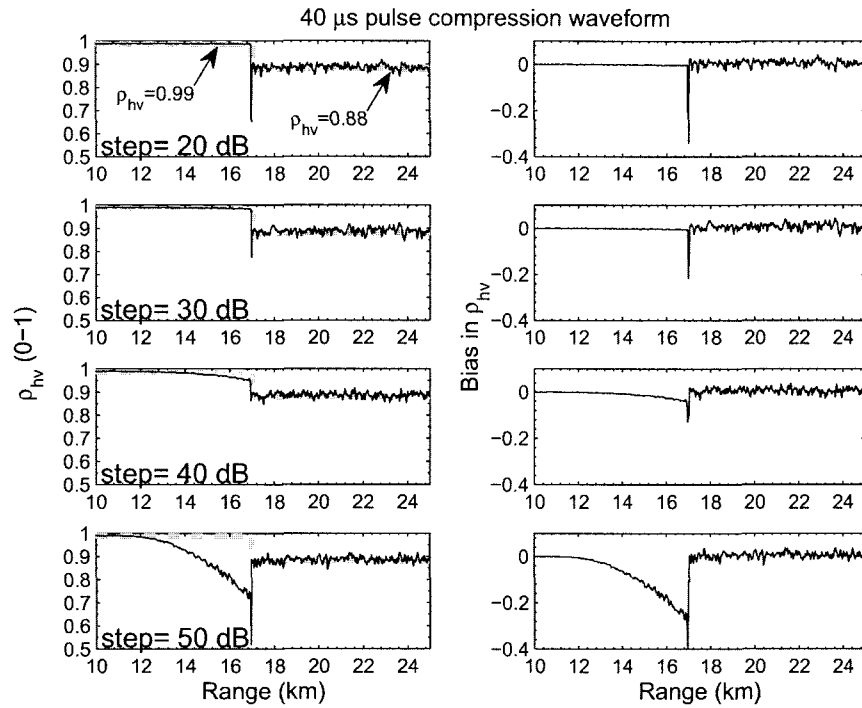


Figure 5.16: The impact of side lobe level on  $\rho_{hv}$  using a step function profile with varying step sizes of reflectivity with phase noise  $\delta\theta = 0.25^\circ$ .

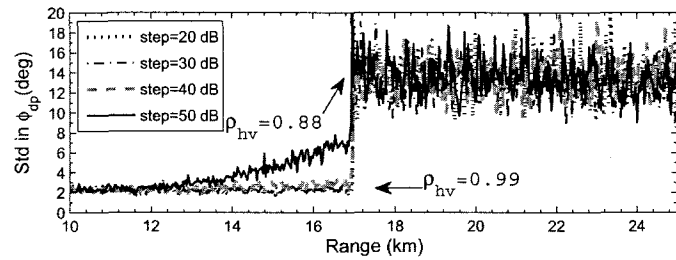
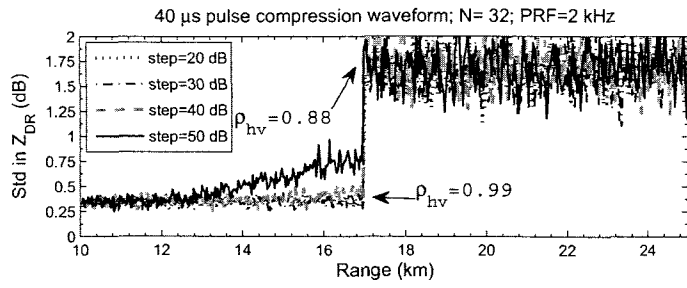
Table 5.2: Frequency diversity pulse compression waveform

Parameter	$i = 1$	$i = 2$	$i = 3$
Frequency	$f_1$	$f_2$	$f_3$
Pulse width, $\mu s$	40	20	1
Chirp bandwidth, MHz	3.6	3.6	-
Tukey window tuning	0.1268	0.1944	-
$k_T$	0.3543	0.3274	-
$k_B$	0.6	0.4920	-

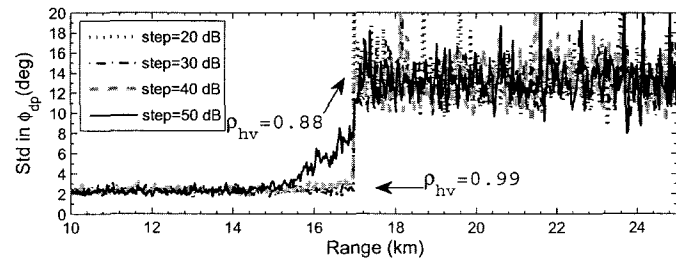
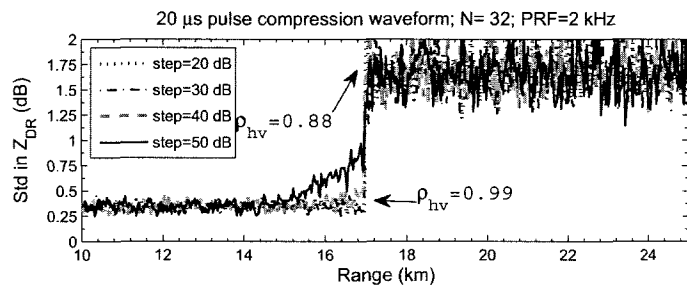
deviation of  $Z_{dr}$  and  $\phi_{dp}$  observed using the pulse compression waveform with  $T = 40 \mu s$  and  $T = 20 \mu s$  respectively and estimated using  $N = 32$  pulses at X-band. The standard deviations are plotted for varying reflectivity step sizes. For both the pulses, the standard deviation of  $Z_{dr}$  about 0.3 dB for  $Z_h$  step size up to 40 dB in the region where  $\rho_{hv} = 0.99$  and very high standard deviation of 1.75 dB corresponding to  $\rho_{hv} = 0.88$ . The standard deviations of polarimetric variables degrade significantly when  $\rho_{hv}$  is very low. It is important to observe the increased standard deviation of  $Z_{dr}$  due to range side lobe contamination when the  $Z_h$  step size is 50 dB. A behavior similar to  $Z_{dr}$  is observed in  $\phi_{dp}$ . However, the error in  $\phi_{dp}$  is not as significant as the error in  $Z_{dr}$ .

## 5.6 Frequency diversity waveform

Based on the requirement of 10 dBZ sensitivity at 40 km a frequency diversity waveform consisting of three components is obtained using the sensitivity mapped generalized waveform. The pulse widths of the three components are  $T_1 = 40 \mu s$ ,  $T_2 = 20 \mu s$  and  $T_3 = 1 \mu s$ . The pulse compression waveform for each component using pulse compression is obtained by minimizing the side-lobe for a  $B = 3.6 MHz$  chirp operating at a base band sampling frequency of  $f_s = 5 MHz$ . The minimum ISL filter is chosen as the compression filter. The use of frequency diversity enables the mitigation of blind range. The envelope of the transmit pulse and its time-frequency plot are shown in Fig.5.18. The parameters of the frequency diversity waveform is



(a)



(b)

Figure 5.17: The standard deviation of  $Z_{dr}$  and  $\phi_{dp}$  with the reflectivity step size as a parameters (a) for a waveform with  $T = 40\mu s$  and (b) for a waveform with  $T = 20\mu s$ .

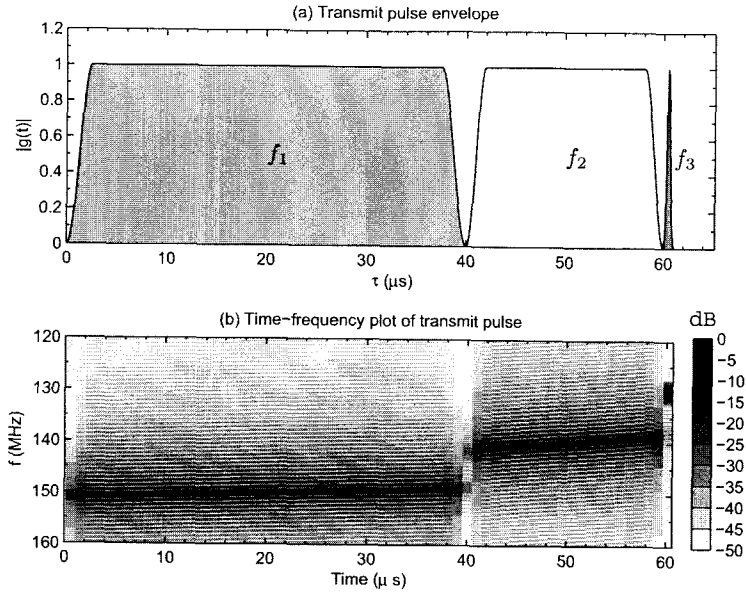


Figure 5.18: Time-frequency plot of the frequency diversity pulse compression waveform (a) Transmit pulse envelope (b) Time frequency plot.

shown in Table 5.2. The sub pulse at frequency  $f_1$  has a blind range of 9.15 km and has the highest sensitivity as shown in Fig. 5.1 while sub pulse at frequency  $f_2$  has a blind range of 3.15 km and has intermediate sensitivity. The short pulse at  $f_3$  does not have a blind range and has the least sensitivity. The measurements from the three frequencies are combined to provide observations without any blind range and adequate sensitivity.

In order to ascertain the feasibility of the frequency diversity pulse compression waveform in a more realistic meteorological phenomenon a simulation based on observations from CSU-CHILL radar is performed. A precipitation event with a well defined bright band was observed by CSU-CHILL radar on Jun 07, 2003 at 02:15:01 UTC. This bright band data set was used to simulate the received signal for a frequency diversity pulse compression waveform transmitted using a 100 W solid-state power amplifier. A phase noise of 0.5 degree was added to the transmit waveform. The simulations were performed with  $N = 64$  pulses at a PRF of 2 kHz. The cal-

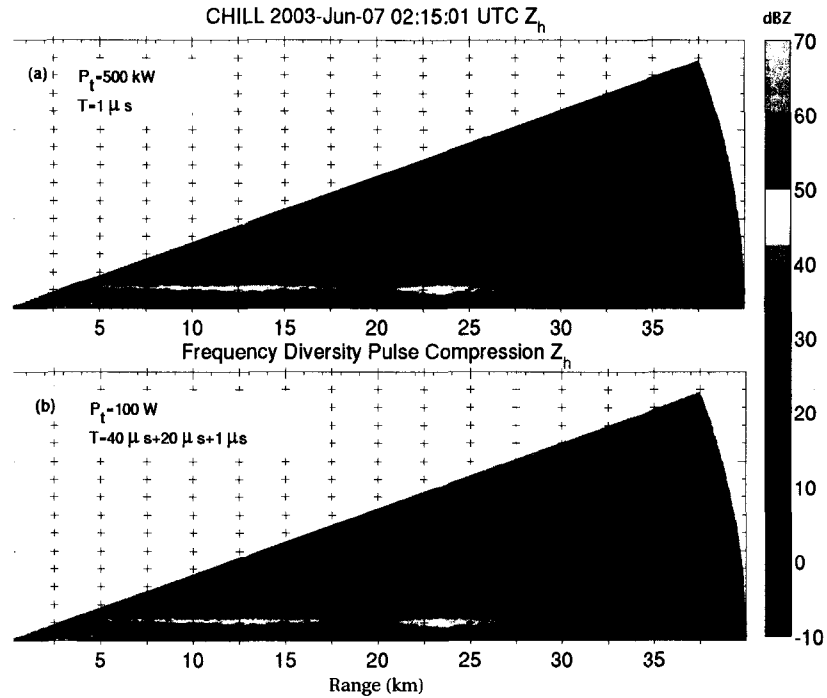


Figure 5.19: Simulation of frequency diversity pulse compression waveform for an X-band radar. (a) Observed reflectivity field from CSU-CHILL radar on Jun 07, 2003 at 02:15:01 UTC (b) The retrieved reflectivity from a frequency diversity pulse compression waveform.

ibration was done based on the radar constant for each component of the transmit waveform. The true bright band observations are shown in Fig. 5.19(a) which was obtained from a 500 kW peak-power radar. The reflectivity obtained by combining the observations from the three components of the transmit pulse is shown in Fig. 5.19(b). A comparison of the true reflectivity and that obtained from pulse compression agree well. The reflectivity observations with the solid state radar and true reflectivity deviate from each other at lower reflectivity regions seen well above the melting layer at farther ranges as shown in Fig. 5.19. This difference is primarily because CSU-CHILL uses a very high powered Klystron transmitter.

A performance of the frequency diversity pulse compression radar is evaluated based on simulations at X-band. The characteristics of the solid-state radar used in the simulations is shown in Table 5.3. Observations from the X-band polarimet-

Table 5.3: Solid-state radar characteristics used in simulations

<b>Transmitter</b>	
Type	Solid-state
Center frequency	$9400 \pm 100$ MHz
Peak power output	100 W (per polarization channel)
Pulse width	maximum $70 \mu s$
Polarization	Dual linear, Horizontal and Vertical
Max. Duty Cycle	15%
<b>Antenna and Pedestal</b>	
Type (diameter)	Parabolic reflector (2.4 m)
3-dB Beam width	$1^\circ$
Gain	43.0 dB
<b>Receiver</b>	
Type	Dual-channel digital
Bandwidth	5 MHz (before compression filter)
Noise figure	4.0 dB
Sampling rate	5 MHz (baseband)

ric radars deployed by Center for Collaborative Adaptive Sensing of the Atmosphere (CASA) is used as input data to simulate a more realistic distribution of precipitation and simulations were performed with  $N = 64$  pulses at a PRF of 2 kHz. The simulations are carried out at three different frequencies whose center frequencies are separated by 10 MHz. The parameters of the wideband waveform simulated is given in Table 5.2.

The observations made by the CASA radar at Chickasha on Mar 10, 2009 at 04:14:19 UTC and the results obtained with the frequency diversity pulse compression waveform is shown in Fig. 5.20 and 5.21. The precipitation event shown in Fig. 5.20 has weaker echoes close to the radar from azimuth of  $240^\circ$  to  $330^\circ$  and very strong reflectivities in the ranges covered by the longest pulse  $T_1 = 40 \mu s$  (azimuth  $330^\circ$  to  $20^\circ$ ). The results obtained for the frequency diversity pulse compression waveform are combined from the three frequencies such that there is no blind range in the data and there is spatial continuity along range. This is particularly necessary for  $\phi_{dp}$  because the system differential phase shift at the three different frequencies can lead to discontinuity in the range profiles of  $\phi_{dp}$ . The reflectivity observed with the

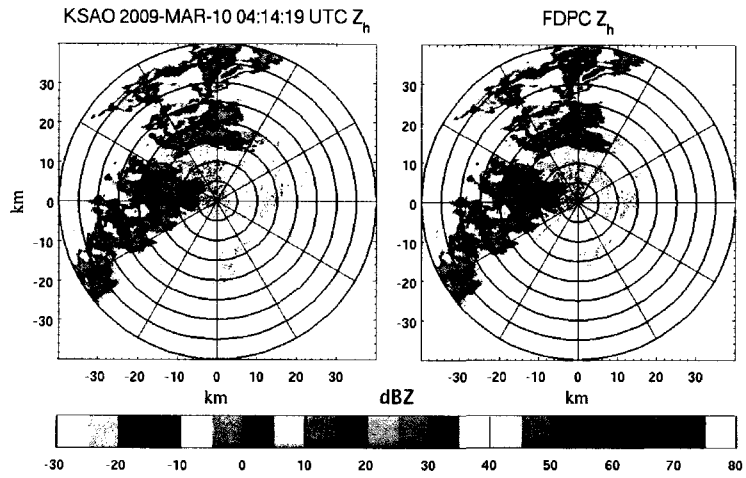
frequency diversity pulse compression is shown in Fig. 5.20(a) and it can be seen that they match very well with the input reflectivity. The reflectivity close to the radar is obtained from the short pulse while the weaker echoes farther away from the radar are obtained from the long pulses.

The observation of  $Z_{dr}$  from the frequency diversity pulse compression waveform is also in good agreement with the input  $Z_{dr}$  as shown in Fig. 5.20(b). The observed  $\phi_{dp}$  and  $\rho_{hv}$  from the frequency diversity pulse compression waveform is compared with the input  $\phi_{dp}$  and  $\rho_{hv}$  respectively and are shown in 5.21 (a) and (b) respectively. The increase in  $\phi_{dp}$  along range (which indicates attenuation) in areas of significant precipitation is in good agreement between the input  $\phi_{dp}$  distribution and the  $\phi_{dp}$  distribution obtained from the pulse compression waveform. The retrieval of  $\phi_{dp}$  is critical for attenuation correction algorithms. Similar simulation were carried out for a second data set based on observations made by the CASA radar at Cyril on Apr 16, 2009 at 23:14:17 UTC under identical set up. The simulation based on Cyril radars also provided results comparable to the Chickasha results.

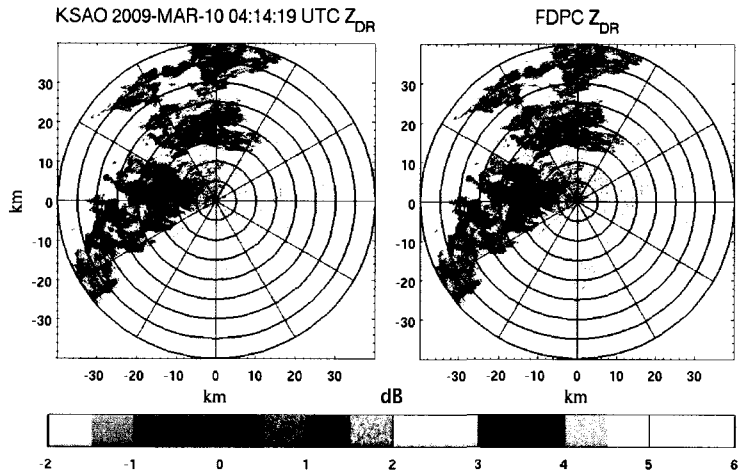
A scatter plot of reflectivity observed using frequency diversity pulse compression versus input reflectivity for the two simulation cases is shown in Fig. 5.22.

## 5.7 Summary

Waveforms for radar using solid-state transmitters are critically important for electronically scanned radars. The main drawback of the solid-state transmitter is the unavailability of high peak power which reduces the sensitivity. However, solid-state transmitter are capable of transmitting long pulses which is used to gain sensitivity. The transmission of long pulses does provide good sensitivity but at an expense of very poor range resolution. Pulse compression waveforms provides means to achieve good sensitivity by transmitting long pulse and still make observations with good range resolution. However, the transmission of long pulses blinds the radar for the

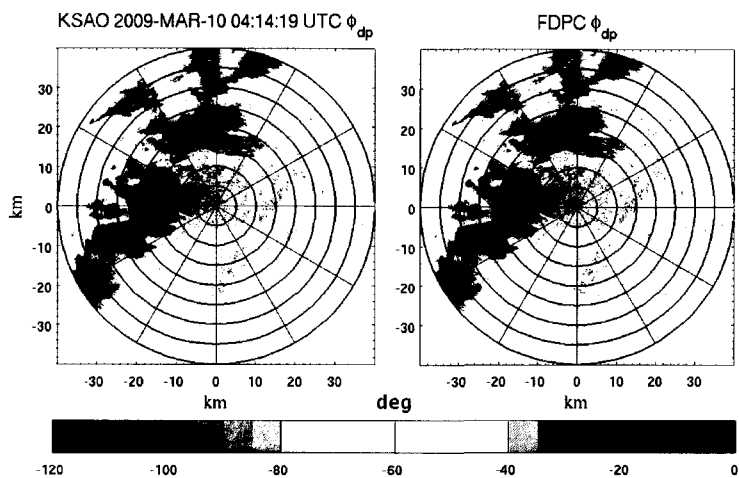


(a)

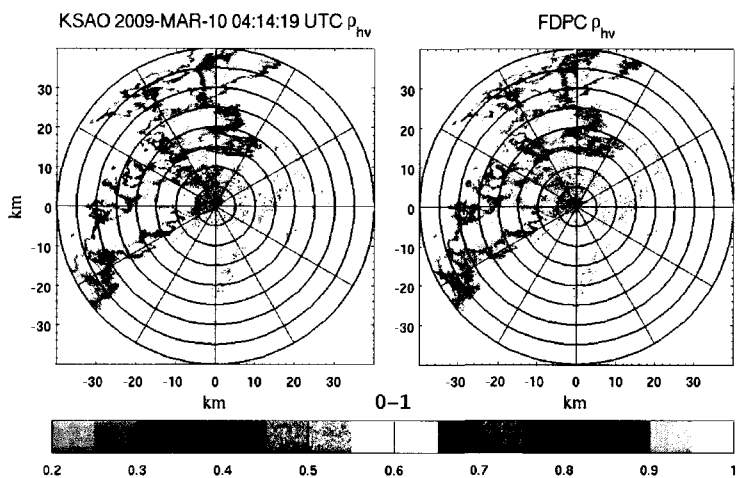


(b)

Figure 5.20: PPI plots of frequency diversity pulse compression waveform compared with the input data. The simulation is based on observation made with CASA IP1 radar at Chickasha on Mar 10, 2009 at 01:14:19 UTC. (a) Reflectivity (b)  $Z_{dr}$ .



(a)



(b)

Figure 5.21: PPI plots of frequency diversity pulse compression waveform compared with the input data. The simulation is based on observation made with CASA IP1 radar at Chickasha on Mar 10, 2009 at 01:14:19 UTC. (a)  $\phi_{dp}$  (b)  $\rho_{hv}$ .

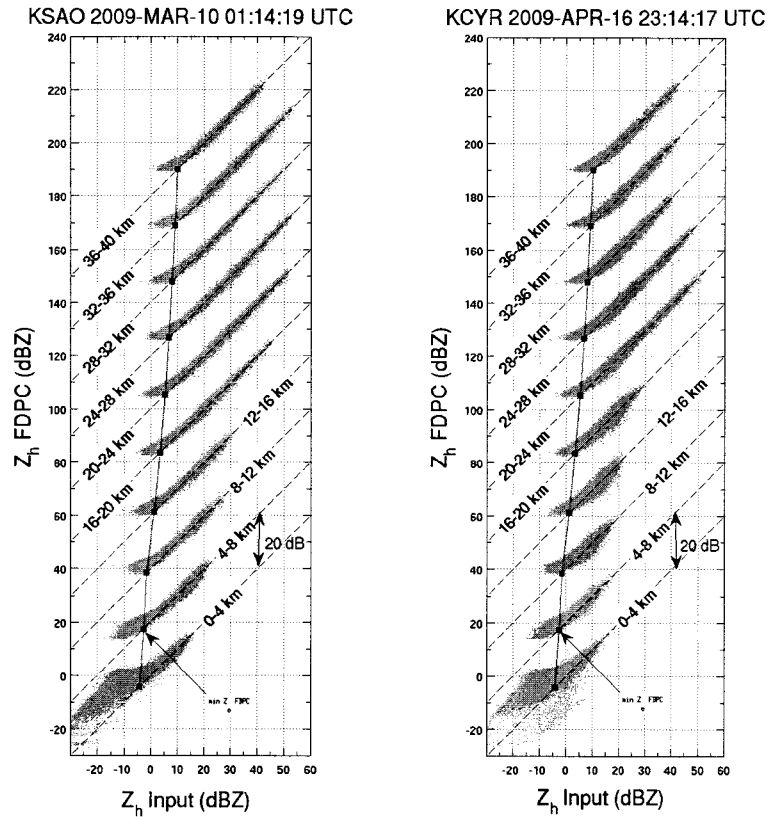


Figure 5.22: Scatter plot of reflectivity from frequency diversity pulse compression versus the input reflectivity. The data used for simulations were collected by Chickasha radar on Mar 10, 2009 at 01:14:19 UTC and Cyril radar on Apr 16, 2009 at 23:14:17 UTC.

duration of the pulse length resulting in blind ranges. A novel waveform using frequency diversity was presented to mitigate the problems of low sensitivity and blind ranges associated with pulse compression waveforms. A sensitivity mapped generalized waveform was presented that utilized wideband transmit signals along with frequency diversity. The use of frequency diversity long pulses is the key feature that mitigates blind ranges.

A nonlinear frequency modulation pulse compression waveforms was proposed for the long pulses to achieve good range resolution and side lobe levels. The nonlinear frequency modulation pulse compression waveform was parameterized in terms of a linear frequency chirp and a non-linear chirp segments. A quadratic time-frequency relation governs the non-linear frequency modulation. The pulse compression waveform is controlled by three parameters; the time and bandwidth control parameters and the Tukey envelope window parameter. A minimum ISL filter was designed to achieve very good side lobe performance. The minimum ISL filter is based on the transmit pulse and is designed such that the ambiguity function has minimal integrated side lobes. The side-lobe performance of pulse compression waveforms were presented for the minimum ISL filter. The Doppler tolerance and the impact of phase errors were quantified for integrated and peak side-lobe level. It is important to have phase errors less than 0.5 deg to minimize the range side-lobe problem. The performance of the minimum ISL filter degrades in the presence of Doppler velocity but the side lobe levels are still within acceptable limits for Doppler velocities encountered in meteorological phenomenons.

An analysis of the pulse compression waveform for volume targets was presented. The range resolution, receiver, impact on Doppler moments and polarimetric variables were presented. The minimum ISL filter provided better range resolution when compared to window based mismatch filters. The receiver bandwidth plays an important role in the amount of noise added and finite bandwidth loss in the receiver. The minimum ISL filter suffers less finite bandwidth loss when compared to window

based mismatch filters. The impact of strong reflectivity gradients and range side lobes were presented for volume targets. The paper presented the impact of range side lobes using step function with varying step sizes. The retrieval of Doppler moments and polarimetric variables were not significantly affected by a reflectivity step size up to 40 dB. The performance of the non-linear pulse compression waveform and the minimum ISL filter were acceptable for reflectivity step size up to 40 dB.

A frequency diversity pulse compression waveform was simulated based on actual observations from CSU-CHILL radar at S-band and the CASA IP1 radars at X-band. The CSU-CHILL radar observations are made with a very high power transmitter and therefore, has very high sensitivity. A comparison based of CSU-CHILL radar observations with the simulated X-band observation using frequency diversity pulse compression waveform was presented. The frequency diversity pulse compression waveform does provide adequate sensitivity and is suggested for operations. The performance of the frequency diversity pulse compression waveform based on observations from CASA's IP1 radars were presented. The errors in  $Z_h$ ,  $Z_{dr}$  and  $\phi_{dp}$  were described for varying reflectivity ranges. The biases and standard deviations are within acceptable limits. The frequency diversity pulse compression waveform provided acceptable performance in providing adequate sensitivity, minimizing range side lobes and mitigating blind range. Based on analysis performed on realistic simulations using CSU-CHILL radar data and CASA IP1 data the frequency diversity pulse compression waveform is suggested for polarimetric pulsed Doppler weather radars using solid-state transmitters.

CHAPTER 6  
NETWORKED WAVEFORM SYSTEM FOR WEATHER RADAR  
NETWORK

---

---

### 6.1 Introduction

A fundamental physical limit imposed by transmission from single radar is the problem of changing resolution as a function of range. In addition the lowest coverage altitude increases with range due to earth curvature. As an alternate solution, a networked radar environment concept has been proposed (Chandrasekar and Jayasumana (2001), McLaughlin (2002), Fig. 6.1). Single Doppler radar transmitting pulses with uniform pulse repetition frequency (PRF) have a fundamental limitation on maximum unambiguous range ( $r_a$ ) and maximum unambiguous velocity ( $v_a$ ) determined by the pulse repetition time and the wavelength. There is always a conflicting trade off between  $r_a$  and  $v_a$  as their product is fixed for a given wavelength. This trade off is more stringent for X-band radars due to the shorter wavelength. The first generation CASA (the Center for Collaborative Adaptive Sensing of the Atmosphere, an engineering research center established by the National Science Foundation) radars are low cost X-band magnetron radars. Hence, there is a hardware limitation to implement time and phase coded waveforms, which are the existing or proposed waveforms to mitigate range ambiguity on a single radar Bharadwaj et al. (2007).

In this chapter a new approach to mitigate ambiguity is presented. The new approach is a network based technique where spatially distributed mono-static radar are

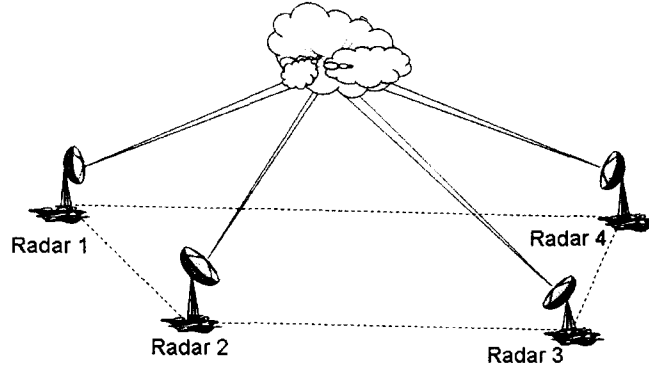


Figure 6.1: Illustration of a networked radar concept (NETRAD).

used to mitigate ambiguities in the measurements. In this chapter ambiguity problem is formulated for a networked radar environment by using the principle that the underlying intrinsic properties of the medium such as reflectivity and velocity must remain consistent in a networked environment. The ambiguity is resolved by jointly processing the measurements from all the individual radars. The short wavelength used in CASA radars limits the maximum unambiguous velocity and the inability of low cost transmitter to transmit complex waveforms amplifies the velocity ambiguity problem. A distributed waveform is proposed to overcome the ambiguity for targeted applications such as tornado detection, high winds, tracking and hydrology. A simulation study is carried out to evaluate the performance of the distributed waveform. In addition to the simulation study the network based approach is tested with measurements from the CASA's IP1(Integrative Projects) testbed. The CASA testbed consist of a network of four X-band radars deployed as shown in Fig.6.2. The four operational radars are deployed at Cyril, Chickasha, Rush Springs and Lawton in southern Oklahoma.

This chapter is organized as follows: A brief description of multiple Doppler measurements is presented in Section 6.2 which is essential for understanding of the formulation of the networked waveform system. Section 6.3 describes the formulation and analysis of the networked waveform system. A simulation study for the net-

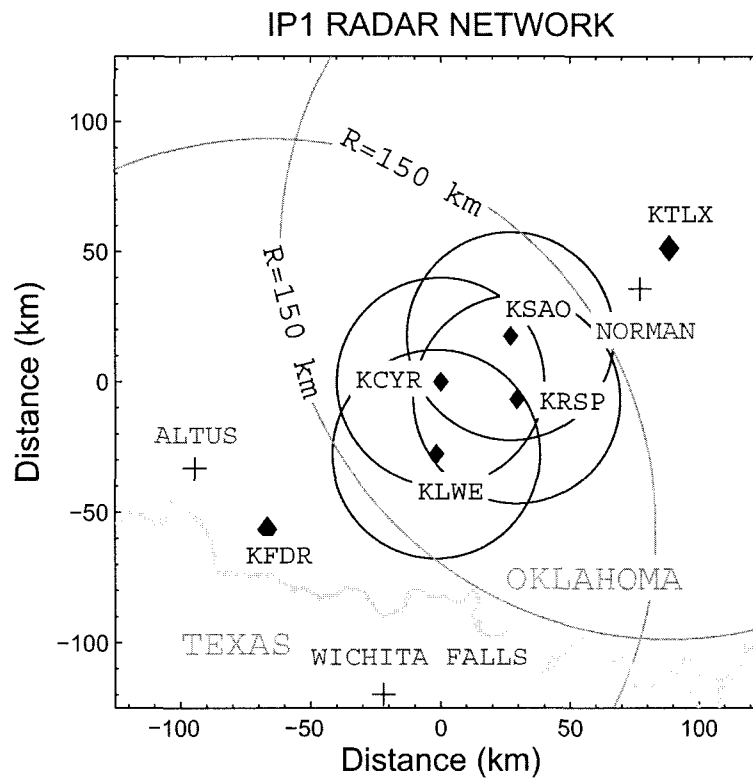


Figure 6.2: Geometry of IP1 radar network. The four radar nodes are located at Cyril(KCYR), Chickasha(KSAO), Rush Springs(KRSP) and Lawton(KLWE).

worked waveform is presented in Section 6.4 and results from actual implementation of the networked waveform on the CASA IP1 radar network is presented in Section 6.5. Finally, Section 6.6 presents the summary of the chapter.

## 6.2 Multiple Doppler observations

A single radars maps the component of wind speed directed in the radial direction of the radar. The mean Doppler velocity estimated from the received signal is a projection of the vector wind velocity on to the propagation path of the beam. For example, wind field perpendicular to the beam will result in zero mean Doppler velocity at the radar. The intrinsic wind velocity vector has three components; two components in the horizontal direction and one component in the vertical direction. The radial velocity of a resolution volume observable at the radar is related to the intrinsic wind velocity by the equation given by

$$v(a, e) = u \sin a \cos e + v \cos a \cos e + w \sin e, \quad (6.1)$$

where  $a$  and  $e$  are the azimuth and elevation of the resolution volume;  $u$ ,  $v$  and  $w$  are the three components of the intrinsic wind velocity vector. Two or more radars observations are required to obtain the unknown wind velocity vector. The relation between the observed radial velocities of a resolution volume and the intrinsic wind velocity components in a networked radar environment with  $N$  radars is given by

$$\mathbf{v} = \begin{pmatrix} v_1 \\ v_2 \\ \vdots \\ v_N \end{pmatrix} = \mathbf{G} \begin{pmatrix} u \\ v \\ w \end{pmatrix} + \begin{pmatrix} \varepsilon_1 \\ \varepsilon_2 \\ \vdots \\ \varepsilon_N \end{pmatrix}, \quad (6.2)$$

where  $\mathbf{G}$  is given by

$$\mathbf{G} = \begin{pmatrix} \sin a_1 \cos e_1 & \cos a_1 \cos e_1 & \sin e_1 \\ \sin a_2 \cos e_2 & \cos a_2 \cos e_2 & \sin e_2 \\ \vdots & \vdots & \vdots \\ \sin a_N \cos e_N & \cos a_N \cos e_N & \sin e_N \end{pmatrix} \quad (6.3)$$

The wind field can be estimated by solving the above overdetermined set of equations. However, the errors in the vertical velocity is very high because a low elevations the radar beam and the vertical component are nearly orthogonal. The mass continuity equation is used to in conjunction with the above overdetermined system of equations to obtain the wind vector. A detailed formulation of the multiple Doppler synthesis is described in Armijo (1969).

### 6.3 Networked Waveform System

Waveforms for precipitation radars have been designed from a single radar perspective for many decades. The primary parameters for a pulsing scheme are the number of pulses and the pulse repetition time (PRT) or pulse repetition frequency (PRF). The number of pulses used in the integration is mainly for the reduction of errors in the estimated moments. The PRT selection is based on the unambiguous range-velocity space and the operating range of Doppler spectral width. Both, unambiguous range-velocity space and operating range of Doppler spectral width are a function of PRT and the radar wavelength. Since the wavelength is fixed for a given radar or radar network only the PRT can be changed to alter the design space. The most common approach is the use of staggered PRT and multiple PRF pulsing schemes. In this section a networked waveform system is described that adds spatial diversity of individual radars along with PRT to mitigate the ambiguity problem. In a networked waveform measurements of precipitation from a network of weather radars are jointly processed to mitigate ambiguity.

#### 6.3.1 Formulation and solution

The networked waveform can be represented with

$$\mathbf{S}(t) = [s_1(t) \quad s_2(t) \quad s_3(t) \quad \cdots \quad s_N(t)] \quad (6.4)$$

where  $\mathbf{s}_j(t)$  is a vector representing the transmitted signal or pulsing scheme at the  $j^{\text{th}}$  radar node and  $\mathbf{s}_j(t)$  is given by

$$\mathbf{s}_j(t) = \begin{pmatrix} s_{j1}(t) \\ s_{j2}(t) \\ \vdots \\ s_{jM_j}(t) \end{pmatrix}, \quad (6.5)$$

where  $s_{jk}(t)$  for  $k = 1, 2, \dots, M_j$  is the pulsing scheme at the  $j^{\text{th}}$  radar node with multiple PRF waveform with  $M_j$  PRFs. The pulsing scheme  $s_{jk}(t)$  will operate at a pulse repetition time  $T_{jk}$  whose maximum unambiguous velocity is given by

$$v_{jk}^a = \frac{\lambda}{4T_{jk}}. \quad (6.6)$$

In general,  $M_j$  can be different in each radar node but in this research  $M_j = M$  is identical in each radar node. Therefore, a networked waveform provides a total of  $NM$  samples of the same atmospheric phenomenon but observed with  $N$  view points. The dimension of networked waveform system  $D$  is given by

$$D = \sum_{j=1}^N M_j = NM. \quad (6.7)$$

The precipitation medium within the coverage of the networked radar system is measured with the distributed waveform  $\mathbf{S}$ . The intrinsic properties of the precipitation medium should remain self consistent within measurements made with  $\mathbf{S}$ .

The mean Doppler velocity estimated using the networked waveform  $\mathbf{S}$  is related to the intrinsic wind field by a geometric transformation matrix. The mean Doppler velocity observed with  $\mathbf{S}$  is given by

$$\hat{\mathbf{v}}_m = \begin{pmatrix} \hat{v}_1 \\ \hat{v}_2 \\ \vdots \\ \hat{v}_M \end{pmatrix} = \mathbf{\Theta} \mathbf{w} + \boldsymbol{\epsilon}, \quad (6.8)$$

where

$$\hat{\mathbf{v}}_k = \begin{pmatrix} \hat{v}_{1k} \\ \hat{v}_{2k} \\ \vdots \\ \hat{v}_{Nk} \end{pmatrix}, \mathbf{w} = \begin{pmatrix} u \\ v \\ w \end{pmatrix} \text{ and } \mathbf{\Theta} = \begin{pmatrix} \mathbf{G} \\ \mathbf{G} \\ \vdots \\ \mathbf{G} \end{pmatrix}. \quad (6.9)$$

The observed velocities  $\hat{v}_{jk}$  may have aliased velocities whose folding or Nyquist velocity is  $v_{jk}^a$ . The folding of velocities occurs differently for each  $T_{jk}$  but the observations are of a the same resolution volume. Therefore, self consistency of the vector velocity field can be invoked in a networked environment to estimate the true wind field. The velocity ambiguities are resolved by directly estimating the wind fields. The solution is obtained by solving the optimization problem given by

$$\hat{\boldsymbol{w}} = \underset{\boldsymbol{w}}{\text{arg min}} \|\boldsymbol{\Theta}\boldsymbol{w} - \hat{\boldsymbol{v}}_m\|^2 \quad (6.10)$$

The estimated wind velocity vector can be used to obtain the unfolded radial velocities at each node as given below.

$$\hat{\boldsymbol{v}}_{un} = \boldsymbol{\Theta}\hat{\boldsymbol{w}} \quad (6.11)$$

The wind velocity vector  $\hat{\boldsymbol{w}}$  is used in multi-Doppler analysis for studying the kinematics within storms while  $\hat{\boldsymbol{v}}_{un}$  is used for detection of shear features that are associated with tornadoes.

### 6.3.2 Analysis

Before a a networked waveform is designed additional constraints on the operating PRTs is set based on both operational and hardware requirements. A maximum operating PRT  $T_m$  is first set so that the precipitation volume is adequately sampled to accommodate larger Doppler spectral widths. The minimum PRT  $T_{min}$  is set by the maximum duty cycle of the transmitter. Therefore, the PRT  $T_{jk}$  in the  $k^{th}$  burst at the  $j^{th}$  radar is limited to

$$T_m \geq T_{jk} \geq T_{min} \text{ for all } j = 1, 2, \dots, N \text{ and } k = 1, 2, \dots, M. \quad (6.12)$$

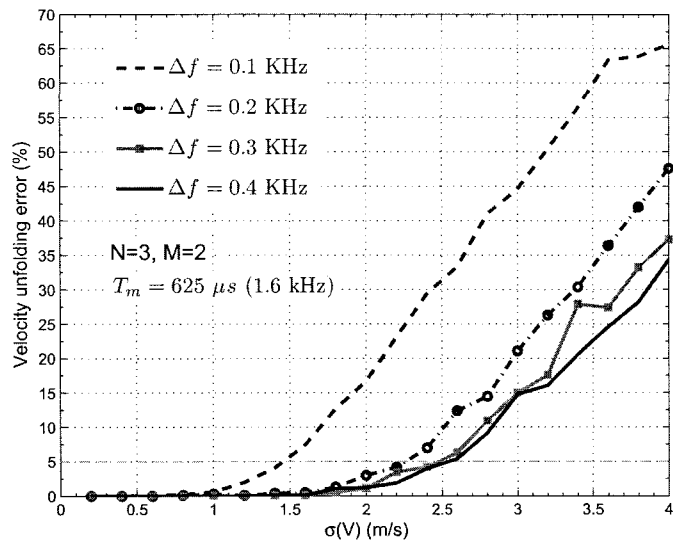
To simplify the design process a differential step in PRF  $\Delta f$  is used to obtain  $T_{jk}$  for the  $N$  radars.  $\Delta f$  can be in the range of 100 Hz to 500 Hz and  $T_m = 625 \mu s$  which

corresponds to a PRF of 1.6 kHz is chosen. The PRT at the  $N$  radar nodes is given by

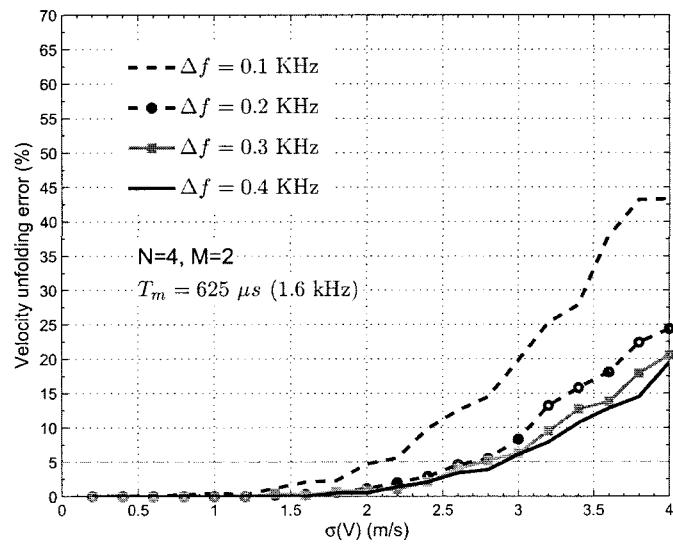
$$T_{jk} = \frac{T_m}{1 + [(k-1)N + j - 1] \Delta f T_m} \quad (6.13)$$

A simulation at X-band is performed to illustrate the design and performance of the networked waveform. The simulation is performed for a radar network with  $N = 3$  radars and  $M = 2$  burst at each radars. Essentially, each radar operates in a dual-PRF waveforms but it is important to note that unlike the traditional dual-PRF waveform there is no requirement on the ratio of the two PRFs. The geometry of the radar network is chosen to be identical to CASA's IP1 radar network. A random location within the coverage region of the three radars is selected and a wind field with a uniform distribution of  $u \sim U(-50, 50)$  and  $v \sim U(-50, 50)$  is simulated. The observed radial velocities are computed based on the intrinsic wind velocity vector and a Gaussian Measurement error with standard deviation  $\sigma(V)$  is added to the observed radial velocity. The unfolding error in wind velocity is estimated by comparing the intrinsic wind velocity with the velocity estimated from the networked waveform.

The unfolding error as a function of measurement error is shown in Fig. 6.3 for varying  $\Delta f$ . The unfolding error in Fig. 6.3 is shown for  $\Delta f = 100, 200, 300,$  and  $400$  Hz. The errors are plotted for two networked radar configurations; one with  $N = 3$  radar nodes and the other with  $N = 4$  radar nodes. The unfolding errors for  $N = 3$  radars and  $N = 4$  radars are shown in Fig. 6.3(a) and Fig. 6.3(b) respectively. It can be observed in Fig. 6.3 that the unfolding errors reduce when  $\Delta f$  is increased from 100 Hz to 400 Hz. The trend of lower velocity unfolding error with increasing  $\Delta f$  is consistent for  $N = 3$  and  $N = 4$  radars. It is worth noting that there is not much gain for  $\Delta f > 200 Hz$  which indicates that the improvement in the measurements due to PRF separation within the networked waveforms becomes asymptotic with  $\Delta f$ . There is a reduction in the velocity unfolding error when the number of radars is increased from  $N = 3$  to  $N = 4$ . The velocity unfolding error is under 2.5% for



(a)



(b)

Figure 6.3: Velocity unfolding error plotted as a function of standard deviation in velocity: (a) For  $N=3$  radars;(b) For  $N=4$  radars

$\sigma(V) \leq 2.0 \text{ m/s}$  for  $N = 3$  radars while velocity unfolding error is under 2.5% for  $\sigma(V) \leq 2.5 \text{ m/s}$  for  $N = 4$  radars indicating that more errors can be tolerated when the dimension of the networked waveform  $D$  is increased. The dimension  $D$  can be increased by adding more radars in the network or by adding more number of bursts  $M$  at each radar. It is an easier solution to increase the number of bursts at each radar than to add more radars within the network.

#### 6.4 Simulation Study

The velocity unfolding error is governed by the wind velocity vector and the distributed waveform design. The Doppler velocities measured at the nodes are directly a function of the wind speed and the wind direction at the specific resolution volume. Figure 6.4 shows the velocity unfolding error as a function of wind speed and wind direction for a specific resolution volume in the middle of the three nodes of the IP1 network. A significantly high variance of  $1 \text{ m/s}$  was used for the velocity error distribution. The region with very high velocity unfolding error in Fig.6.4 occurs in conditions when the radial velocities at the nodes are closer to the Nyquist velocities of the waveform. However, the region with high errors are much smaller than the region where the error is 5% or less and the overall velocity unfolding error is 3.5%. This limitation can be reduced by performing spatial filtering on the estimated wind field. Also, the the region with higher errors is reduced when a narrower error distribution is used. Figure 6.4 is the velocity unfolding error for a given resolution volume withing the IP1 network. An average error is obtained for the resolution volume for varying wind speeds and wind directions. The average unfolding error is a function of the location of the resolution volume within the radar network. Figure 6.5(a) shows the the average unfolding error for a networked waveform using three radar nodes. It can be observed in Fig.6.5 that the errors along the baseline of the radars is high. In order to eliminate the high errors in the baseline region a networked waveform with four radar nodes is implemented. It can be observed in Fig. 6.5(b) that the base

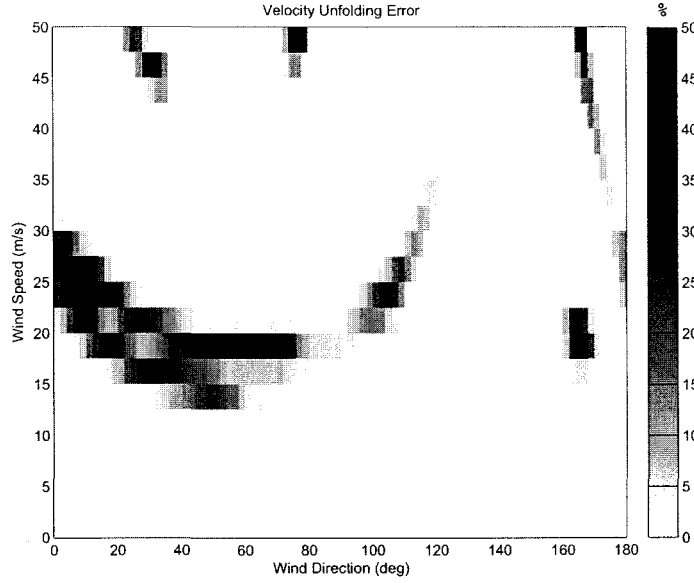


Figure 6.4: Velocity unfolding error as a function of wind speed and wind direction for the resolution volume located 20 km from Cyril radar at an azimuth of 60 deg.

error between Cyril and Rush Springs is eliminated. Therefore, in a large and dense network of radar the higher error in the baseline can be eliminated using a networked waveform system.

A simulation is performed to analyze the ability of the networked waveform system to measure very high Doppler velocities. A Rankine model (Wood and Brown, 1992) is used to model the horizontal wind fields within a tornado and is used to simulate the velocity distributions that are measured in the networked environment. The Doppler velocity measured at the radar node is given by

$$\begin{aligned}
 v_d = & \left( \frac{r}{r_c} \right)^{\xi-1} \left[ \frac{r_p}{r_c} - \frac{r_v}{r_c} \cos(\theta_p - \theta_v) \right] v_r \\
 & + \left( \frac{r}{r_c} \right)^{\xi-1} \frac{r_v}{r_c} \sin(\theta_p - \theta_v) v_t
 \end{aligned} \tag{6.14}$$

where  $v_r$  is the peak radial velocity and  $v_t$  is the peak tangential velocity at the center of vortex of radius  $r_c$ .  $r_p$  and  $r_v$  are the radar range of the resolution volume and vortex center respectively.  $\theta_p$  and  $\theta_v$  are the azimuth angles of the resolution volume

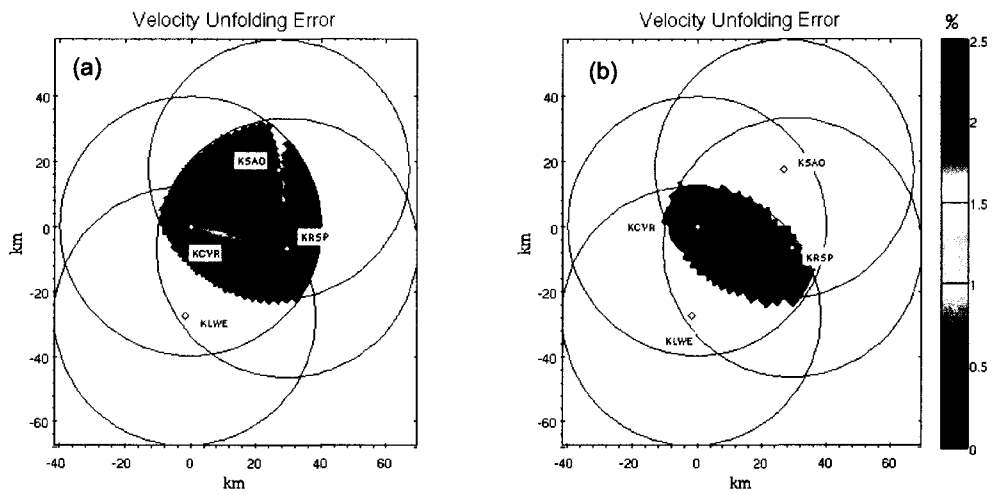


Figure 6.5: Velocity unfolding error within the IP1 coverage area. (a) Mean unfolding error with a networked waveform using three radar nodes. (b) Mean unfolding error with networked waveform using four radar nodes.

and vortex center respectively; and  $r$  is the distance of the resolution volume from the center of vortex. For the simulations presented in this chapter  $\xi = 1$  for  $r \leq r_c$  and  $\xi = -1$  for  $r > r_c$ .

A range profile of Doppler velocity is simulated based on (6.14) with a variance of 1 m/s in a networked radar environment with measurements made with  $\mathbf{U}$ . It can be observed in Fig.6.6(a) that unbiased velocities as high as 60 m/s can be measured with acceptable standard deviations as shown in Fig.6.6(b). The standard deviation of NETRAD retrieval is less than 1.5 m/s. Figure 6.6(c) shows the unfolding error with NETRAD retrieval at Cyril. The unfolding error is less than 5% while being able to measure velocities as high as 60 m/s. It is important to note that  $\mathbf{U}$  for the results shown in Fig.6.6 is designed for low cost hardware and in general  $\mathbf{U}$  can be designed to measure velocities as high as  $\pm 100$  m/s. Figure 6.7 shows Doppler velocity measurements of a tornado circulation simulated in the IP1 region. Figure 6.7(a) and (b) are measurements with the node waveform at Cyril and Fig. 6.7(c) shows the true Doppler velocity at Cyril. The networked waveform retrieval is shown in Fig. 6.7(d) and it can be observed that the networked retrieval is able to measure high velocities around  $\pm 60$  m/s.

## 6.5 Results

The networked waveform system was implemented in the IP1 radar network which consist of low cost X-band radars (Junyent et al. (2005)). A data set with the three nodes at Cyril, Chickasha and Rush Springs was collected on Mar 31, 2008 at 17:50:32 UTC. Figure 6.8 shows the networked retrieval for Cyril radar. The maximum unambiguous velocity at Cyril is 14.6 m/s. The Doppler velocity and reflectivity are plotted versus azimuth in Fig.6.8. Velocity folding can easily observed in the measured velocity while the NETRAD retrieval provides unfolded velocities. Figure 6.9 shows a PPI of networked retrieval for Cyril radar. The measured Doppler velocities are shown in Fig.6.9(a) and Fig.6.9(b). Velocity folding can easily be observed in the

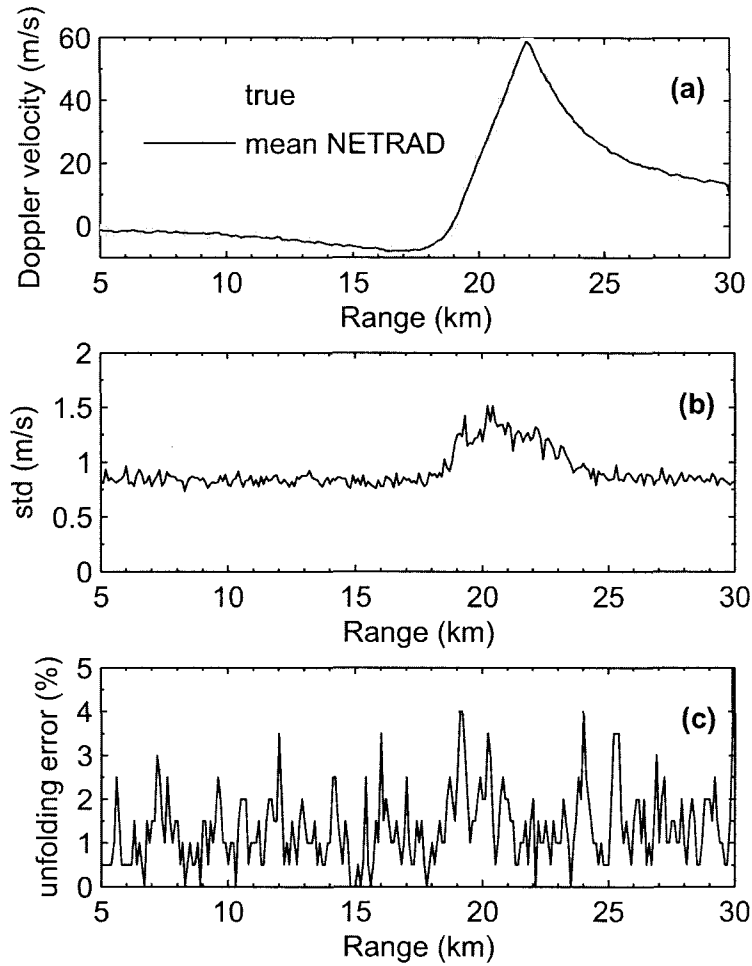


Figure 6.6: Networked waveform simulation with the IP1 radar network at 1 degree elevation angle. (a) True and mean Doppler velocity with networked retrieval (b) Standard deviation of NETRAD velocity at Cyril (c) Unfolding error in NETRAD velocity at Cyril.

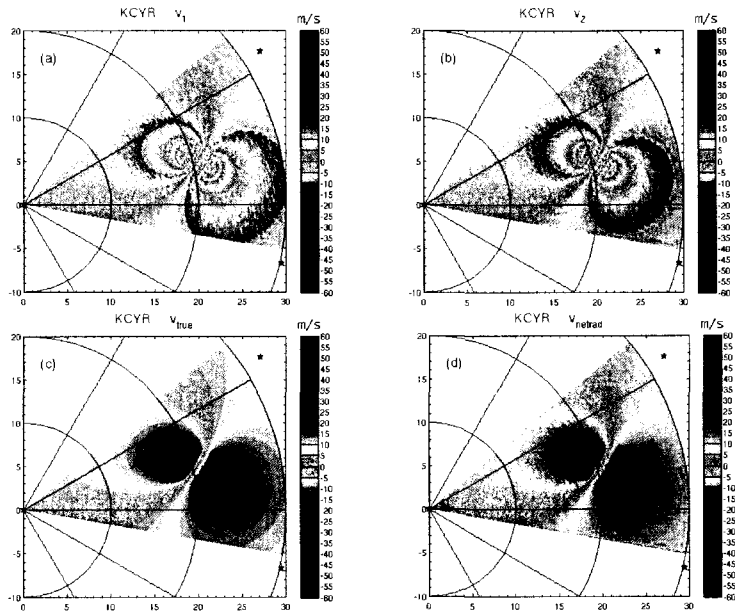


Figure 6.7: Networked waveform simulation with the IP1 radar network at 1 degree elevation angle. (a) Measured velocity at Cyril at PRF=1.6 kHz (b) Measured velocity at Cyril at PRF=1.84 kHz (c) True Doppler velocity of the simulated circulation and (d) (b) Networked retrieval for Cyril.

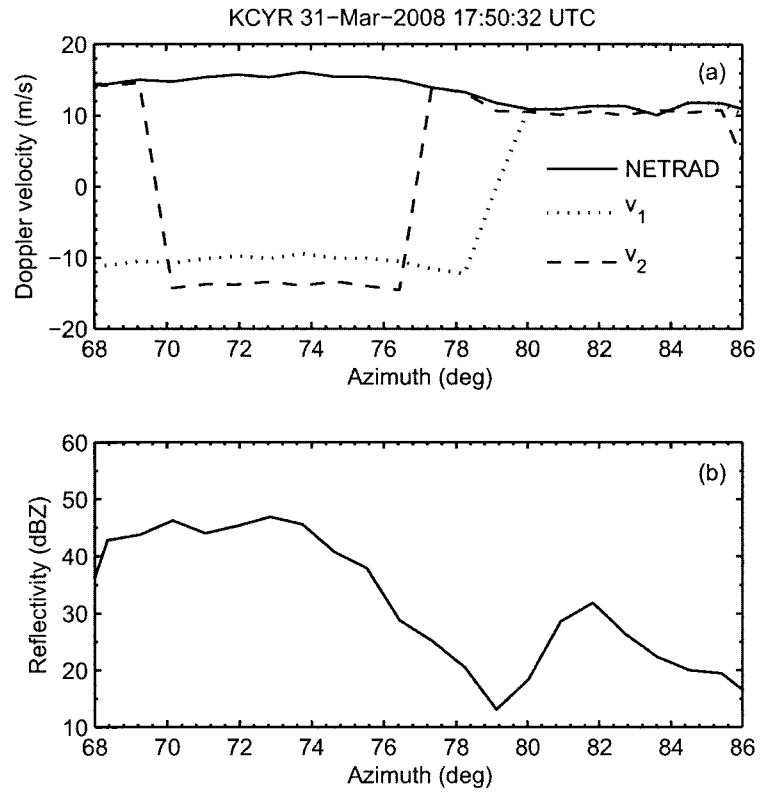


Figure 6.8: Networked waveform the IP1 radar network at 1 degree elevation angle. (a) Doppler velocity with networked retrieval (b) Reflectivity.

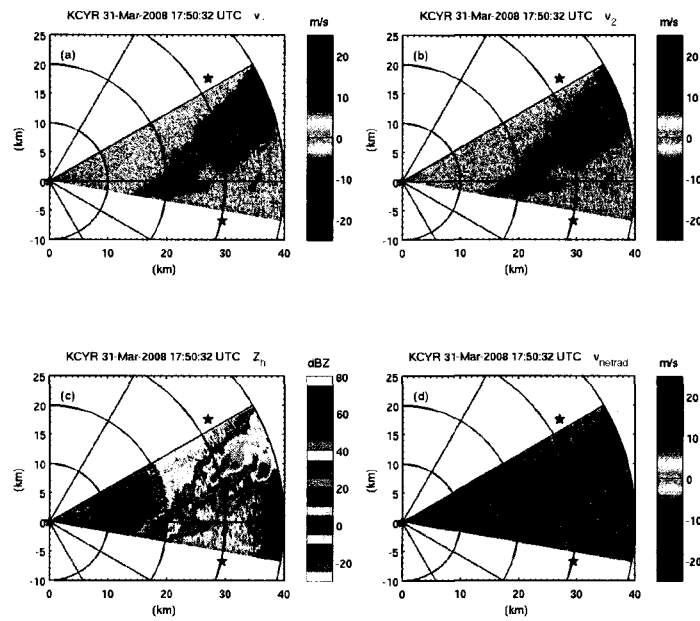


Figure 6.9: Networked waveform data collected on Mar 31, 2008 at 17:50:32 UTC with the IP1 radar network at 1 degree elevation angle. (a) Measured velocity at Cyril at PRF=1.6 kHz (b) Measured velocity at Cyril at PRF=1.84 kHz (c) Measured reflectivity and (d) (b) Networked retrieval for Cyril.

measured velocities. The measured reflectivity is shown in Fig.6.9(c) and Fig.6.9(d) shows the NETRAD retrieval of velocity for Cyril. It can be observed for regions with adequate signal-to-noise ratio NETRAD retrieval provides dealiased velocities. Although the Doppler velocities are not very high the application of the networked waveform system is demonstrated with data collected from an operational weather radar network.

## 6.6 Summary

A networked waveform system for resolving ambiguities for Doppler weather radar systems was presented. The networked waveform system offers many advantages. Firstly, it decouples the range ambiguity and velocity ambiguity from each other, whereas range and velocity ambiguities are coupled together in a single node waveform. Secondly, the networked waveform can be designed to measure very high velocities without the need for complex waveforms and advanced processing at each node. This minimizes the computational load on each node. A simple methodology was presented to simplify the designing of networked waveform system and an analysis of the errors in unfolding Doppler velocity was presented. The networked waveform system was parameterized in terms of the difference between the PRFs transmitted at each node. The velocity unfolding error reduced when the difference between the PRFs was increased but the improvement in performance was asymptotic with the PRF difference. Velocity unfolding errors of less than 5% was achieved based on simulations. The simulations were performed based on the network geometry of CASA IP1 radar network. Simulation of a circulation feature was used to ascertain the performance of the networked waveform in a realistic weather phenomenon. Based on the results obtained from simulation and it can be concluded that networked waveform system can provide high unambiguous velocities. The networked waveform system was implemented with the IP1 radar network and preliminary results show that the networked

approach is a viable solution. However, further evaluation based on data from the IP1 networked is necessary for operational use of networked waveform system.

# CHAPTER 7

## RESOLUTION ENHANCEMENT SYSTEM FOR NETWORKED RADAR SYSTEMS

---

---

### 7.1 Introduction

The spatial resolution of observations made with a pulsed Doppler weather radars has a direct impact on the detection, quantitative estimation and modeling of precipitating phenomenon. The spatial resolution of a pulse Doppler radar is determined by the size of the beam at a given range from the radar. The size of the beam along range is determined by the transmitted pulse width and the cross-range beam size is determined by the antenna beam width. The intrinsic property of the radar beam is that beam gets wider at farther ranges and thereby reduces the cross-beam resolution of precipitation measurements at far ranges. Improved spatial resolution enables us to observe finer structures in atmospheric phenomenon which improves detection and in general improves the understanding of atmospheric dynamics. Making observations at a wide range of spatial scales is not only important for improved detection and precipitation estimation but also very important for modeling applications. The study of precipitation variability in hydrological applications have suggested that small-scale spatial variability of the precipitation field has significant effect on runoff volume, which is provided as input to a rainfall-runoff model (Winchell et al., 1998).

The resolution along range can be improved by transmitting shorter pulses. A typical  $1 \mu s$  pulse will provide a range resolution of 150 m. Pulse compression waveforms

(Mudukutore et al., 1998) can be used to improve range resolution. Other techniques using deconvolution methods have been suggested to improve range resolution (Galati et al., 1996; Yu et al., 2006) and a technique using interferometry has been proposed (Zhang et al., 2005). The resolution obtained along range in current pulsed Doppler weather radar is on the order of 100 m and is within acceptable limits. However, the cross-range resolution is a function of antenna size and its impractical to have a physically very large aperture antenna. Therefore, the spatial resolution of a pulsed Doppler weather radar is limited by the antenna beam width. In this paper a novel methodology to improve the spatial resolution is presented.

A networked radar environment concept was proposed by Chandrasekar and Jayasumana (2001); McLaughlin (2002) to mitigate the many of the limitations of single radar using a large antenna. Chandrasekar and Lim (2008) used the concept of different view angles in a networked radar environment to perform attenuation correction. In this paper we use the concept of different view angles in a networked radar environment to enhance the spatial resolution of reflectivity. The novel methodology called the resolution enhancement system (RES) uses an algebraic approach to retrieve the reflectivity distribution with a constraint that all the radar nodes within the common coverage area observe a common reflectivity distribution.

The paper is organized as follows: Section 7.2 gives a short description of the received signal back-scattered from precipitation medium. Section 7.3 describes the relation between spatial resolution of the measurements and the radar system parameters. The evaluation of the methodology based on simulation study is presented in Section 7.4 while results from the application of the methodology on the data collected with Center for Collaborative Adaptive Sensing of the Atmosphere (CASA) Integrated Project I (IP1) radar network is presented in Section 7.5.

## 7.2 Received signal from volume targets

A pulse Doppler radar transmits a pulse train with a pulse repetition time (PRT)  $T_s$ . The received voltage from a resolution volume at range  $r$  corresponds to the back-scattered signal from particles within a volume extending radially from  $r$  to  $r + \Delta r$ , as illustrated in Fig.7.1. The back-scattered signals from all the particles within a single resolution volume sum to a resultant voltage sample at the receiver at time  $t$  (range,  $r$ ) and is given by

$$v_r(t) = \sum_k a_k(\tau_k; t) e^{-j2\pi f_0 \tau_k} g(t - \tau_k) \quad (7.1)$$

where  $a_k$  is the scattering amplitude of the  $k^{th}$  particle in the resolution volume.  $g(t)$  is the complex envelope of the transmit pulse operating at a frequency  $f_0$  and  $\tau_k = 2r_k/c$  where  $c$  is the speed of light. A more detailed description of the properties of the received voltage can be found in Bringi and Chandrasekar (2001). The mean power received from the resolution volume is given by

$$\bar{P}_r(t) = \langle |v_r(t)|^2 \rangle = \sum_k \langle |a_k(\tau_k; t)|^2 \rangle |g(t - \tau_k)|^2 \quad (7.2)$$

$$= \frac{\lambda^2 P_t}{(4\pi)^3} \sum_k \left\langle \frac{G_k^2 4\pi |S_k|^2}{r_k^4} \right\rangle |g(t - \tau_k)|^2 \quad (7.3)$$

where  $\langle \cdot \rangle$  indicates ensemble averaging and the time-dependence of  $a_k(\tau_k; t)$  is not considered because it is reasonable to assume that  $a_k(\tau_k; t)$  is stationary over the integration cycle.  $G_k$  is the antenna gain in the direction of the  $k^{th}$  particle. The mean radar cross-section per unit volume,  $\eta(r, \theta, \phi)$ , is defined by

$$\eta(r, \theta, \phi) \Delta V = \sum_k \langle 4\pi |S_k|^2 \rangle \quad (7.4)$$

where  $\Delta V$  is the elemental volume. The mean received power from range  $r_0$  can be expressed as an integrals of weighted  $\eta(r, \theta, \phi)$  over the resolution volume of the beam

$$\bar{P}_r(t) = \frac{\lambda^2 P_t}{(4\pi)^3} \int_V \frac{G^2(\theta, \phi)}{r^4} \eta(r, \theta, \phi) |g(t - \tau)|^2 dV \quad (7.5)$$

$$= \frac{\lambda^2 P_t}{(4\pi)^3} \int_{\Omega} \int_{r_0 + \Delta r/2}^{r_0 - \Delta r/2} \frac{G^2(\theta, \phi)}{r^2} \eta(r, \theta, \phi) |g(t - \tau)|^2 dr d\Omega \quad (7.6)$$

Where  $G(\theta, \phi)$  is the two-way antenna power pattern and  $\Omega$  is the elemental solid angle subtended by the resolution volume. The antenna power pattern is expressed

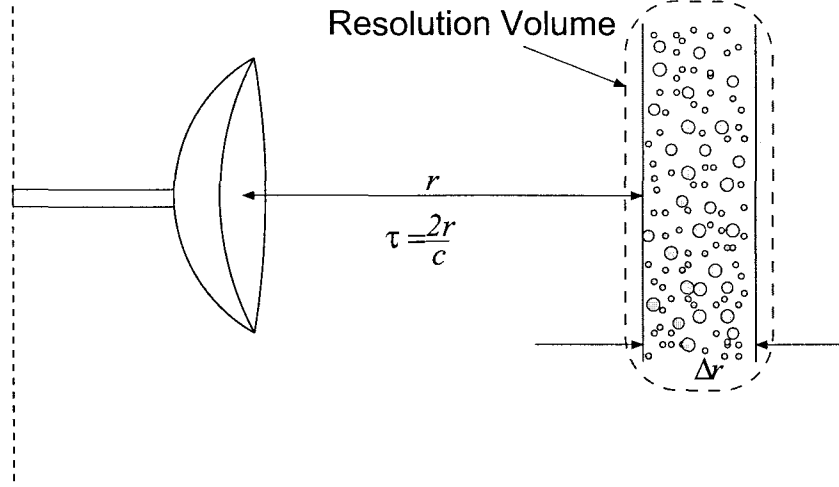


Figure 7.1: Received voltage due to scattering from particles located within a shell extending from  $(r, r + \Delta r)$ .

in terms of peak power pattern  $G_0$  and normalized power pattern  $f(\theta, \phi)$  as  $G(\theta, \phi) = G_0 f(\theta, \phi)$ . Then the mean received signal is given by

$$\bar{P}_r(t) = \frac{\lambda^2 P_t G_0^2}{(4\pi)^3} \int_{\Omega} \int_{r_0 + \Delta r/2}^{r_0 - \Delta r/2} \frac{f^2(\theta, \phi)}{r^2} \eta(r, \theta, \phi) |g(t - \tau)|^2 dr d\Omega \quad (7.7)$$

### 7.3 Resolution of measured reflectivity

The resolution of measured reflectivity is a function of the antenna beam-width, scan speed and the transmitted pulse width. The resolution along range is a function of the transmit pulse length and the cross-range or azimuthal resolution is a function of the beam width and the range to the resolution volumes shown in Fig.7.2. The range resolution is related to the pulse width  $T_0$  as

$$\Delta r = \frac{cT_0}{2} \quad (7.8)$$

If we assume the reflectivity is uniform along range within  $\Delta r$  and the complex envelope of the transmit pulse is rectangular then we can rewrite (7.7) as

$$\bar{P}_r(r_0) = \frac{cT_0}{2} \left[ \frac{\lambda^2 P_t G_0^2}{(4\pi)^3 r_0^2} \right] \int \int f^2(\theta, \phi) \eta(r_0, \theta, \phi) d\theta d\phi \quad (7.9)$$

Doppler weather radar have good range resolution due to the short transmit pulse width. Typically range resolution is from 50-200 m. However, the azimuthal resolution degrades as the range increases and is given by

$$\Delta R_{cx} = r\theta_B \quad (7.10)$$

where  $\theta_B$  (or  $\phi_B$ ) is the antenna beam-width. We can further decompose the antenna

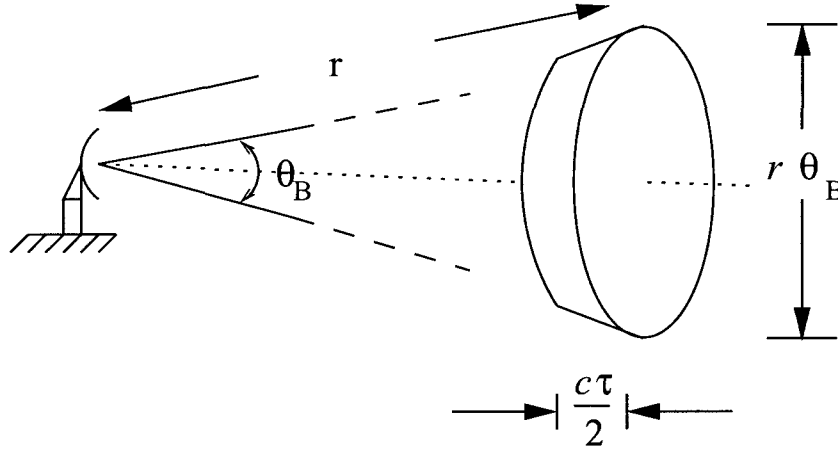


Figure 7.2: Illustration of resolution volume size as a function of pulse width, range and beam width.

pattern into two orthogonal components. One components defines the pattern in elevation and the other defines the pattern in azimuth. The antenna pattern can now be expressed as  $f(\theta, \phi) = g(\theta)g(\phi)$ . Doppler weather radars traditionally scan in the azimuth domain and if we lump the reflectivity integrated over the elevation angle  $\phi_0$  as  $\eta(r_0, \theta, \phi_0)$  then (7.9) can be written as

$$\bar{P}_r(r_0) = \frac{cT_0}{2} \left[ \frac{\lambda^2 P_t G_0^2}{(4\pi)^3 r_0^2} \right] \int g^2(\theta) \eta(r_0, \theta, \phi_0) d\theta \quad (7.11)$$

In addition to the range dependent beam broadening in (7.10) antenna motion during the integration cycle also effectively broadens the beam. The effective antenna pattern is given by

$$f_e = g^2 * w = \int_{-\infty}^{\infty} g^2(\theta - \xi) w(\xi) d\xi \quad (7.12)$$

where

$$g(\theta) = \exp\left\{-4\ln(2)\frac{\theta^2}{\theta_B^2}\right\} \quad (7.13)$$

and

$$w = \begin{cases} 1 & |\theta| \leq \Delta \\ 0 & \text{otherwise} \end{cases} \quad (7.14)$$

In (7.12)  $g(\theta)$  is the intrinsic antenna pattern in azimuth and  $w$  is the rectangular window function extending  $\Delta$  in azimuth. The length of  $w$  depends on the dwell time of the integration cycle. The effective antenna pattern is given by

$$f_e(\theta) = \frac{\theta_B}{4} \sqrt{\frac{\pi}{2\ln 2}} \left\{ \operatorname{erf}\left[\frac{\sqrt{8\ln 2}}{\theta_B}\left(\theta_B + \frac{\Delta}{2}\right)\right] - \operatorname{erf}\left[\frac{\sqrt{8\ln 2}}{\theta_B}\left(\theta_B - \frac{\Delta}{2}\right)\right] \right\} \quad (7.15)$$

The effective antenna pattern forms a range-variant kernel relating the reflectivity and

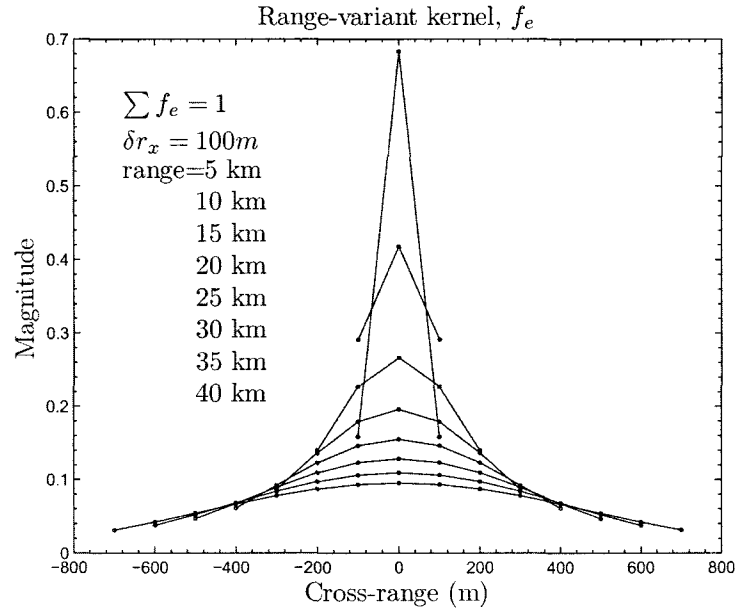


Figure 7.3: Range-variant discrete Gaussian kernel

the mean received power. The range-variant kernel is shown in Fig.7.3 as a function of cross-range distance with the range to the resolution volume as a parameters. It can be seen that the kernel gets broader with range implying that measured reflectivity is

a smeared version of the intrinsic reflectivity and the smearing effect gets worse with range. In other words the cross-range resolution of reflectivity in azimuth is governed by the range-variant kernel given by (7.15).

#### 7.4 The CASA example

In this section a examples are presented to evaluate the performance of the resolution enhancement system. The simulations are performed in a networked environment with four radar nodes. The radars are located to match the positions of the four radar in the Integrated Projects-I (IP1) testbed deployed by CASA in Oklahoma. A composite reflectivity is obtained based on the networked retrieval technique. In addition composite reflectivities based on range weighted averaging and maximum reflectivity is also estimated. The range weighted averaging of reflectivity from multiple radars uses the fact that the resolution and signal-to-noise ratio degrades with range. Reflectivity from individual radars are relatively weighted such that measurements from the closest radar is assigned the highest weight while measurement from the farthest radar is assigned the least weight. The weight for the  $i^{th}$  radar to obtain a range weighted mosaic is given below.

$$w_i = \frac{R_i^{-p}}{\sum_{j=1}^N R_j^{-p}} \quad (7.16)$$

In the above equations  $R_j$  is the range of the resolution volume from the individual radar nodes and  $p$  is an integer selected to adjust the dependence on range. The range weighted mosaic is obtained as given below.

$$Z_{rmean}(x, y) = \sum_{j=1}^N w_j(x, y) Z_j(x, y) \quad (7.17)$$

A simulation with with  $2^\circ$  beam width was performed with a two dimensional flat-topped reflectivity field with a specified reflectivity gradient as shown in Fig. 7.4. The simulated reflectivity distribution is positioned in the coverage region of the networked radar system. The measured reflectivity at each node is obtained based

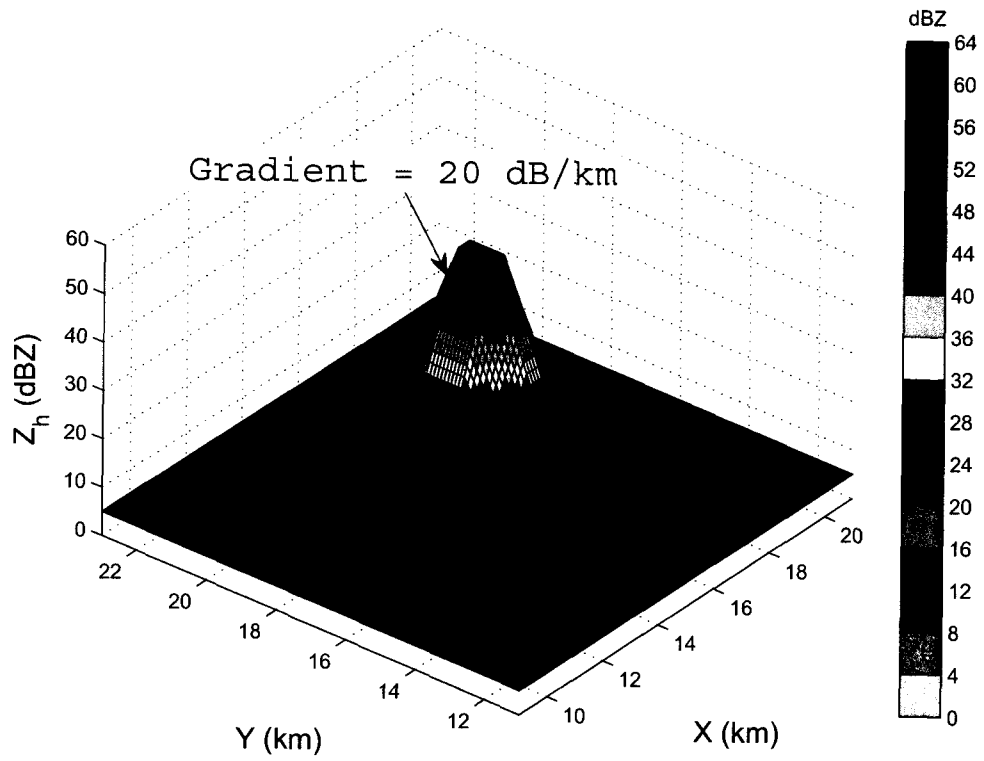


Figure 7.4: A two dimensional flat topped reflectivity distribution with 25 dB/km gradient.

on the effective antenna pattern of the radar and measurement error of 1 dB added. The RES solution was obtained for a  $6 \times 6$  km tile.

Figure 7.5 shows the application of the resolution enhancement system for a simulated data set with  $20$  dB/km reflectivity gradient. The simulation were performed for a three node configuration with nodes at Cyril, Chickasha and Rush Springs. The observed reflectivity is shown in Fig. 7.5(a), (b) and (c) while the true reflectivity is shown in Fig. 7.5(d). The smearing effect of the antenna pattern is obvious when the observations are compared with the true reflectivity. The range weighted reflectivity mosaic and networked retrieval is shown in Fig. 7.5(e) and Fig. 7.5(f) respectively. The resolution enhancement system provides a reflectivity that matches the true reflectivity and the smearing effect that lowers the peak reflectivity is mitigated with the resolution enhancement system. The range weighted mosaic performs well at the storm edges to minimize smearing but is not able to retrieve the peak reflectivity in the core of the precipitation cell.

#### 7.4.1 Multiscale analysis

Spatial variability is intrinsic to the estimated reflectivity distribution in radar meteorology. Spatial variability is dependent on both the scale and support of the estimated reflectivity distribution. Multiscale statistical methods have been extensively used to analyze spatial data. In this section we will consider Fourier spectrum to study the spatial variability and scaling.

The power spectrum of a two dimensional distribution has been used for studying spatial variability over a wide range of scales. The Fourier spectrum can be obtained with a periodogram estimate using 2D FFT as

$$F(\mathbf{k}) = F(k_1, k_2) = \frac{1}{MN} \left| \sum_{n=0}^{N-1} \sum_{m=0}^{M-1} Z(m, n) \exp \{ -j2\pi \mathbf{u}^T \mathbf{k} \} \right|^2 \quad (7.18)$$

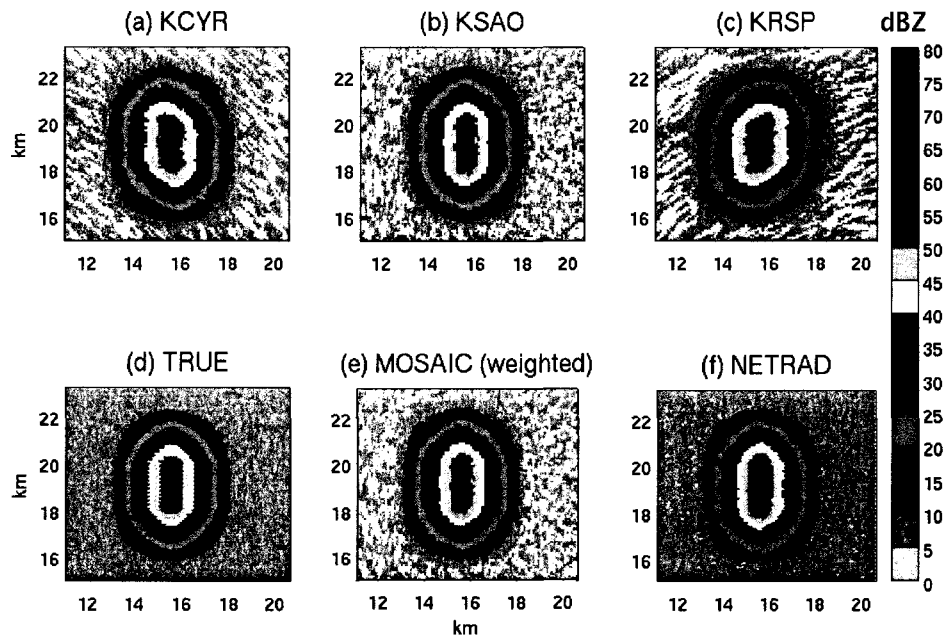


Figure 7.5: Resolution enhancement system applied to simulated data for a three radar node case. Observed reflectivity from (a) KCYR (b) KSAO (c) KRSP. (d) True reflectivity distribution (e) Range weighted mosaic (f) Resolution enhancement system.

where

$$\mathbf{k} = \begin{pmatrix} k_1 \\ k_2 \end{pmatrix} \text{ and} \quad (7.19)$$

$$\mathbf{u} = \begin{pmatrix} m/M \\ n/N \end{pmatrix}. \quad (7.20)$$

To compute the isotropic power spectrum ( $F(k)$ ,  $k = \|\mathbf{k}\|_2$ ) the 2D power spectrum is angularly averaged about  $\mathbf{k} = \mathbf{0}$ . Empirical observations suggests scale invariance of reflectivity seen as power law relation of spatial spectrum with wave-number. The power law relation between spatial spectrum and wave-number is given as

$$F(k) \sim k^{-\beta} \quad (7.21)$$

The spatial spectrum roll-off factor  $\beta$  is a measure of the variability or smoothness of the reflectivity distribution. Higher values of  $\beta$  indicate smoother reflectivity distribution while lower  $\beta$  indicates more variability in the reflectivity distribution.

#### 7.4.2 Simulations : Multiscale analysis

The performance of RES can be studied by analyzing the isotropic spectrum of the retrieved reflectivity distribution. A simulated reflectivity field is used to compare the scales of observed and retrieved reflectivity distribution. A  $12 \times 12 km$  area within the coverage of the radar network is simulated. An geometry of the simulated radar network is identical to the first generation radar network deployed by CASA. The RES solution is obtained for a  $6 \times 6 km$  area at a grid resolution of  $100 \times 100 m$  and the final solution is a tiling of the individual tiles. This sections presents results for two simulated cases. The simulations are performed for radar nodes with a beam width of  $1.8^\circ$  and maximum operating range of 40 km. Case I is a precipitation event observed by four radar nodes and Case II is a storm cell observed by only three radar nodes.

The observed reflectivity for Case I is shown in Fig. 7.6 while the range weighted reflectivity mosaic and RES retrieved reflectivity distribution for Case I is shown in

Fig. 7.7. The smearing of the observed reflectivity is obviously visible in Fig. 7.6 and the worst cross-range resolution is observed in KSAO because the storm cell is more than 35 km away from the radar as seen in Fig. 7.7(a). The true reflectivity distribution is compared with the range weighted mosaic and RES retrieval in Fig. 7.7(b). It can be observed that the reflectivity mosaic has degraded resolution when compared with RES reflectivity. The difference in resolution is clear when some of the very small features are compared between the true reflectivity, mosaic and RES reflectivity. The small features are much more spatially smeared in the range weighted mosaic when compared to the RES reflectivity.

The observed reflectivity for Case I is shown in Fig. 7.8 while range weighted reflectivity mosaic and RES retrieved reflectivity distribution for Case II is shown in Fig. 7.9. The storm cell in Case II is only observed by three radars and KRSP observations have the worst resolution because the storm is more than 35 km away from KRSP as shown in Fig. 7.9(a). Again, the true reflectivity distribution is compared with the range weighted mosaic and RES retrieval in Fig. 7.9. It can be observed that the reflectivity mosaic has degraded resolution when compared with RES reflectivity. About four high reflectivity regions are clearly visible in the true reflectivity distribution and a similar high reflectivity regions are visible in the RES reflectivity whereas these the distinction between the high reflectivity regions is not clear for the reflectivity mosaic.

It is important to observe in both Case I and Case II that mosaic and RES is not able to perfectly recover the high resolution reflectivity distribution. This is very obvious because the true reflectivity is available in simulated cases. However, in order to compare the performance of range weighted mosaic with RES multiscale analysis of the retrieved reflectivity can be performed. The isotropic power spectrum of the range weighted reflectivity mosaic and RES retrieved reflectivity is compared to the isotropic power spectrum of true reflectivity is shown in Fig. 7.10. The higher spatial variability of the reflectivity in Case I when compared to Case II is easily observed

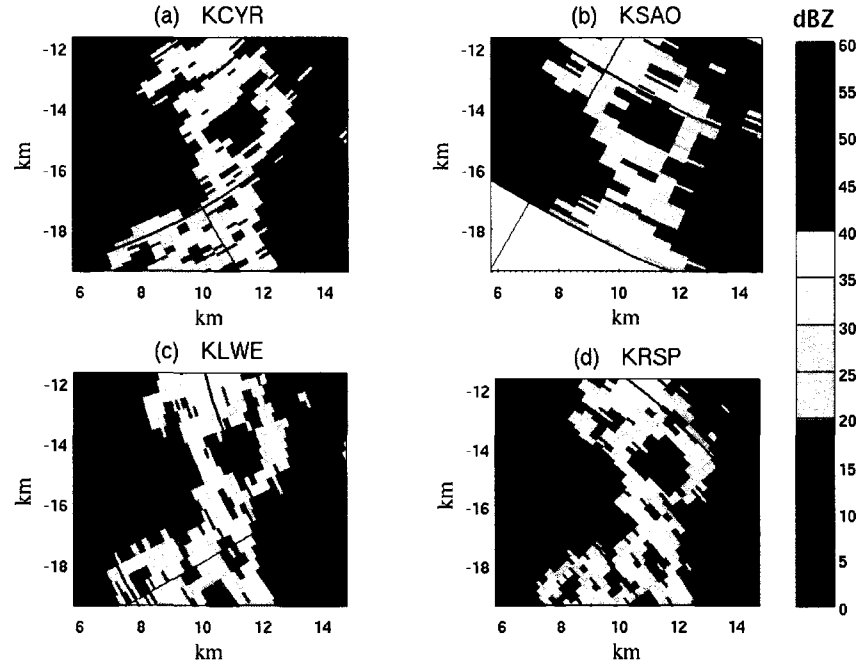


Figure 7.6: Case I : Observation of simulated data for a networked radar system :(a) KCYR (b) KSAO (c) KRSP, and (d) KLWE.

by cross comparing true reflectivities Fig. 7.7(d) and Fig. 7.9(d). This higher spatial variability is also evident from the isotropic power spectrum shown in Fig. 7.10. The power at smaller scales ( $< 500$  m) in Case I is much higher than Case II.

Figure 7.10 clearly shows that true, mosaic and RES reflectivity have comparable powers at scales larger than 1 km. However, the powers at scales smaller than 1 km are attenuated for mosaic and RES with respect to the true reflectivity. Therefore, the variability in reflectivity at smaller scales is not clearly observed in the reflectivity mosaic and RES. Although mosaic and RES do not observe the variability at all scales, the power at smaller scales for RES is closer to the true reflectivity for both Case I and Case II as shown in Fig. 7.10 (a) and Fig. 7.10 (b) respectively. Hence, it can be concluded by comparing powers at smaller scales that RES can capture small scale variability relatively better than range weighted mosaic.

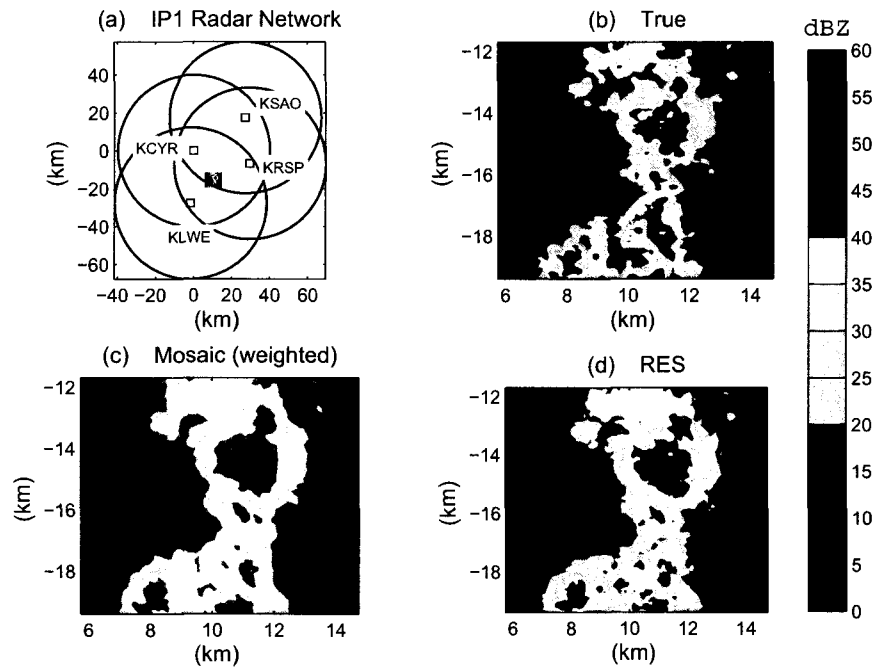


Figure 7.7: Case I : Simulated data for a networked radar system : (a) Location of the storm within the IP1 radar network (b) True reflectivity distribution (c) Reflectivity mosaic, and (d) RES retrieval.

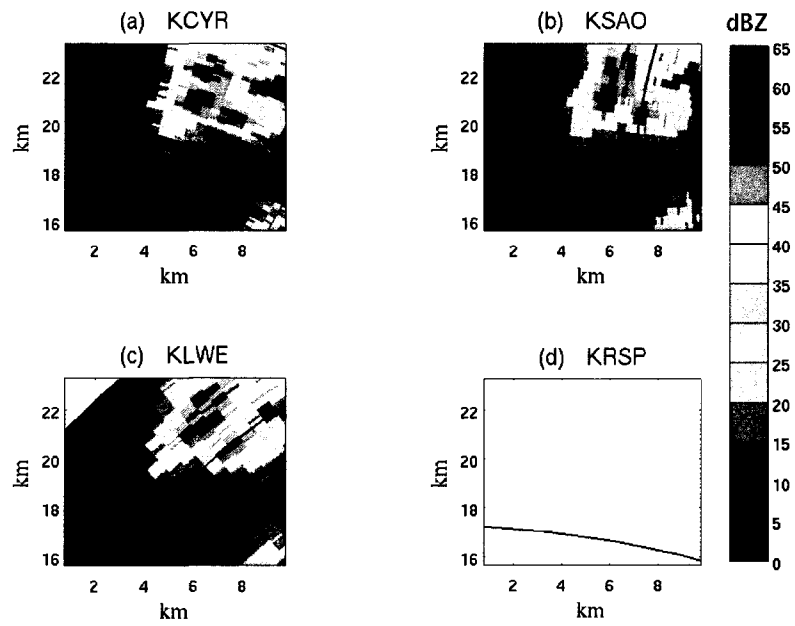


Figure 7.8: Case II : Observation of simulated data for a networked radar system :(a) KCYR (b) KSAO (c) KRSP, and (d) KLWE.

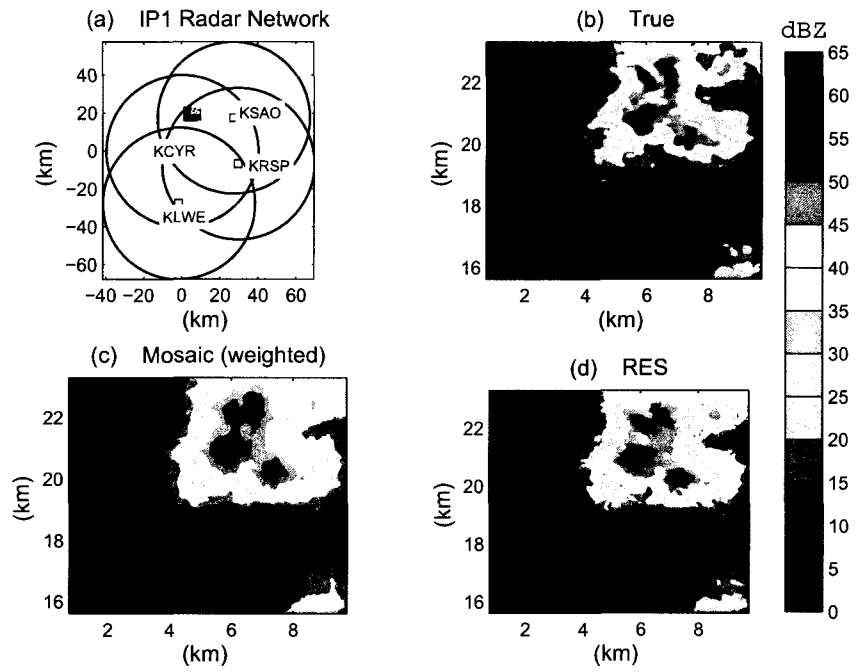
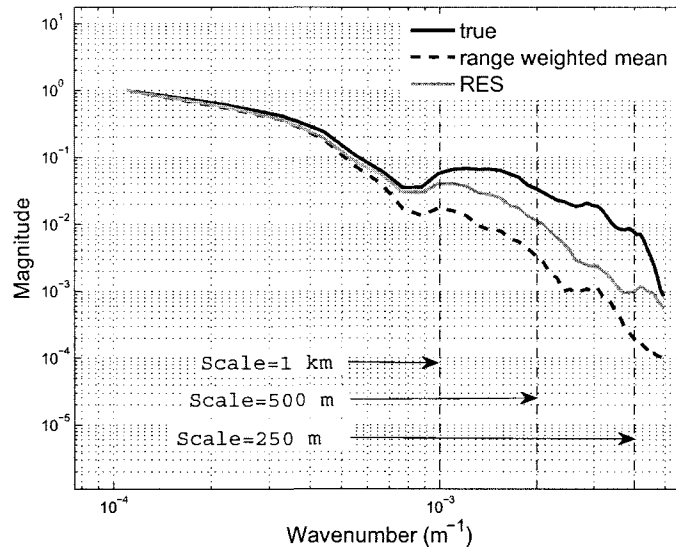
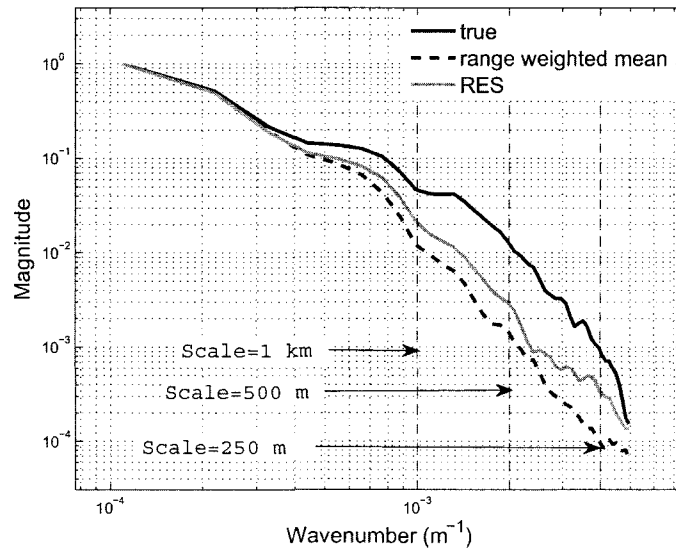


Figure 7.9: Case II : Simulated data for a networked radar system : (a) Location of the storm within the IP1 radar network (b) True reflectivity distribution (c) Reflectivity mosaic, and (d) RES retrieval.



(a)



(b)

Figure 7.10: Isotropic power spectrum of reflectivity distribution: (a) Case I; (b) Case II.

## 7.5 Implementation with CASA radar network data

In this section the resolution enhancement system is applied to data collected from IP1 testbed. The IP1 testbed is a networked radar system with four radars operating at X-band. Measurements at X-band suffer the effect of attenuation due to propagation in precipitation. The IP1 radars perform attenuation correction (Liu et al., 2006) on a real-time basis and a attenuation corrected reflectivity product is provided operationally (Junyent et al., 2009). The data used to apply RES is attenuation corrected reflectivity distribution. The four radars are separated by approximately 25 km and make measurements up to 40 km. The radars transmit a short pulse resulting in a range resolution of 60 m. A 1.2 m antenna with a  $1.8^\circ$  beam-width has a mean cross range resolution of 837 m in the coverage region of a single radar. However, mean resolution in a networked radar environment is less than the mean range resolution of an individual radar. The resolution in a networked environment is obtained by selecting the minimum resolution among the radars within the common coverage. The resolution in the CASA's IP1 radar network is shown in Fig. 7.11. A mean resolution of 736 m can be obtained by selecting the best resolution from the four IP1 radars. The reflectivity obtained corresponds to a  $1^\circ$  integration cycle which provides oversampled data in azimuth with oversampling factor  $\sim 2$ . In this paper we are not considering the retrieval of the three dimensional reflectivity distribution and hence only scans at lower elevation angle ( $\leq 2^\circ$ ) are used. The RES is solved for a grid resolution of 100 m using a  $6 \times 6 \text{ km}^2$  area tile. The origin is arbitrarily chosen to coincide with the Cyril radar and each radar GPS locations is translated to this new origin. A constrained linear least-squares solution is obtained to provide the RES reflectivity distribution.

### 7.5.1 Case I: Small precipitation cell

A small precipitating cell within the coverage of all the four radars was observed on Jun 06, 2008 at 20:36:08 UTC. The reflectivity distribution observed at  $1^\circ$  eleva-

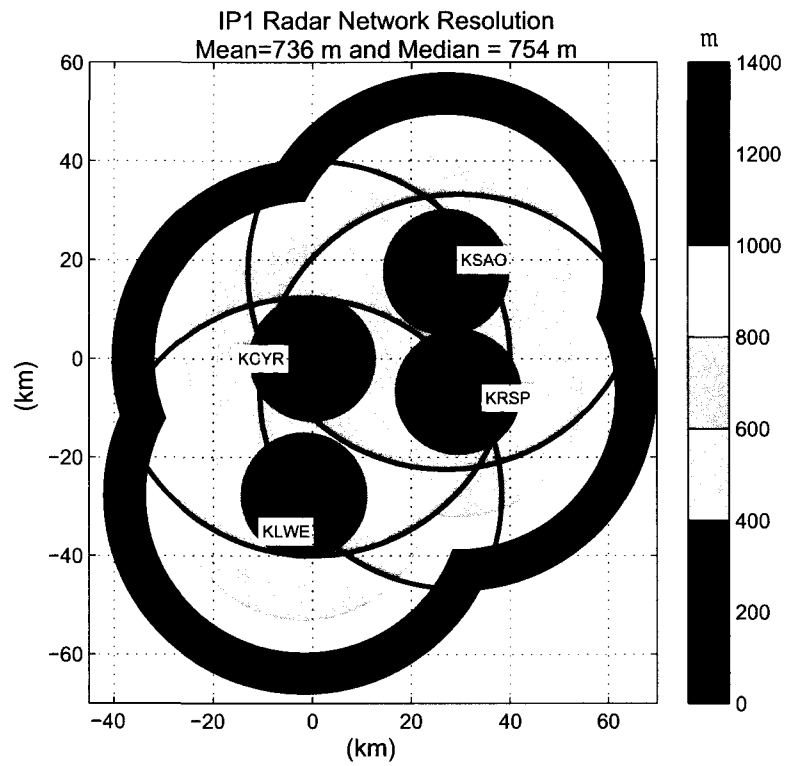


Figure 7.11: Composite networked resolution for CASA's IP1 radar network.

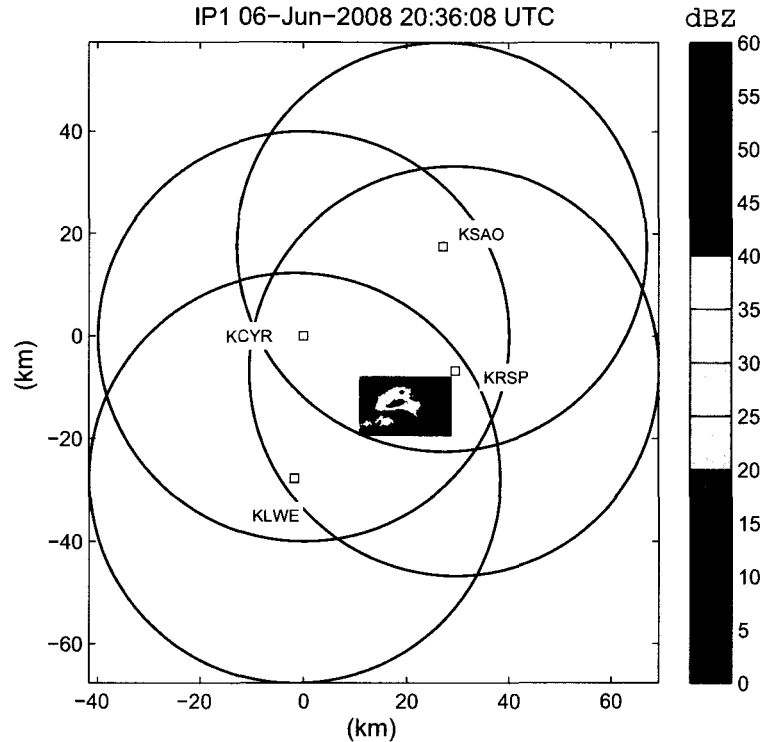


Figure 7.12: Location of the precipitation event in the radar network for data collected with IP1 radar network on Jun 06, 2008 at 20:36:08 UTC.

tion at the four nodes are used as inputs to the RES algorithm. The location of the precipitation cell relative to the radar locations is shown in Fig.7.12 and the observations made by the individual radars is shown in Fig.7.13. The smearing effect of the antenna pattern is clearly seen as the smearing effect is along the azimuth for each radar. The retrieval of reflectivity distribution from range weighted mosaic and reflectivity obtained from RES is shown in Fig.7.14(a) and (b) respectively.

### 7.5.2 Case II: Thunder storm cell

Figure 7.15 shows the relative location of the thunder storm within the IP1 radar network and the observations of reflectivity of a intense thunder storm in the IP1 radar network. The Thunder storm is observed by all the four nodes in the network as shown in Fig. 7.16. The data was collected at  $1^\circ$  elevation angle on Jun 16, 2008 at 11:30:30

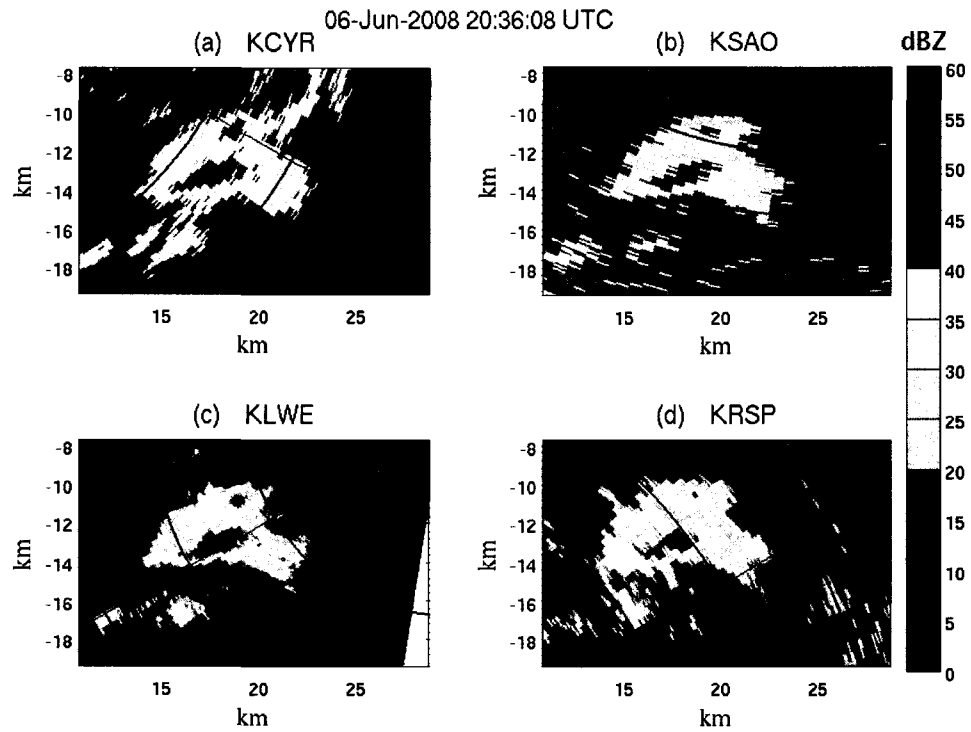


Figure 7.13: Data collected with IP1 radar network on Jun 06, 2008 at 20:36:08 UTC: (a) KCYR (b) KSAO (c) KRSP, and (d) KLWE.

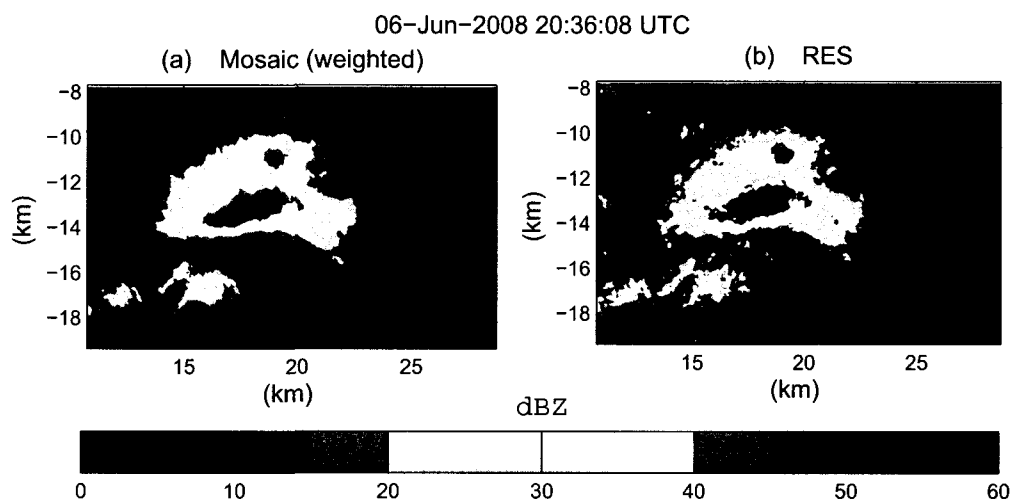


Figure 7.14: Reflectivity retrieval from the IP1 radar network with data collected on 2008-Jun-06 at 20:36:08 UTC (a) Range weighted reflectivity mosaic and (b) RES reflectivity retrieval.

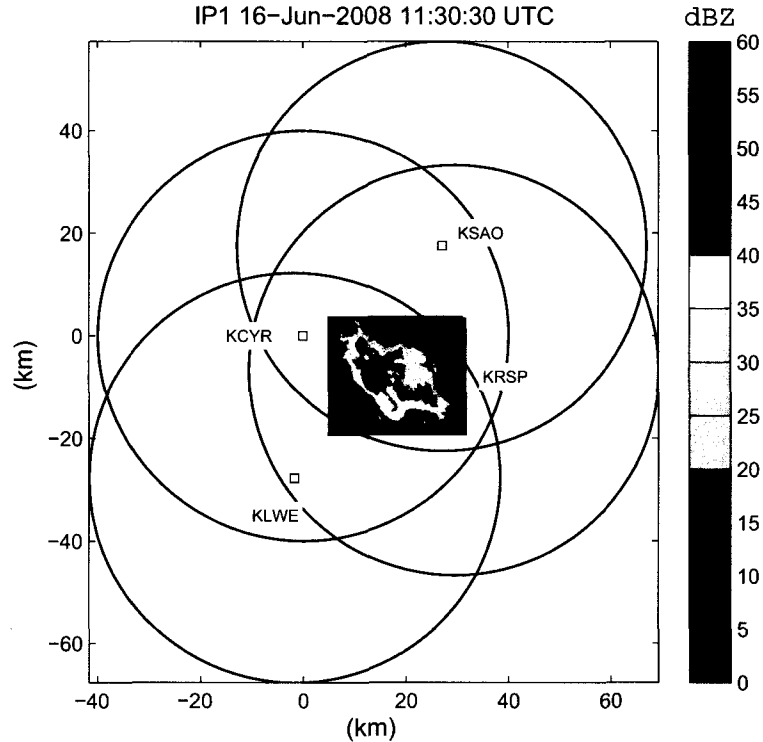


Figure 7.15: Location of the precipitation event in the radar network for data collected with IP1 radar network on Jun 16, 2008 at 11:30:30 UTC.

UTC. The comparison of reflectivity mosaic and resolution enhancement system is seen in Fig.7.17(a) and (b). Similar to the simulation results the peak reflectivity at the cores is much pronounced with the retrieval from resolution enhancement system. Also, there is more variability of features observed with the resolution enhancement system as compared to reflectivity mosaic.

### 7.5.3 Case III: Hook echo

A hook echo associated with a tornado was observed by the IP1 radar network on Feb 10, 2009 at 21:13 UTC. The position of the hook echo within the network is shown in Fig.7.18 and its clearly out of range for Rush Springs and Lawton. The hook echo was observed by only two radars located at Cyril and Chickasha as shown in Fig.7.19(a) and (b). The networked resolution enhancement system is applied to this

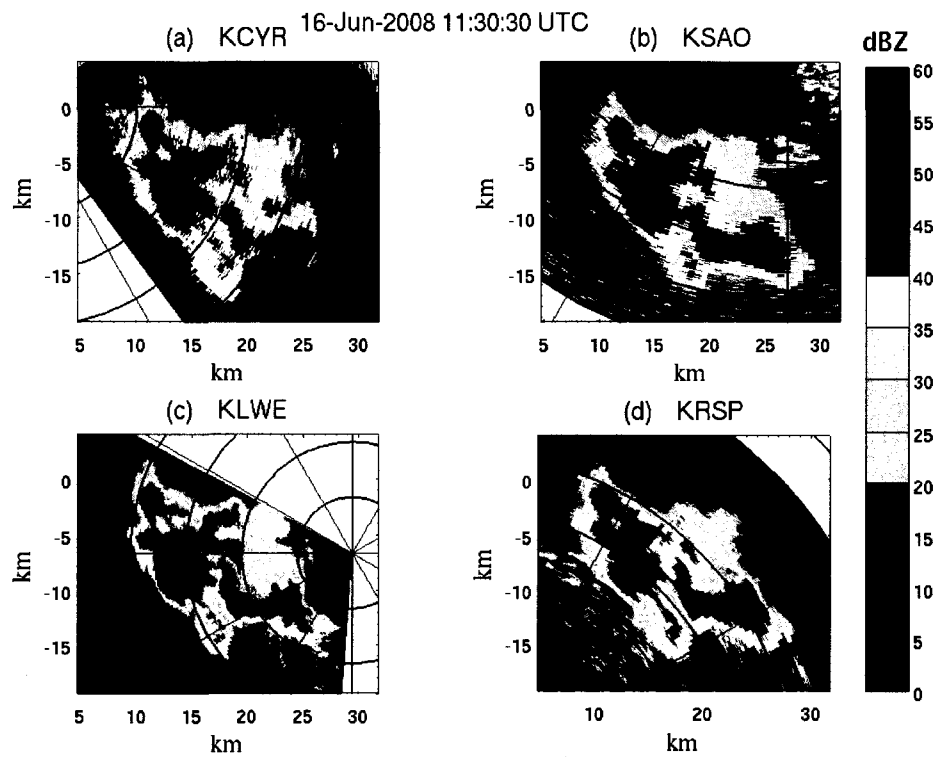


Figure 7.16: Data collected with IP1 radar network on Jun 16, 2008 at 11:30:30 UTC: (a) KCYR (b) KSAO (c) KRSP, and (d) KLWE.

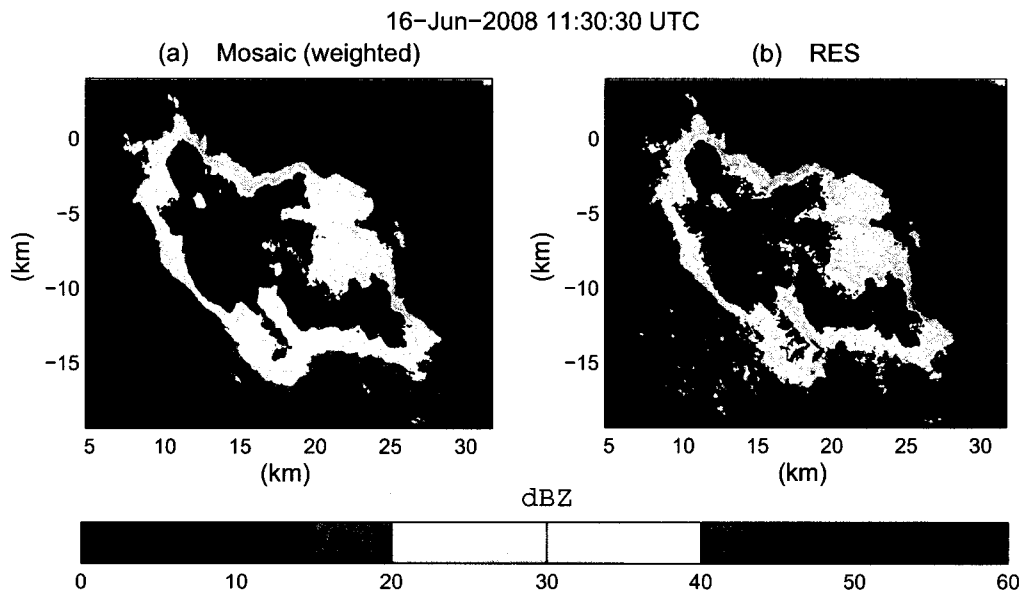


Figure 7.17: Reflectivity retrieval from the IP1 radar network with data collected on 2008-Jun-16 at 11:30:30 UTC (a) Range weighted reflectivity mosaic and (b) RES reflectivity retrieval.

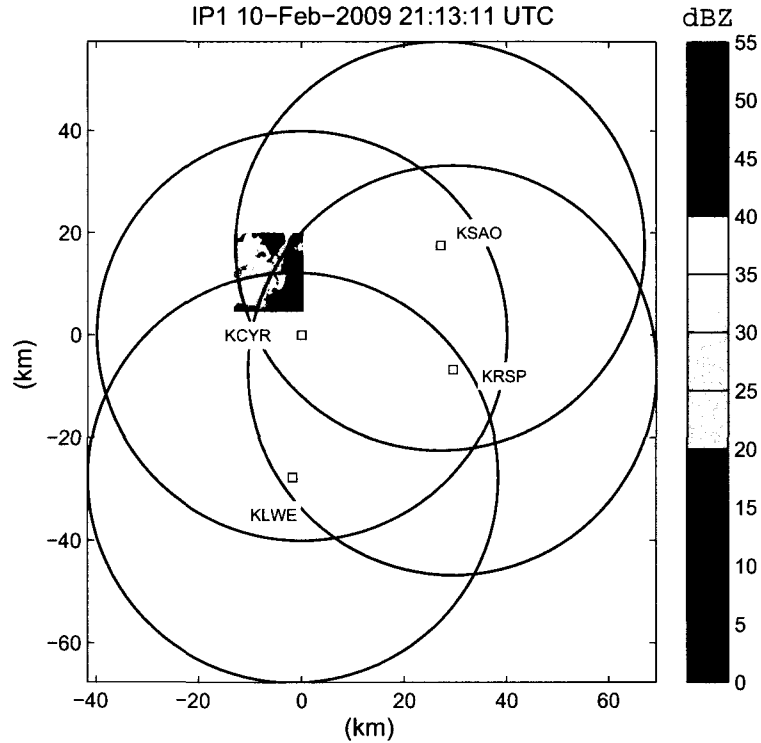


Figure 7.18: Location of the precipitation event in the radar network for data collected with IP1 radar network on Feb 10, 2008 at 21:13:11 UTC.

data set. The reflectivity mosaic and networked retrieval is shown in Fig. 7.20(b) and (c) respectively. The formation of the hook echo is much more clearly visible in the networked retrieval. Also, as observed with previous data sets the peak reflectivity observed in the the storm is much more prominent in the networked retrieval.

#### 7.5.4 Results: multiscale analysis

Scale analysis is performed on the range weighted reflectivity mosaic and RES retrieval by computing the isotropic power spectrum. The isotropic power spectrum of the reflectivity mosaic and RES retrieval for Case I, Case II, and Case III is shown in Fig. 7.21. As in the results for simulated data sets the power at scales larger than 1 km there is no significant different between mosaic and RES reflectivity. The power spectrum for mosaic and RES start to differ from each other for scales lesser



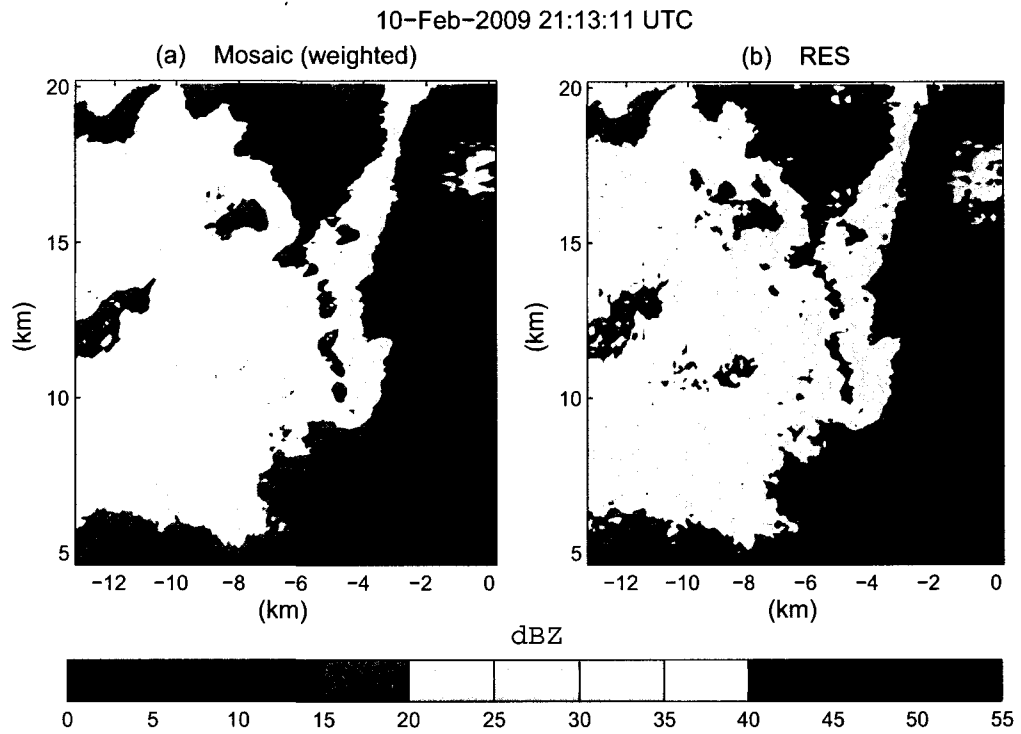


Figure 7.20: Reflectivity retrieval from the IP1 radar network with data collected on Feb 10, 2008 at 21:13:11 UTC (a) Range weighted reflectivity mosaic and (b) RES reflectivity retrieval.

than 1 km. Reflectivity from RES has consistently higher powers at lower scales than range weighted mosaic. The power difference between mosaic and RES becomes more significant for scales smaller than 500 m.

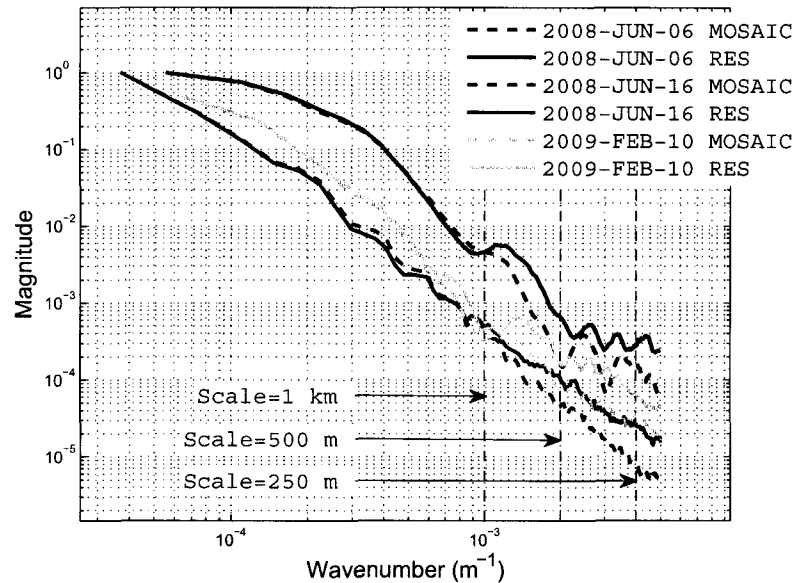


Figure 7.21: Comparison of radially average power spectral density of the RES retrieved reflectivity and range weighted mosaic.

## 7.6 Summary

The resolution of Doppler weather radars is primarily dependent on the transmit pulse length and antenna beam width. The resolution has two independent components namely, range resolution and cross-range resolution. Range resolution corresponds to the pulse length while cross-range resolution is a function of beam width and the range to the resolution volume. A brief description of the dependence of the received signal from volume targets on the radar system parameters given. The spatial resolution of the observed reflectivity is governed by the antenna beam width and the integration period. An effective antenna pattern based on a Gaussian antenna pattern and a given azimuth integration period was presented. The effective antenna

pattern provides the range variant smoothing kernel that determines the smearing of reflectivity observations along azimuth. The smearing or degradation of resolution was formulated as a linear problem relating the observed reflectivity and the intrinsic reflectivity distribution through the range variant smoothing kernel.

A novel methodology called the Resolution Enhancement System (RES) was presented to solve the ill-posed problem of improving the resolution. A networked radar approach is used in RES to undo the effect of range variant smoothing kernel. A simulation study was performed to ascertain the RES retrieval technique. A comparison of range weighted mosaic with RES was also performed based on simulated reflectivity distributions. A comparison of the true reflectivity distribution and RES reflectivity suggested a good performance of RES when compared to reflectivity mosaic. In addition to the direct comparison of reflectivities a multiscale analysis was performed using the isotropic power spectrum. A comparison of the power spectrum of the true reflectivity, reflectivity mosaic and RES reflectivity revealed that RES is better than reflectivity mosaic in capturing small scale features in the reflectivity distribution. However, RES is not able to provide the identical resolution as the true reflectivity distribution but still provides better resolution than a simple mosaic.

Finally, the novel methodology was applied to data collected by CASA's IP1 radar network. Attenuation corrected reflectivity was used as inputs from each of the four radar. The RES reflectivity retrievals from IP1 radar network were compared with the range weighted reflectivity mosaic by performing a multiscale analysis using the isotropic power spectrum. Similar to the results obtained with simulated data it is observed that RES is better than reflectivity mosaic in capturing small scale features. Application of RES based on simulated reflectivity distributions and data collected with CASA's IP1 radar shows that RES in a networked radar environment provides a viable methodology to enhance spatial resolution.

## CHAPTER 8

### SUMMARY AND CONCLUSIONS

---

---

#### 8.1 Summary and Conclusions

Networked radar systems consisting of a dense set of agile short-range high frequency radars operating as Distributed Collaborative Adaptive System (DCAS) is an emerging innovative concept for atmospheric remote sensing that offer great potential to address several challenging problems in atmospheric remote sensing. This research has addressed the key aspects of waveforms and retrieval algorithms taking into account some of the unique challenges that must be overcome to successfully deploy a networked radar system. This research also provided a comprehensive set of waveforms that form the basis for modern weather radars to operate with both networked systems and solid state transmitters.

A short description of CASA's first generation radar network was presented. The first generation processing algorithms on the radars deployed in Oklahoma heavily relies on spectral processing. The performance of spectral processing were presented based on simulations. The accuracy of the spectral moments and polarimetric variables obtained from spectral processing is slightly degraded when compared to traditional pulse-pair processing. This degradation is primarily due to the estimation of the spectral coefficients by applying a window function. However, spectral processing offers several benefits in its ability to filter ground clutter signal and overlaid echoes. An adaptive spectral processing technique for clutter suppression was presented for polarimetric variables. It is important to apply the adaptive spectral processing jointly

to the horizontal and vertical polarization channels. While the interpolation of the notch filtered region is recommended for the estimation of spectral moments, it is not recommended to perform any interpolation of the complex spectral coefficients. The adaptive spectral clutter filter was tested with data obtained from CSU-CHILL radar under very severe ground clutter conditions. The adaptive spectral filter suppressed very strong ground clutter signal from the Rocky mountains.

The quality of spectral moments and polarimetric variables depend on the ability of the waveform and associated processing to mitigate the effects of clutter, overlaid echo and velocity folding. A dual-PRF waveform was suggested as a candidate waveform for the first generation CASA radars. Based on the operational requirements and hardware limitations of the IP1 radars a dual-PRF waveform operating at 1.6 kHz and 2.4 KHz was selected for operational use. Adaptive spectral processing was utilized to concurrently mitigate the impact of ground clutter, range overlaid echoes and velocity ambiguity. A phasor median filter was proposed to spatially filter the outliers that occur due to velocity unfolding. The performance of the phasor median filter is better than regular median filter when the errors in the data are larger. The application of phasor median filter is recommended for filtering the outliers and smoothing the velocity field. The performance of the dual-PRF waveform were presented based on simulations as well as data collected by the IP1 radars during the experiments conducted in the year 2007 and 2008. Based on the data from the IP1 radars it can be concluded that the dual-PRF waveform provides acceptable ground clutter suppression and overlaid echo suppression for the systems deployed.

The transition from low cost magnetron based radars to solid-state radar requires specialized waveforms to achieve the desired sensitivity and coverage. A Frequency diversity pulse compression waveforms was proposed for the next generation radar operating with a solid-state transmitter. Performance analysis of the waveform provides valuable design space for developing the solid-state radars. A nonlinear FM

pulse compression was described with two frequency modulation components; one linear FM component and the other nonlinear component. A quadratic curve describes the nonlinear component and the quadratic curve was parameterized a bandwidth-fraction term ( $k_B$ ) and a time-fraction term ( $k_T$ ) to control the performance of the pulse compression waveform. A Tukey window function is recommended shape the rise and fall time of the transmit pulse to avoid spectral ringing. The pulse compression waveform was designed to minimize the side lobe levels by tuning the pulse shape, bandwidth-fraction, and, time-fraction of the nonlinear FM. A compression filter designed to minimized the ISL is recommended as the receive filter at base band. The compression filter is an FIR filter obtained by minimum least square solution of the cost function minimizing ISL. The minimum ISL filter has good Doppler tolerance. The impact of phase noise on the performance of the pulse compression waveform was presented and a phase noise of at least  $0.5^\circ$  is required to minimize the impact of range side lobes. The performance of the pulse compression waveform in retrieving the Doppler moments and polarimetric variables was presented from realistic simulations based on actual observation from CASA IP1 radar and CSU-CHILL radar. The frequency diversity waveform provides complete coverage without any blind ranges. Results based on simulations indicate that the frequency diversity waveforms provide a good solution for solid-state radar in improving sensitivity and mitigating the problem of blind range associated with long transmit pulses.

A networked waveform system was developed to overcome the fundamental limitation of a single pulsed Doppler radar in resolving range and velocity ambiguities. The networked radar system uses the principle that the underlying intrinsic properties of the precipitation medium remain consistent in a networked environment. The ambiguity in range and velocity is resolved by jointly processing the measurements from all the radars in the network. The networked waveform system offers many advantages. Firstly, it decouples the range ambiguity and velocity ambiguity from each other, whereas range and velocity ambiguities are coupled together in a single

node waveform. Secondly, the networked waveform can be designed to measure very high velocities without the need for complex waveforms and advanced processing at each node. This minimizes the computational load on each node. Thirdly, it can be used with low cost transmitter that has limited ability to support complex waveforms as opposed to a significantly expensive single radar system with complex waveforms. Fourthly, the networked waveform system can be designed to meet a specific requirement over the coverage region without being restricted by limitation of an individual radar node in the network. This approach shows good performance in measuring radial velocities as high as 100 m/s.

The cross-beam resolution of radar measurements degrades with increasing range resulting in poor resolution at far ranges from the radars. However, the resolution of radar measurements along range remain constant as they are determined only by the transmit waveform. The radar observations are smeared in the cross range directions resulting in degraded resolution. The smearing in the cross range direction has different impact when a continuum of volume targets are considered as opposed to isolated point targets. The primary concerns with hard targets are detection, target localization and tracking. Radar target localization and detection for hard targets using wide beams has been developed. However, precipitation systems are volume targets extending over a large area and the techniques used for point targets are not applicable here. The networked radar resolution enhancement system (RES) uses measurements from a network of radar nodes to retrieve reflectivity field with better resolution than what is possible with the individual radar nodes. RES uses the higher range resolution of radars in a networked environment to build an innovative system to enhance the resolution of the observations. The resolution enhancement system has many advantages. (i) The retrieved reflectivity has enhanced resolution compared to the individual radar observations. (ii) This technique enables the use of lower cost radars with relatively smaller apertures in a network and still retrieves reflectivity at an acceptable resolution. (iii) The retrieved reflectivity over the network coverage

region has nearly uniform resolution as opposed to reflectivity measurements with varying resolution that is obtained from single radar. (iv) The resolution enhancement can be implemented on demand in a small selected region, thereby making it suitable for targeted applications. (v) The networked radar resolution enhancement technique is designed so that it can be implemented with parallel processing. This parallel processing feature reduces the time required for processing large areas of coverage and makes the system suitable for real-time applications. The performance of RES was demonstrated both with simulated data (where we know the original resolution) as well as field observations, from an IP1 X-band radar network with four nodes deployed in SW Oklahoma. The results of RES were analyzed by performing a multiscale analysis. The multiscale analysis was performed using the isotropic spatial power spectrum of the RES retrieval. A comparison of the spatial power spectrum were made between reflectivity mosaic and RES retrieval. RES retrieval were able to capture features at smaller scales than reflectivity mosaic.

## 8.2 Future Work

Key aspects of waveforms and retrieval algorithms for a networked radar system was developed and demonstrated in this research. The following are suggestions for future work in this area of research:

- i. Colorado State University is developing a Wideband Experimental X-band radar (WiBEX) that uses a solid-state transmitter. An end-to-end evaluation of the pulse compression waveforms from data collected with WiBEX should be performed to evaluate the side-lobe performance of the NLFM waveform.
- ii. The frequency diversity pulse compression waveform should be evaluated by comparing the observations of WiBEX and CSU-CHILL.
- iii. Evaluation of the networked waveform should be performed with more data collected in severe storms from IP1 radar network.
- iv. A feasibility study and testing of the networked waveform for real-time processing should be performed to enable operational networked waveform system.
- v. Analysis of the resolution enhancement system with more data sets have to be performed to make it robust. The robustness of the resolution enhancement system must be test with data collected from the IP1 radar network.
- vi. A study to evaluate real-time operations of the resolution enhancement system should be performed.

## BIBLIOGRAPHY

- Ackroyd, M. and F. Ghani, 1973: Optimum mismatched filters for sidelobe suppression. *Aerospace and Electronic Systems, IEEE Transactions on*, **AES-9**, 214–218.
- Armijo, L., 1969: A theory for the determination of wind and precipitation velocities with Doppler radars. *J. Atmos. Oceanic Technol.*, **26**, 570–573.
- Astola, J., P. Haavisto, and Y. Neuvo, 1990: Vector median filters. *Proceedings of the IEEE*, **78**, 678–689.
- Baden, J. and M. Cohen, 1990: Optimal peak sidelobe filters for biphasic pulse compression. *Radar Conference, 1990., Record of the IEEE 1990 International*, IEEE, 249–252.
- Bharadwaj, N. and V. Chandrasekar, 2007: Phase coding for range ambiguity mitigation in dual-polarized Doppler weather radars. *J. Atmos. Oceanic Technol.*, **24**, 1351–1363.
- Bharadwaj, N., V. Chandrasekar, and F. Junyent, 2007: Evaluation of first generation CASA radar waveforms in the IP1 testbed. *Proc. IEEE IGARSS'07*, Barcelona, Spain, CD ROM.
- Bringi, V. N. and V. Chandrasekar, 2001: *Polarimetric Doppler Weather Radar: Principles and Applications*. Cambridge University Press, 636 pp.
- Carswell, J., S. Bidwell, and R. Meneghini, 2008: A novel solid-state, dual-polarized, dual wavelength precipitation doppler radar/radiometer. *Geoscience and Remote Sensing Symposium, 2008. IGARSS 2008. IEEE International*, volume 4, IV – 1014–IV –1017.
- Chandrasekar, V. and N. Bharadwaj, 2009: Orthogonal channel coding for simultaneous co and cross-polarization measurements. *J. Atmos. Oceanic Technol.*, **26**, 45–56.
- Chandrasekar, V., V. N. Bringi, and P. J. Brockwell, 1986: Statistical properties of dual-polarized radar signals. *23rd Conf. on Radar Meteorology*, Amer. Meteor. Soc., Snowmass, CO, 193–196.
- Chandrasekar, V. and A. P. Jayasumana, 2001: Radar design and management in a networked environment. *Proceedings of ITCOMM*, 142–147.

- Chandrasekar, V. and S. Lim, 2008: Retrieval of reflectivity in a networked radar environment. *J. Atmos. Oceanic Technol.*, **25**, 1755–1767.
- Chandrasekar, V., S. Lim, N. Bharadwaj, W. Li, D. McLaughlin, V. N. Bringi, and E. Gorgucci, 2004: Principles of networked weather radar operation at attenuation frequencies. *Third European Conference on Radar in Meteorology and Hydrology*, ERAD, 109–114.
- Cho, J. Y. N., 2005a: Multi-PRI signal processing for the Terminal Doppler Weather Radar. part I: Clutter filtering. *J. Atmos. Oceanic Technol.*, **22**, 575–582.
- 2005b: Multi-PRI signal processing for the Terminal Doppler Weather Radar. part II: Range velocity ambiguity mitigation. *J. Atmos. Oceanic Technol.*, **22**, 1507–1519.
- Cilliers, J. and J. Smit, 2007: Pulse compression sidelobe reduction by minimization of  $L_p$ -norms. *Aerospace and Electronic Systems, IEEE Transactions on*, **43**, 1238–1247.
- Cook, C. E. and M. Bernfeld, 1993: *Radar Signals: An Introduction to Theory and Application*. Artech House, 552 pp.
- Doviak, R. J. and D. S. Zrnić, 1993: *Doppler Radar and Weather Observations*. Academic Press., 562 pp.
- Galati, G., M. Naldi, and M. Ferri, 1996: Reconstruction of the spatial distribution of radar reflectivity of precipitations through linear-inversion techniques. *Radar, Sonar and Navigation, IEE Proceedings -*, **143**, 375–382.
- George, J., N. Bharadwaj, and V. Chandrasekar, 2008: Pulse compression for weather radars. CDROM.
- Golestani, Y., V. Chandrasekar, and R. Keeler, 1995: Dual polarized staggered PRT scheme for weather radars: Analysis and applications. *IEEE Trans. Geoscience and Remote Sensing.*, **33**, 239–246.
- Goodman, N. R., 1963: Statistical analysis based on a certain multivariate complex gaussian distribution (an introduction). *The Annals of Mathematical Statistics*, **34**, 152–177.
- Griffiths, H. and L. Vinagre, 1994: Design of low-sidelobe pulse compression waveforms. *Electronics Letters*, **30**, 1004–1005.
- Groginsky, H. L. and K. M. Glover, 1980: Weather radar canceller design. *19th Conf. on Radar Meteorology*, Amer. Meteor. Soc., 192–198.
- Holleman, I. and H. Beekhuis, 2003: Analysis and correction of dual PRF velocity data. *J. Atmos. Oceanic Technol.*, **20**, 443–453.

- Joe, P. and P. T. May, 2003: Correction of dual PRF velocity errors for operational Doppler weather radars. *J. Atmos. Oceanic Technol.*, **4**, 429–442.
- Junyent, F. and V. Chandrasekar, 2009: Theory and characterization of weather radar networks. *J. Atmos. Oceanic Technol.*, **26**, 474–491.
- Junyent, F., V. Chandrasekar, D. McLaughlin, S. Frasier, E. Insanic, R. Ahmed, N. Bharadwaj, E. Knapp, L. Krnan, and R. Tessier, 2005: Salient features of radar nodes of the first generation NetRad system. *Proc. IEEE IGARSS'05*, 420–423.
- Junyent, F., V. Chandrasekar, D. McLaughlin, E. Insanic, and N. Bharadwaj, 2009: The CASA integrated project 1 networked radar system. *J. Atmos. Oceanic Technol.*, accepted.
- Liu, Y., V. Bringi, and M. Maki, 2006: Improved rain attenuation correction algorithms for radar reflectivity and differential reflectivity with adaptation to drop shape model variation. *Geoscience and Remote Sensing Symposium, 2006. IGARSS 2006. IEEE International Conference on*, 1910–1913.
- McLaughlin, D., 2002: Presentation to committee on “Weather Radar Technology Beyond NEXRAD”. Technical report, National Research Council, Washington, D.C.
- Moisseev, D. N. and V. Chandrasekar, 2007: Nonparametric estimation of raindrop size distributions from dual-polarization radar spectral observations. *J. Atmos. Oceanic Technol.*, **24**, 1008–1018.
- Moisseev, D. N., V. Chandrasekar, C. M. H. Unal, and H. W. J. Russchenberg, 2006: Dual-polarization spectral analysis for retrieval of effective raindrop shapes. *J. Atmos. Oceanic Technol.*, **23**, 1682–1695.
- Moisseev, D. N., C. M. Nguyen, and V. Chandrasekar, 2008: Clutter suppression for staggered prt waveforms. *J. Atmos. Oceanic Technol.*, in press.
- Mudukutore, A. S., V. Chandrasekar, and R. J. Keeler, 1998: Pulse compression for weather radars. *IEEE Trans. Geoscience and Remote Sensing.*, **36**, 125–142.
- Nakagawa, K., H. Hanado, K. Fukutan, and T. Iguchi, 2005: Development of a c-band pulse compression weather radar. *32nd Conf. on Radar Meteorology*, Amer. Meteor. Soc., Albuquerque, New Mexico, CD ROM.
- Nathanson, F. E., 1969: *Radar Design Principles*. McGraw-Hill, 626 pp.
- NRC, 1995: *Assessment of NEXRAD Coverage and Associated Weather Services*. Compass Series (Washington, D.C.), 112 pp.
- Passarelli, R. E. and D. S. Zrnic, 1989: An expression for phase noise. *24th Conf. on Radar Meteorology*, Amer. Meteor. Soc., Tallahassee, Florida, 433–435.
- Peebles, P. Z., 1998: *Radar Principles*. Wiley-Interscience, 794 pp.

- Sachidananda, M. and D. Zrnica, 1999: Systematic phase codes for resolving range overlaid signals in a Doppler weather radar. *J. Atmos. Oceanic Technol.*, **16**, 1351–1363.
- 2000: Clutter filtering and spectral moment estimation for doppler weather radars using staggered pulse repetition time. *J. Atmos. Oceanic Technol.*, **17**, 323–331.
- 2002: An improved clutter filtering and spectral moment estimation algorithm for staggered PRT sequences. *J. Atmos. Oceanic Technol.*, **19**, 2009–2019.
- Seminario, M., K. Gojara, and V. Chandrasekar, 2001: Noise correction of polarimetric radar measurements. *30 nd Conf. on Radar Meteorology*, Amer. Meteor. Soc., Munich, Germany, 38–40.
- Siggia, A., 1983: Processing phase coded radar signals with adaptive digital filters. *21st Conf. on Radar Meteorology*, Amer. Meteor. Soc., Edmonton, AB, Canada, 513–518.
- Siggia, A. and J. Passarelli, 2004: Gaussian model adaptive processing (GMAP) for improved ground clutter cancellation and moment calculation. *European Conference on Radar in Meteorology and Hydrology*, ERAD., 67–73.
- Skolnik, M. I., 1990: *Radar Handbook*. McGraw-Hill Professional, second edition, 1200 pp.
- Torres, S. M., Y. F. Dubel, and D. S. Zrnica, 2004: Design, implementation, and demonstration of a staggered PRT algorithm for the WSR-88D. *J. Atmos. Oceanic Technol.*, **21**, 1389–1399.
- Wang, Y., V. Chandrasekar, and B. Dolan, 2008: Development of scan strategy for dual doppler retrieval in a networked radar system. *Geoscience and Remote Sensing Symposium, 2008. IGARSS 2008. IEEE International*, volume 5, V –322–V –325.
- Winchell, M., H. V. Gupta, and S. Sorooshian, 1998: On the simulation of infiltration- and saturation-excess runoff using radar-based rainfall estimates: Effects of algorithm uncertainty and pixel aggregation. *Water Resour. Res.*, **34**, 2655–2670.
- Wood, V. T. and R. A. Brown, 1992: Effects of radar proximity on single-doppler velocity signatures of axisymmetric rotation and divergence. *Monthly Weather Review*, **120**, 2798–2807.
- Yu, T.-Y., G. Zhang, A. B. Chalamalasetti, R. J. Doviak, and D. S. Zrnica, 2006: Resolution enhancement technique using range oversampling. *J. Atmos. Oceanic Technol.*, **23**, 228–240.
- Zhang, G., T.-Y. Yu, and R. J. Doviak, 2005: Angular and range interferometry to refine weather radar resolution. *Radio Sci.*, **40**, RS3013.1–RS3013.10.

- Zink, M., E. Lyons, D. Westbrook, and J. Kurose, 2008: Closed-loop architecture for distributed collaborative adaptive sensing of the atmosphere: Meteorological command and control. *International Journal of Sensor Networks*, In press.
- Zrnic, D., 1980: Spectral statistics for complex colored discrete-time sequence. *Acoustics, Speech and Signal Processing, IEEE Transactions on*, **28**, 596–599.
- Zrnic, D. and P. Mahapatra, 1985: Two methods of ambiguity resolution in pulsed Doppler weather radars. *IEEE Trans. Aerosp. Electr. Syst.*, **21**, 470–483.